

MOLECULAR DISSECTION OF A-TYPE LAMIN-REGULATED PATHWAYS

Tobias Corne

A dissertation submitted to Ghent University and the University of Antwerp
in partial fulfilment of the requirements for the degree of
Doctor of Applied Biological Sciences (Ghent University)
and Doctor of Bio-science Engineering (University of Antwerp)

2017

PROMOTORS

Prof. dr. ir. Winnok H. De Vos
Laboratory of Cell Biology and Histology, Department of Veterinary Sciences,
University of Antwerp

Prof. dr. Els J.M. Van Damme
Biochemistry and Glycobiology, Department of Molecular Biotechnology, Ghent
University

DEAN

Prof. dr. Nick Schryvers
Faculty of Science, University of Antwerp

Prof. dr. ir. Marc Van Meirvenne
Faculty of Bio-science Engineering, Ghent University

RECTOR

Prof. dr. Herman Van Goethem
University of Antwerp

Prof. dr. Md. Anne De Paepe
Ghent University

BOARD OF EXAMINERS

Prof. dr. ir. Guy Smagghe (Chairman)
Faculty of Bioscience Engineering, Ghent University

Prof. dr. ir. Tim De Meyer (Secretary),
Department of Mathematical Modeling, Statistics and Bio-informatics, Ghent University

Dr. ir. Charlotte Grootaert
Department of Food Safety and Food Quality, Ghent University

Dr. Md. Valerie Verstraeten
Academic Hospital Maastricht, Maastricht University

Dr. Sylvain Gabriele
Department of Chemistry, University of Mons

Prof. dr. Jean-Pierre Timmermans
Department of Veterinary Sciences, University of Antwerp

Prof. dr. Kevin Braeckmans
Department of Pharmaceutics, Ghent University

TABLE OF CONTENTS

Acknowledgments	III
Dankwoord	IV
Summary	IV
Samenvatting.....	VIII
List of abbreviations.....	X
Chapter 1: General introduction.....	1
1.1. Nuclear lamins and laminopathies.....	2
1.1.1. Nuclear lamins	2
1.1.2. Functions of lamins	7
1.1.3. Laminopathies.....	11
1.2. Modern tools for cell biology	16
1.2.1. Genomics.....	17
1.2.2. Proteomics	17
1.2.3. High-throughput microscopy	19
1.2.4. Raman microspectroscopy.....	21
1.3. Scope	24
Chapter 2: Sustained accumulation of prelamin A and depletion of lamin A/C both cause oxidative stress and mitochondrial dysfunction but induce different cell fates	27
Abstract.....	28
2.1. Introduction.....	28
2.2. Results	29
2.3. Discussion	36
2.4. Materials and methods	39
Chapter 3: Deregulation of focal adhesion formation and cytoskeletal tension due to loss of A-type lamins	47
Abstract.....	48
3.1. Introduction.....	48
3.2. Results	49
3.3. Discussion	60
3.4. Materials and Methods	62
Chapter 4: ZMPSTE24 deficiency impairs intracellular lipid storage as revealed by Raman microspectroscopy	69

Abstract.....	70
4.1. Introduction.....	70
4.2. Results	71
4.3. Discussion	77
4.4. Materials and Methods	78
Chapter 5: General Discussion and perspectives.....	84
References	94

ACKNOWLEDGEMENTS

This research was supported by the University of Antwerp (TTBOF/29267), the Special Research Fund of Ghent University (project BOF/11267/09), the Hercules foundation (AUGE/013), NB-Photonics (Project code 01-MR0110) and the CSBR (Centres for Systems Biology Research) initiative from the Netherlands Organisation for Scientific Research (NWO; No: CSBR09/013V). The nanobody lab of Prof. dr. Jan Gettemans is acknowledged for sharing the antibodies directed against FSCN1, ACTR2 and ACTR3. Dr. Pieter Rondou of the Centre for Medical Genetics is acknowledged for sharing the antibodies directed against vinculin and STAT3. Renate De Smedt is acknowledged for helping with the western blot analysis of vinculin. At last dr. Christian Matthäus and dr. Claudia Beleites, from the Insitute of Photonic Technology in Jena, Germany are gratefully acknowledged for their advice and training on Raman acquisition and Raman spectra analysis, respectively.

DANKWOORD

Mijn doctoraat verliep niet van een leien dakje. De "PhD blues" heb ik zelf aan den lijve mogen ondervinden. Deze werden voornamelijk aangewakkerd door tegenslagen tijdens mijn doctoraatsonderzoek zoals het niet kunnen reproduceren van resultaten, mycoplasma infecties, het verlies van de cel opslag, en de plotse verhuis van het laboratorium voor aquacultuur (samen met zijn ChemiDoc MP ...). Anderzijds heb ik ook wel een aantal aha-erlebnis momenten mogen ervaren. Het kunnen scheiden van lamine A en prelamine A met SDS-PAGE na twee jaar knoeien, bijvoorbeeld, of het op punt stellen van de Raman acquisitie en analyse en het kunnen nabootsen van laminopathie cellen met knockdowns. Naar mijn bescheiden mening hebben we met onze kleine onderzoeksgroep, "Cell Systems and Imaging" (niet te verwarren met Crime Scene Investigation), toch mooie resultaten geboekt waar ik best wel fier op ben. De sociale cohesie zat goed binnen het CSI-team. Denk maar aan de sportnamiddagen (ik drink nooit meer Ommegang), Stockholm en Isle sur Sorgue.

Er zijn uiteraard een aantal mensen die ik nog eens speciaal wil bedanken. Allereerst Tom Sieprath, mijn dichtste collega. Hij heeft me vaak te hulp geschoten en gesteund in moeilijke tijden. Zowel tijdens onze middagpauzes als achter ons computerscherm konden we bij elkaar ventileren, wat meer dan eens nodig was. Toch begrijp ik nog steeds niet waarom hij ooit voor N-VA gestemd heeft. Ik wil ook zeker Joke Robijns bedanken. Zonder haar bestond het vierde hoofdstuk van dit doctoraat niet. Ze kwam terecht in een redelijk chaotische onderzoeksgroep wat zeker geen sinecure was. De officieuze CSI'er Pieter Wuytens verdient ook een eervolle vermelding. Ik vergeet nooit het moment waarop ik bijna moest overnachten in de trappenhal van het Max Planck instituut in Potsdam. Tom, Pieter en ik hadden toch wel een speciale band: onze Brompton plooi-fiets. Een fietsband dus eigenlijk. Ook merci aan Niels De Brandt en Frederick Tison. Onze onderzoeksgroep was altijd geliefd onder thesis studenten met hier en daar een interessant figuur, wat het onderzoek des te boeiender maakte. Sofie De Schynkel en Fien De Block zijn de fundamentele van ons departement en verdienen zeker een eervolle vermelding. Geert Meesen, de schrik van iedere ethidiumbromide molecule, wil ik ook bedanken en me bij deze nogmaals verontschuldigen voor die ene zaterdag waarop hij moest komen opdraven. Prof. Els Van Damme wil ik bedanken voor het in goede banen leiden van mijn doctoraat en de fijne samenwerking met onze onderzoeksgroep. De leden van de examencommissie wil ik van harte bedanken voor hun constructieve commentaren. Tenslotte vermeld ik graag ook mijn nieuwe werkgever, CREAX, voor de kans die ze mij gegeven hebben.

Prof. dr. ir. Winnok H. De Vos verdient hier zijn eigen alinea. Winnok stak enorm veel tijd en energie in mijn doctoraat, waar ik hem zeer dankbaar voor ben. Zijn kritische blik tilde dit werk naar een nóg hoger niveau. Timemanagement is nooit mijn sterkste kant geweest, onze communicatie liep soms wat stroef en de afstand speelde ons ook soms parten. Maar het is ons toch gelukt om dit verhaal tot een goed einde te brengen. Dus Winnok, bedankt voor jouw geduld en toewijding.

Ten laatste wil ik mijn vriendin Heleen, haar familie en mijn dochtertje Lia bedanken. Voor Heleen was dit geen gemakkelijke periode. Aangezien ik het schrijven van mijn doctoraat moest combineren met mijn nieuwe job, heb ik ze toch wat verwaarloosd. Daarenboven kochten we net een huis in Gent, waardoor een zenuwzinking de laatste tijd nooit veraf was. Bedankt lief voor jouw steun tijdens deze moeilijke periode... en het regelen van mijn receptie. Lia betekent alles voor mij, ze is ongetwijfeld het beste wat mij ooit is overkomen. Mijn doctoraat wil ik daarom graag aan haar opdragen. Binnen 23 jaar is ze misschien zelf deze sectie aan het invullen, wie weet ... Ik ga er alleszins voor zorgen dat ze geen beroep moet doen op "Rich Meet Beautiful".

SUMMARY

The nuclear lamina, a thin filamentous protein layer beneath the nuclear envelope, physically supports the cell nucleus and has a central role in nuclear organization and gene regulation. The major constituents of this meshwork are type V intermediate filament proteins, known as lamins. Mutations in the *LMNA* gene, which encodes A-type lamins, or in the *ZMPSTE24* gene, which encodes a zinc metalloprotease involved in the maturation of A-type lamins, are linked to a wide spectrum of tissue-specific and systemic diseases collectively called laminopathies. Disease manifestations include muscular dystrophies, lipodystrophies, dilated cardiomyopathies and the premature aging syndromes Hutchinson-Gilford progeria (HGPS) and restrictive dermopathy (RD). The wide variety of diseases caused by mutations in the *LMNA* gene illustrates the pleiotropic functionality of A-type lamins in cell physiology. Although a large number of disease-causing mutations has been identified, the underlying pathogenic mechanisms are not completely understood.

To unveil A-type regulated pathways, we have optimized and used cellular models in which we blocked the expression of *LMNA* or *ZMPSTE24*. This was achieved through sustained siRNA-mediated knockdown in human dermal fibroblasts or by CRISPR/Cas9-mediated genome editing in HeLa cells.

First, we investigated the effect on redox biology. Sustained knockdown revealed that both persistent prelamin A accumulation and lamin A/C depletion elevated intracellular ROS levels, but to a different extent, and with different effects on cell fate. *LMNA* knockdown eventually induced apoptosis, while *ZMPSTE24* knockdown triggered a senescence pathway. We hypothesize that a threshold level of intracellular reactive oxygen species (ROS) underlies this bifurcation and that the loss of A-type lamins removes an essential ROS buffering capability.

Next, to further our knowledge on the molecular effects of *LMNA* deficiency, we compared the proteome of *LMNA* knockdown fibroblasts with mock-treated controls using quantitative stable isotope labelling-based shotgun proteomics. This revealed that the largest fraction of differentially produced proteins was involved in actin cytoskeleton organization. Interestingly, functional validation showed that loss of A-type lamins perturbed the coordination between focal adhesion formation and cytoskeletal tension. We believe that this imbalance may contribute to the mechanosensing defects that are observed in certain laminopathies.

Finally, to identify molecular changes associated with *ZMPSTE24* deficiency at the cellular level we analysed genome-edited *ZMPSTE24* knockout cells with label-free confocal Raman microscopy. We identified a decreased lipid content in *ZMPSTE24*-deficient HeLa cells attributed to a significant reduction in lipid droplet number and size. Counterintuitively, this was accompanied with increased expression of several lipid droplet biogenesis genes. We believe that overexpression of these genes is a

compensatory mechanism against the accelerated lipolysis induced by prelamin A accumulation.

In summary, we show that redox balance, focal adhesion and cytoskeletal tension are affected by loss of A-type lamins. We hypothesize that these pathways are interlinked and that ROS can be partly responsible for the uncoupling between cell adhesion and cytoskeletal tension. Furthermore, reduced focal adhesion and high ROS levels trigger apoptosis. Persistent prelamin A accumulation on the other hand, triggers a senescence pathway and interferes with lipid storage, in line with prelamin A-linked lipodystrophies. These findings open up new treatment strategies for laminopathies, in particular for muscular dystrophies, dilated cardiomyopathies and mandibuloacral dysplasia type B. These treatments strategies include reducing ROS levels, restoring mitochondrial function, increasing proteasome activity and increasing autophagy.

SAMENVATTING

De nucleaire lamina is een dunne filamenteuze proteïne laag onder de nucleaire enveloppe, die ondersteuning geeft aan de celkern. Ze speelt een centrale rol bij de organisatie van de celkern en bij genregulatie. De belangrijkste componenten van dit netwerk zijn de type V intermediaire filament-eiwitten, die gekend zijn als de lamines. Mutaties in het *LMNA* gene, dat codeert voor de type A lamines, of in het *ZMPSTE24* gen, dat een rol speelt bij de maturatie van type A lamines, veroorzaken een breed spectrum aan ziektes, genaamd laminopathieën. Tot deze ziekten behoren musculaire dystrofieën, lipodystrofieën, gedilateerde cardiomyopathie en de premature verouderingsziekten Hutchinson-Gilford progeria (HGPS) en restrictieve dermopathy (RD). Het brede gamma aan ziektes toont aan dat type A lamines betrokken zijn bij ver uiteenlopende cellulaire processen. Alhoewel een groot aantal mutaties gekend zijn, blijft het gissen naar de onderliggende mechanismen die aan de basis liggen van de pathogenese.

Om een beter inzicht te verschaffen over welke pathways gereguleerd worden door type A lamines, hebben we cellulaire modellen ontwikkeld, waarin de expressie van *LMNA* of *ZMPSTE24* verstoord werd. Hiervoor hebben we gebruik gemaakt van siRNA-gemedieerde knockdown in humane dermale fibroblasten of CRISPR/Cas9-gemedieerde genoom editing in HeLa cellen.

In eerste instantie werd het effect op redox biologie bestudeerd. De knockdown modellen toonden aan dat zowel hardnekkige prelamine A accumulatie, als verlies van type A lamines, leidden tot een verhoogde hoeveelheid reactieve zuurstofverbindingen (ROS), waarbij de omvang en het effect op celproliferatie afhankelijk was van het type knockdown. *LMNA*-knockdown resulteerde uiteindelijk in apoptose, terwijl *ZMPSTE24*-knockdown senescentie induceerde. Waarschijnlijk bepaalt de grootteorde van de toename van ROS het lot van de cel, waarbij een sterke toename van ROS apoptose induceert, terwijl een gematigde toename leidt tot senescentie. Daarnaast gaat het verlies van type A lamines gepaard met het verlies van een essentiële ROS buffer.

Daarnaast werd met behulp van kwantitatieve shotgun proteomics, gebaseerd op stabiele isotoop labeling, het proteoom van *LMNA*-knockdown fibroblasten vergeleken met controle fibroblasten, om de moleculaire effecten van *LMNA-deficiëntie* beter in kaart te brengen. Hieruit bleek dat de grootste fractie aan differentieel geproduceerde eiwitten waren betrokken bij de organisatie van het actine-cytoskelet. Functionele validatie wees op een verstoord evenwicht tussen focale adhesie en cytoskeletaire spanning. Deze onbalans draagt hoogstwaarschijnlijk bij aan de defecte mechanosensing, geobserveerd in bepaalde laminopathieën.

Tenslotte werd beroep gedaan op confocale Raman microspectroscopie. Met deze technologie werden de moleculaire veranderingen geassocieerd met *ZMPSTE24*-deficiëntie in kaart gebracht. Analyse van HeLa cellen met een *ZMPSTE24*-knockout,

wees op een verlies van vetopslag. Dit was te wijten aan een significante verlaging in het aantal en het oppervlak van intracellulaire vetlichaampjes. Contra-intuïtief werd dit verlies vergezeld door een verhoogde expressie van genen betrokken bij de biogenese van vetlichaampjes. Deze genen vertonen hoogstwaarschijnlijk een verhoogde expressie om de verhoogde vetafbraak te compenseren, die door prelamine A accumulatie geïnduceerd wordt.

Samengevat tonen we met dit werk aan dat redoxbalans, focale adhesie en cytoskeletaire spanning, beïnvloed worden door verlies van type A lamines. We postuleren dat ROS verantwoordelijk is voor de ontkoppeling tussen celadhesie en cytoskeletaire spanning. Verhoogde ROS en verminderde celadhesie kunnen apoptosis induceren. Daarnaast hebben we aangetoond dat aanhoudende prelamine A accumulatie senescentie induceert en de intracellulaire vetopslag verstoort, in lijn met de prelamine A-gerelateerde lipodystrofieën. Onze bevindingen maken nieuwe behandelingsstrategieën mogelijk. Deze omvatten het reduceren van ROS, het herstellen van de mitochondriale functie, het verhogen van proteasoom activiteiten en het induceren van autofagie in patiëntencellen.

LIST OF ABBREVIATIONS

CARS:	coherent anti-Stokes-shifted Raman scattering
CDDO-me:	2-Cyano-3,12-dioxo-oleana-1,9(11)-dien-28-oic acid methyl ester
CM-H ₂ DCFDA:	5-(and-6)-chloromethyl-2',7'-dichlorodihydrofluorescein diacetate
CRM:	confocal Raman microscopy
DCM:	dilated cardiomyopathy
FA:	focal adhesion
GO:	gene ontology
HCA:	hierarchical cluster analysis
HeLa-WT:	wild type HeLa cells
HeLa-ZKO:	<i>ZMPSTE24</i> knockout HeLa cells
HGPS:	Hutchinson-Gilford progeria syndrome
hMSCs:	human mesenchymal stem cells
hTERT:	human telomerase reverse transcriptase
iPSC:	induced pluripotent stem cell
LA:	lamin A
LD:	lipid droplet
LMNAkd:	<i>LMNA</i> knockdown
MADB:	mandibuloacral dysplasia type B
MEF:	mouse embryonic fibroblasts
NHDF:	normal human dermal fibroblasts
NTkd:	non-targeting knockdown
OCR:	oxygen consumption rate
PCA:	principal component analysis
PDL:	population doubling level
PLA:	prelamin A
RD:	restrictive dermopathy
RMS:	Raman microspectroscopy
ROS:	reactive oxygen species
SILAC:	stable isotope labeling of amino acids in cell culture
SRS:	stimulated Raman scattering
STAT3kd:	<i>STAT3</i> knockdown
TBHP:	tert-butyl hydrogen peroxide
TFM:	Traction force microscopy
TMRM:	tetramethyl rhodamine methyl ester
VCA:	vertex component analysis
ZMPSTE24kd:	<i>ZMPSTE24</i> knockdown
$\Delta\psi_m$:	mitochondrial membrane potential

1

GENERAL INTRODUCTION

1.1. Nuclear lamins and laminopathies

1.1.1. Nuclear lamins

The nuclear envelope and nuclear lamina

The nuclear envelope (NE) separates the nucleus from the cytoplasm in eukaryotic cells.¹ It is composed of an inner nuclear membrane (INM), an outer nuclear membrane (ONM), the nuclear lamina and nuclear pore complexes (NPCs), which are embedded in the NE (Figure 1-1).² The ONM is continuous with the endoplasmic reticulum (ER) and is covered with ribosomes.³ The INM contains integral and peripheral membrane proteins, which have specific nuclear functions.² The distance between INM and ONM is around 40-50 nm, and both membranes join at the NPCs.⁴ NPCs are large (~50 MDa) proteinaceous assemblies that allow passive diffusion of ions and small molecules up to 50kDa and facilitate receptor-mediated bidirectional exchange of larger molecules (proteins and ribonucleoprotein complexes) between the nucleoplasmic and cytoplasmic compartments.^{5,6}

The nuclear lamina is a dense proteinaceous meshwork that lines the INM in metazoan cells.^{7,8} The nuclear lamina gives mechanical support to the nucleus, and is involved in many nuclear activities, including chromatin organization, transcription and replication.^{9,10} Its thickness varies in between 10 and 20 nm in somatic cells.^{10,11} The major constituents of the nuclear lamina are lamins, type V intermediate-filament proteins.¹² A small fraction of lamins is also present in the nucleoplasm, on invaginations of the NE forming a so-called nucleoplasmic reticulum, or as dispersed (veil-like) structures.¹³⁻¹⁶ The nuclear reticulum has been proposed to facilitate nuclear processes such as nuclear transport or calcium storage.¹⁵ Next to lamin proteins, the nuclear lamina contains a large number of inner-membrane proteins, which help anchor lamin filaments to the NE.¹⁷

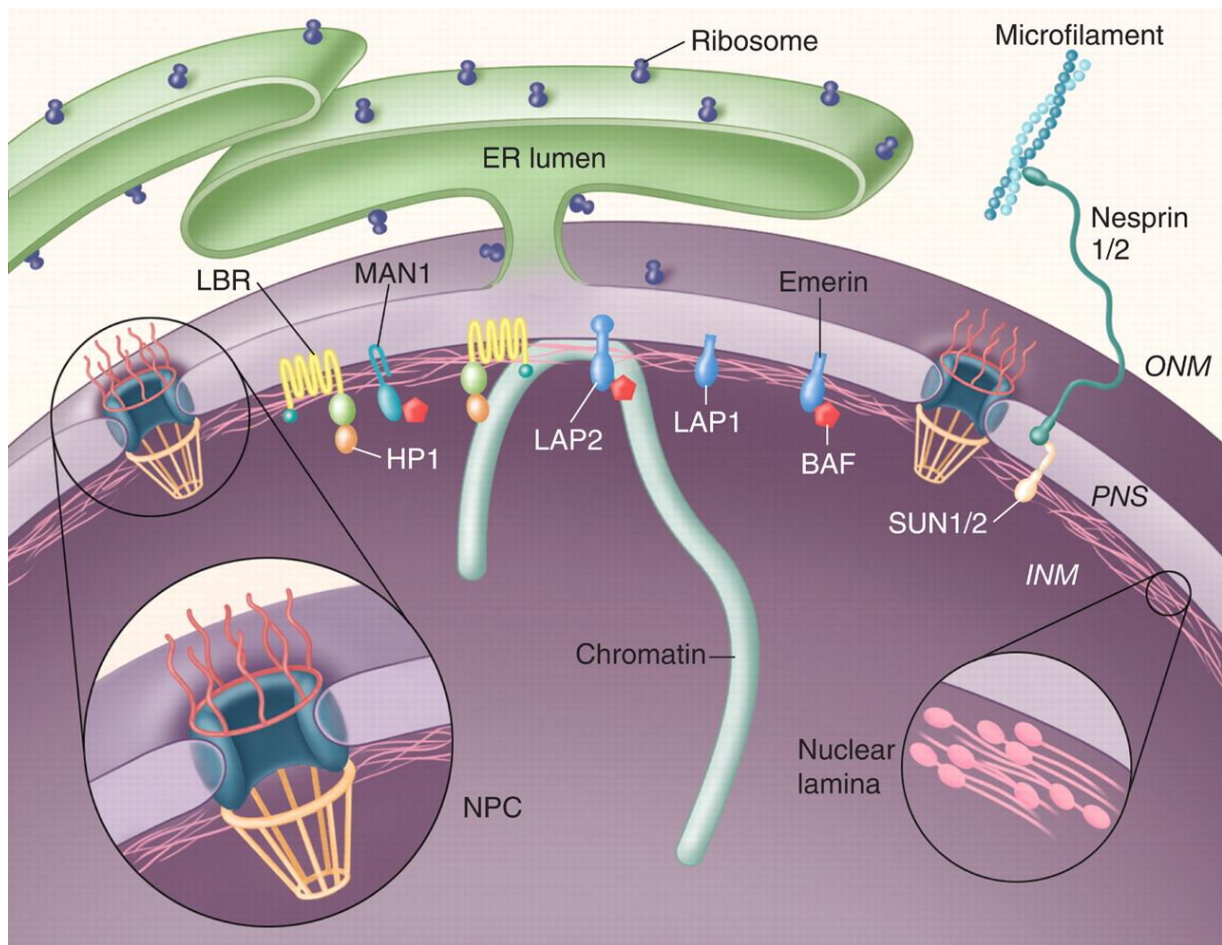


Figure 1-1. Schematic overview of the NE and some of its major constituents. Reprinted from Stewart et al. (2007).¹⁸

Lamin isoforms: expression, prevalence and structure

Nuclear lamins are subdivided into A- and B-type according to their sequence homology, tissue expression pattern and structural properties.¹⁹ A-type lamins are characterized by a neutral isoelectric point, while B-type lamins are rather acidic.²⁰ Lamin A and lamin C are the two major A-type protein isoforms and are alternative splice products of the same gene, namely *LMNA*. Alternative splicing can also produce two less abundant isoforms, lamin A Δ 10 and C2.^{14,19,21} The major B-type lamins are lamin B1 and lamin B2, which are often collectively referred to as lamin B. These proteins are expressed by *LMNB1* and *LMNB2*, respectively. The latter gene also gives rise to the alternatively spliced isoform lamin B3.^{19,20,22} So, the principal lamin isoforms are lamin A, lamin B (B1 and B2) and lamin C. The alphabetical order relates to their respective molecular weight, which is 70 kDa for lamin A, 68 kDa for lamin B2, 67 kDa for lamin B1, and 65 kDa for lamin C.²³

Expression patterns of nuclear lamins are dependent on the stage of development and are cell-type specific. During each stage of development at least one B-type lamin is highly expressed.^{24–26} In contrast, A-type lamins are absent in undifferentiated embryonal stem cells and *LMNA* expression levels correlate with differentiation status.

For example, certain adult cell types that are not fully differentiated produce little or no A-type lamins, such as epithelial cells in the lungs, liver, kidneys, intestine, heart and brains of mouse embryos before birth.^{27,28} Furthermore, most non-hematological malignancies are associated with reduced expression and aberrant localization of A-type lamins.²⁹ Reduced *LMNA* expression can contribute to the proliferative capacity and dedifferentiation ability of cancer cells and has been observed in adenocarcinoma of stomach and colon, squamous and adenocarcinoma of the esophagus, lung cancer, testicular germ cell tumors, and cancerous prostate tissues.²⁹ Conversely, several adenocarcinoma cell lines and carcinoma cell lines show lamin A Δ 10 expression.³⁰ The alternatively spliced isoforms lamin C2 and lamin B3 are exclusively expressed in spermatocytes.^{20,31} Next to the stage of development and differentiation status, the ratio between A- and B-type lamin expression scales with tissue stiffness: stiff tissues, such as bone and cartilage, have nuclei which are rich in A-type lamins, whereas soft tissue, such as brain and liver, have nuclei which are poor in A-type lamins.^{10,32}

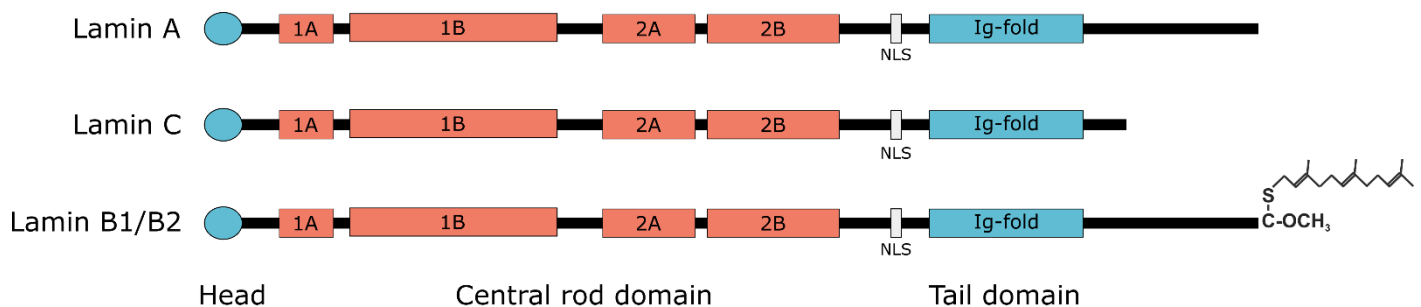


Figure 1-2. Threefold structure of A-type lamins (lamin A/C) and B-type lamins (lamin B1/B2).

Nuclear lamins have been highly conserved throughout evolution.²⁰ Like all intermediate filament proteins, lamins have a typical threefold structure (Figure 1-2). They contain a central highly α -helical coiled-coil rod domain (~50 nm in length), composed of four subhelical regions, flanked by a short (~30 amino acids) globular amino-terminal “head” and a 185-277 residues long carboxy-terminal “tail” domain.^{10,19,20} The subhelical regions in the central domain comprise heptad repeats and are assigned as coil 1A, 1B, 2A, and 2B. The coils are separated from each other by three short linker segments termed L1, L12, and L2.^{19,33} The tail domain contains a globular immunoglobulin fold (Ig-fold), which is 3.5 nm in diameter.^{10,19,34} Between the central rod domain and the Ig-fold, a nuclear localization signal (NLS) can be found, which is required for transport into the nucleus.^{19,35} Similar to most intermediate filament proteins, lamins can self-assemble into higher-order structures. In solution, lamins form coiled-coil dimers by parallel and in-register association of two central rod domains into a left-handed superhelix, exhibiting two Ig-fold domains. Further assembly of the lamin dimers in a head-to-tail fashion results in polarized arrays, which interact in an antiparallel fashion to form apolar tetrameric protofilaments, causing the characteristic beaded appearance of lamin assemblies.^{10,19} Recently, cryo-electron tomography of nuclei of vimentin-null mouse embryonic fibroblasts (MEFs) (to obtain

an unobstructed view of the lamin meshwork) indicated that A- and B-type lamins assemble into tetrameric filaments of 3.5 nm thickness.¹⁰ The assembly of nuclear lamins into dimers, head-to-tail polymers, and protofilaments is shown in Figure 1-3, together with their incorporation into the lamin meshwork. Although the structural assemblies of A- and B-type lamins are very similar, they form distinct networks within the lamina meshwork.^{10,36} However, in MEFs some areas of the lamina present a small amount of overlap between A- and B-type lamins.³⁶

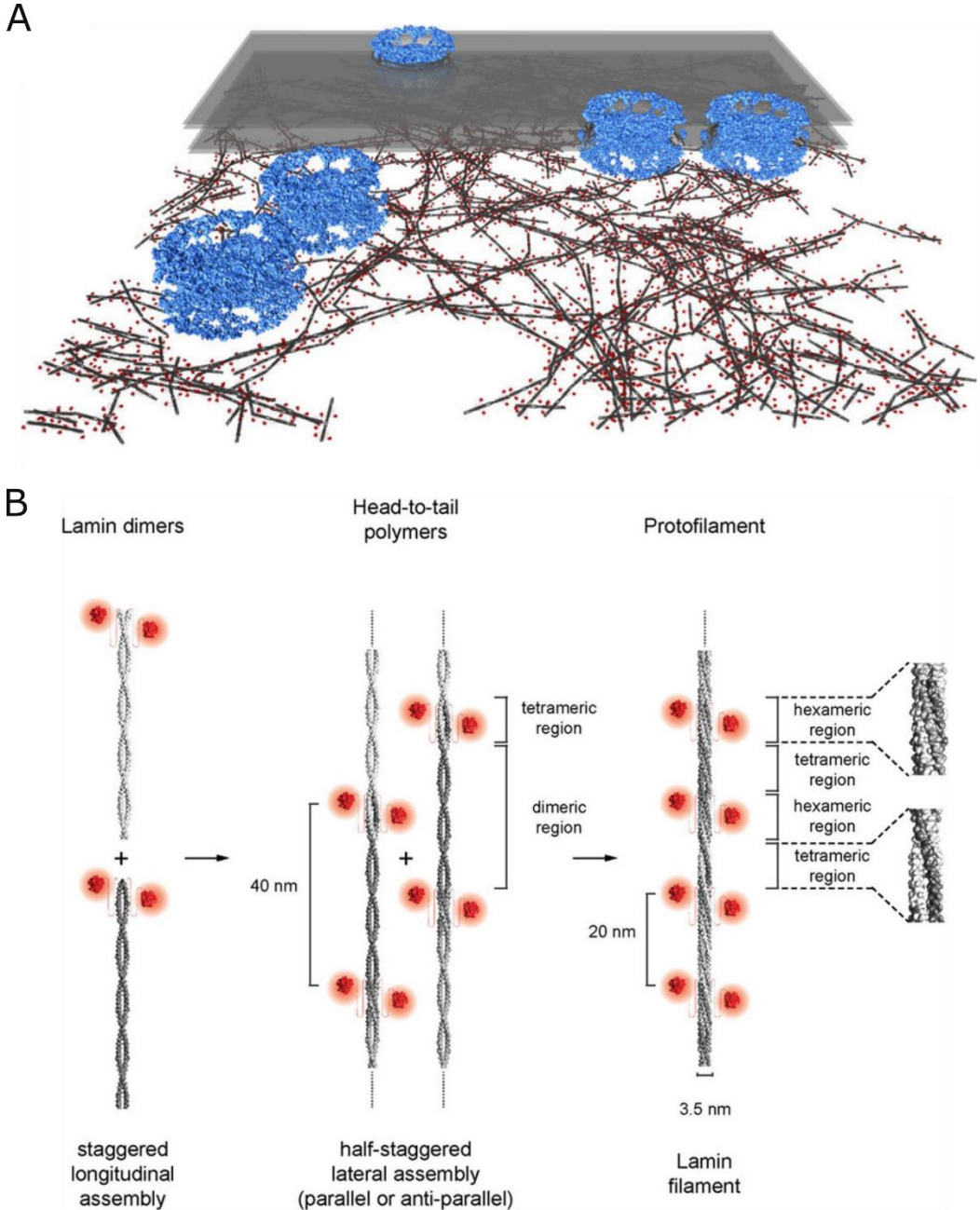


Figure 1-3. A: Cryo-tomogram of the lamin meshwork containing lamins (grey), NPCs (blue) and the INM and ONM (transparent grey). B: Assembly of nuclear lamins into dimers, head-to-tail polymers, and protofilaments. Reprinted from Turgay et al. (2017).¹⁰

Processing and incorporation of lamins into the nuclear lamina

Lamins A, B1 and B2 are produced as precursor proteins (pre-lamins), which all possess a carboxy-terminal CAAX box (C: cysteine; A: aliphatic amino acid; X: random amino acid, typically serine, glutamine, methionine or alanine) that is prone to extensive posttranslational modifications. These modifications are essential for the formation of mature functional lamins.^{19,37,38} The modification of the CAAX box is strictly regulated and starts with farnesylation of the cysteine residue through the action of a farnesyltransferase.³⁸ Next, the AAX residues of the CAAX box are removed by a CAAX prenyl protease (endopeptidase). Two CAAX prenyl proteases have been identified in humans: Ras-converting enzyme 1 (RCE1) and Zinc metalloprotease related to the STE24 homolog in yeast (ZMPSTE24).^{19,39} Subsequently, the carboxy-terminal cysteine is carboxymethylated by isoprenylcysteine carboxyl methyltransferase (ICTM).⁴⁰ Carboxymethylation is the endpoint in the maturation process of B-type lamins. In contrast, prelamin A undergoes a last endoproteolytic cleavage, exclusively catalyzed by ZMPSTE24, after incorporation in the nuclear lamina, resulting in removal of 15 amino acids from the carboxyl terminus, including the farnesylcysteine methyl ester.^{19,39} The maturation process of lamin A, lamin B1 and lamin B2 is shown in Figure 1-4.

Given the fact that lamin maturation is evolutionary conserved, it is highly likely that the pathway serves an important function.⁴¹ Several cell culture studies have suggested that the addition of the hydrophobic farnesyl group to prelamin is important for targeting these proteins to the INM. Furthermore both ZMPSTE24 and ICTM are present in the INM, next to the ER membrane, indicating that their action might take place even after lamin incorporation into the nuclear lamina.⁴¹⁻⁴⁴ However, these studies only focused on prelamin A farnesylation and the importance of B-type lamins has been neglected.⁴⁴ Furthermore, mouse models did not support this notion. For example, knock-in mice that only produce non-farnesylated prelamin A do not show perturbed incorporation of prelamin A.^{41,45} Similarly, lamin C, which is not farnesylated, can be targeted to the nuclear rim in mice that do not produce lamin A.^{41,46} Moreover, bypassing prelamin A synthesis by direct synthesis of mature lamin A in mice, leads to nuclear blebs in MEFs, yet with normal nuclear rim positioning of lamin A in tissue. The occurrence of nuclear blebs in these cells is likely the result of local defects in lamina organization.⁴⁷ A recent study has shown that trafficking of lamin A to and its assembly in the NE is regulated by sorting nexin 6 (SNX6). SNX6-mediated trafficking did not require farnesylation of prelamin A, since mature lamin A was also transported.⁴⁸ In contrast with A-type lamins, farnesylation of lamin B1 has shown to be important for neuronal migration in the developing brain of mice. Knock-in mice expressing non-farnesylated lamin B1 die soon after birth and have striking nuclear abnormalities in neurons: the nuclear lamina appeared pulled away from the chromatin leaving the DNA

exposed in the cytoplasm.⁴⁴ In contrast to lamin A, lamin B1 is not transported by SNX6, therefore farnesylation of lamin B1 is likely essential for INM targeting.⁴⁸

Next to the aforementioned posttranslational modifications, lamins can also be phosphorylated, sumoylated, ADP-ribosylated and possibly glycosylated.¹⁹ For example phosphorylation of lamins by cyclin-dependent kinase 1 (CDK1) and protein kinase C (PKC) is required to trigger disassembly of the nuclear lamina at the onset of mitosis.^{19,23,49,50}

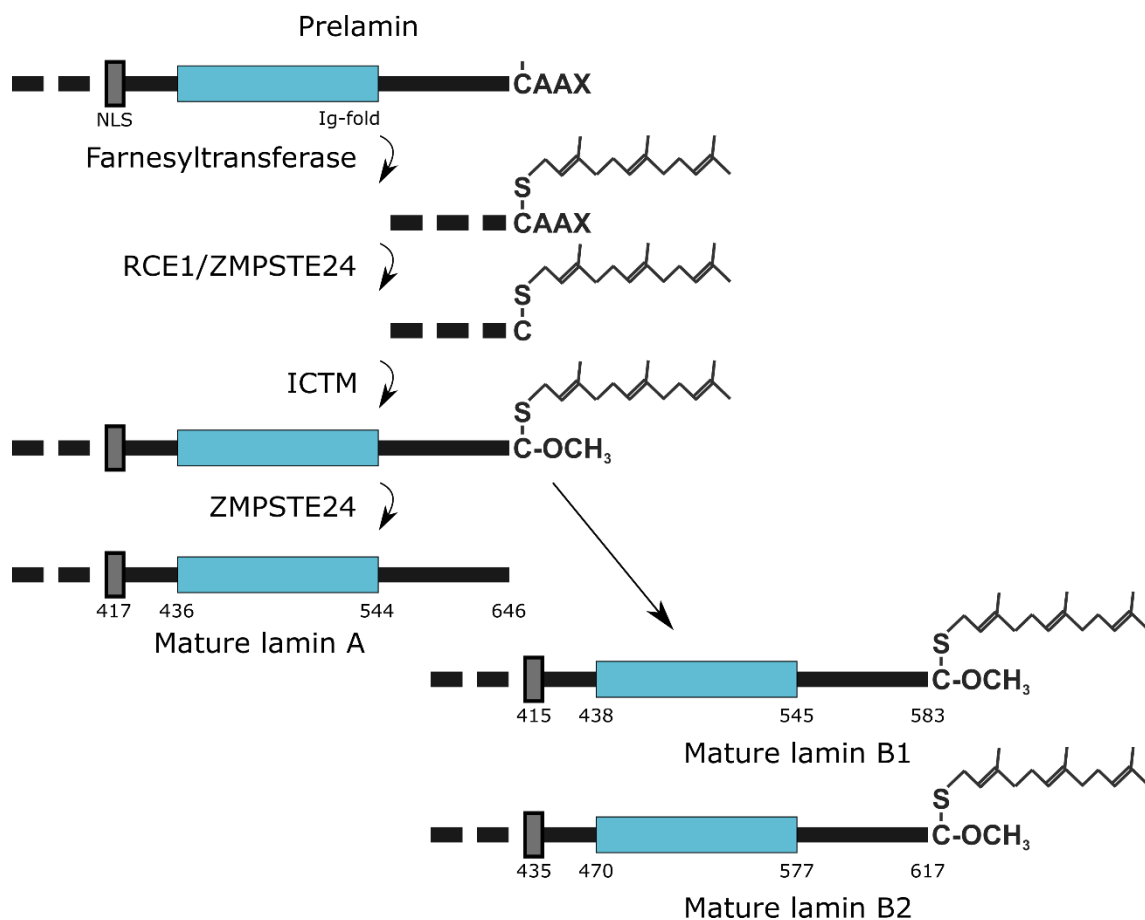


Figure 1-4. Schematic overview of the maturation process of lamin A, lamin B1 and lamin B2. The grey box represents the NLS and the blue box the Ig-fold. The number beneath the lamin structure represent the respective amino acid position. Modified from Dechat et al. (2010).¹⁹

1.1.2. Functions of lamins

Nuclear lamins and their associated proteins play a role in chromatin organization, distribution of NPCs within the NE, positioning of the nucleus in cells and reassembly of the NE after mitosis. They are also involved in essential cellular processes, such as DNA replication and RNA-polymerase-II-dependent gene expression, and interact with proteins involved in a wide range of cellular pathways.⁵¹ Lamins can also function as mediators of oxidative stress, which will be extensively discussed in chapter 2.⁵²

Regulation of nuclear shape and mechanical stability

Similar to cytoplasmic intermediate filaments, nuclear lamins have a mechanical role. More specifically, lamins provide and maintain structural stability of the nucleus. A-type and B-type lamins have a different effect on the mechanical properties of the nucleus. Lamin B1-deficient MEFs exhibit normal nuclear mechanics, although a significant increase in nuclear blebs is observed.⁵³ In contrast, cells lacking A-type lamins exhibit increased numbers of misshapen nuclei and have increased nuclear plasticity.⁵⁴ Furthermore, nuclei in *Lmna*^{-/-} MEFs are more prone to mechanical stress causing increased nuclear dysmorphism and decreased viability. These cells also show decreased mechanical stiffness. Overexpression of lamin A or lamin C can partly restore the phenotype of *Lmna*^{-/-} MEFs.^{19,55–57} Nuclear deformability is also observed in embryonic stem cells that lack expression of A-type lamins. After terminal differentiation there's a 6-fold increase in nuclear stiffness.^{19,58} Next to the lack of lamin A/C, production of mutant lamin A isoforms, such as progerin, or accumulation of prelamin A, as observed in certain diseases (discussed later on), can result in dysmorphic nuclei. Most common nuclear abnormalities observed are honeycombs, blebs, donut-like nuclei.^{14,57,59–61} An exponent of the enfeebled nucleus is the occurrence of nuclear ruptures, temporary breaches of the NE barrier, in cells lacking A-type lamins, and to a lesser extent in cells expressing mutant lamin A isoforms.⁶²

The nuclear lamina is also connected with the cytoskeleton through the “link of nucleoskeleton and cytoskeleton” (LINC) complex (see Figure 1-1). This complex bridges the perinuclear space and consists of SUN1 and/or SUN2 proteins bound to KASH proteins (nesprin1-4), which localize to the INM and ONM, respectively.^{4,63} A-type lamins interact with SUN1/2, which are connected to cytoplasmic actin filaments through nesprin 1 and 2.¹⁸ Furthermore, biochemical studies have shown that A-type and B-type lamins can bind directly to actin filaments.⁶⁴ Nesprin 3 connects intermediate filaments with SUN1/2 through the binding of plectin, and in *Caenorhabditis elegans* it has been shown that ZYG-12 connects microtubules to the nucleus through dynein.⁶⁵

Chromatin organization and positioning

By regulating chromatin organization, nuclear lamins influence gene expression and cell differentiation.⁶⁶ Gene-poor chromatin regions and heterochromatin are preferentially located around the nucleoli and at the nuclear periphery in eukaryotic cells.^{67,68} Nuclear lamins interact with chromatin directly by binding DNA or indirectly by binding DNA-associated proteins. More specifically, DNA sequences in matrix attachment regions (MARs) can be bound by lamins via their rod domain.^{69,70} DNA-associated proteins include histone proteins, barrier to autointegration factor (BAF), LEM-domain proteins (lamina associated polypeptide 2 (LAP2), emerin, MAN1), or lamin B receptor (LBR).^{51,71–73}

Genomic regions associated with the nuclear lamina are termed lamina-associated domains (LADs). These regions are anchored to the nuclear lamina by lamin B1 and

are typified by low gene expression and heterochromatin specific histone markers. LADs range from 0.1-10 Mb in size and contain all together thousands of genes.^{74,75} Genes in LADs are 5- to 10-fold less active than genes outside LADs and the mean gene density outside LADs is about twice the gene density inside LADs. These domains are confined and demarcated by the insulator protein CCCTC-binding factor (CTCF), by outward oriented promoters, or by CpG islands.⁷⁴ In replicative senescent cells *LMNB1* expression is significantly decreased. This is accompanied by large-scale changes in gene expression and chromatin reorganization.⁷⁶ However, the changes in gene expression can also be attributed to altered sequestration of transcription factors, as discussed later on.

In contrast to lamin B1, lamin A/C preferentially associates with gene-rich chromatin regions, and disruption of lamin A-dependent heterochromatin tethering results in decreased expression of muscle genes in mouse myoblasts.^{19,68,77} The amount of heterochromatin at the nuclear periphery is also significantly reduced in lamin A/C-deficient fibroblasts and central chromosome territories are more condensed and repositioned closer to the nuclear gravity center.⁷⁸ Furthermore, loss of A-type lamins alters genome dynamics, inducing a dramatic transition from slow anomalous diffusion to fast and normal diffusion.^{54,79} Similarly, fibroblasts from Hutchinson-Gilford Progeria Syndrome (HGPS) patients, which express a truncated, permanently farnesylated form of prelamin A (progerin), exhibit a dramatic loss of heterochromatin. These changes are accompanied by alterations in histone modifications, like a decrease of H3 trimethylated on lysine 9 (H3K9me3) and H3K27me3. Remarkably, an increase in H4K20me3 was observed, an epigenetic mark for constitutive heterochromatin.⁸⁰ Interference with proper lamin A processing also causes alterations in chromatin organization. For example, inhibition of prelamin A farnesylation, by the farnesyltransferase inhibitor FTI-277, causes redistribution of heterochromatin domains at the nuclear interior. On the other hand, The ZMPSTE24 inhibitor N-acetyl-S-farnesyl-L-cysteine methylester (AFCMe) causes loss of heterochromatin domains, comparable to the observations in HGPS fibroblasts.⁸¹

Taken together, nuclear lamins are indispensable for proper chromatin organization, and in addition they have a strong effect on epigenetic histone modification. Altered lamin levels induce chromatin redistribution, which eventually results in altered gene expression.

Mitosis, DNA replication and DNA damage repair

Nuclear lamins are involved in DNA replication. Observations in primary fibroblasts indicated that DNA synthesis is initiated in a limited number of foci containing nucleoplasmic lamin A/C and retinoblastoma protein (pRb) family members, which surround the nucleoli.⁸² Lamin B1 has also been associated with replication foci in mouse 3T3 cells during late synthesis phase.⁸³ Lamins can also bind directly with proliferating cell nuclear antigen (PCNA) through their Ig-fold motif. This protein is necessary for the chain elongation phase of DNA replication. Interestingly, an excess

of the lamin domain containing the Ig-fold can inhibit DNA replication in a concentration-dependent fashion.⁸⁴ Besides it has been shown that lamin A/C has a role in the restart of stalled replication forks, since replication restart is defective in *Lmna*-deficient MEFs after induction of replication stress.⁸⁵

During mitosis, during the transition from prophase to prometaphase, the nuclear lamina disassembles through phosphorylation of lamins and A-type lamins become freely soluble, in contrast B-type lamins remain associated with nuclear membrane structures through LBR.^{14,86}

Nuclear lamins also influence DNA repair. Loss of A-type lamins induces an increase in the number of DNA damage repair foci, containing phosphorylated H2AX (γ H2AX), pointing at an increase in DNA damage.⁸⁷ Nuclear ruptures can contribute to this increase in DNA damage, as observed in migrating lamin A-depleted cancer cells.^{88,89} In addition, lamin A/C deficiency was associated with an increase in aneuploidy, chromosomal aberrations, telomere shortening and redistribution of telomeres at the nuclear periphery.^{90,91} It has been shown that loss of A-type lamins results in upregulation of cathepsin L (CTSL) expression, which induces a decrease in DNA double strand breaks (DSB) repair via non-homologous end joining (NHEJ).^{90,91} Next to CTSL, BRCA1 and RAD51 also show decreased gene expression, resulting in decreased DSB repair through homologue recombination.^{90,91} The aforementioned stalled replication forks in *Lmna*^{-/-} MEFs is caused by defective recruitment of repair factors (Mre11, CtIP, Rad51, RPA, and FANCD2), which delays the removal of γ H2AX foci.⁸⁵ Similar to A-type lamin depletion, expression of disease-causing lamin A mutants has been linked to increased DNA damage and chromosomal aberrations and an increased susceptibility to genotoxic agents.^{92,93} HeLa cells expressing lamin A mutants exhibited a decrease in γ H2AX foci, when exposed to cisplatin or UV irradiation. Likely this is caused by mislocalization and/or impaired expression of ataxia-telangiectasia- and Rad3-related protein (ATR), which is involved in DNA damage sensing. A decrease in γ H2AX foci in turn, results in impaired recruitment of p53-binding protein 1 (53BP1).⁹³ Recruitment of 53BP1 and RAD51 to DNA damage foci is also impaired in *Zmpste24*^{-/-} MEFs and in HGPS fibroblasts. This results in a delayed checkpoint response and inconsistent DNA damage repair. Wild-type MEFs ectopically expressing unprocessable prelamin A (carboxyl-terminal Ser-Ile-Met was replaced by Phe-Phe-Met) show similar defects in checkpoint response and DNA damage repair.⁹² Furthermore, experiments in *Zmpste24*^{-/-} mice have shown that prelamin A accumulation is responsible for p53 activation, and results in cellular senescence. The progeroid phenotype are largely rescued in *Zmpste24*^{-/-} *Lmna*^{+/-} mice and partially reversed in *Zmpste24*^{-/-} *p53*^{-/-} mice.⁹⁴

Transcription, gene regulation and mechanotransduction

As mentioned before, both A-type and B-type lamins influence gene expression through chromatin organization. However nuclear lamins can also regulate expression of specific genes directly, by sequestering transcription factors at the INM.^{31,95} For example, sequestration of c-Fos by lamin A/C prevents dimer formation between c-Fos

and c-Jun, which in turn suppresses Activation protein 1 (AP1) transcription factor activity.⁹⁶ In line with this *Lmna*^{-/-} MEFs exhibit increased AP-1 activity.^{96,97} AP-1 is involved in multiple essential cellular processes, including cell proliferation and differentiation. Lamin A/C can also interact directly with the transcription factor MOK2 and prelamin A specifically binds sterol regulatory element-binding protein 1 (SREBP1).⁹⁸⁻¹⁰⁰ Sequestration of these transcription factors represses transcription of their respective target genes.^{95,98,100} More specifically, sequestration of SREBP1 by prelamin A induces a decreased expression of peroxisome proliferator-activated receptor- γ (PPAR γ), which is involved in cholesterol metabolism.^{95,100} Lamin B1 can associate with octamer-binding transcription factor-1 (OCT1) at the nuclear periphery. Again this anchorage represses expression of OCT1 target genes.¹⁰¹ Besides direct interaction with transcription factors, lamins can also interact with transcription factors via lamin-associated proteins such as emerin, MAN1, LAP2 β , and pRb. For example, emerin regulates β -catenin activity by restricting its accumulation in the nucleus, and MAN1 can interact with SMADs and thereby antagonizes bone morphogenetic protein (BMP)- and transforming growth factor beta (TGF β)-signalling.^{31,95,102,103}

Nuclear lamins are also involved in mechanotransduction. Mechanotransduction can be defined as the intracellular signaling response of cells to mechanical stimuli.¹⁰⁴ This signal transduction plays an important role in maintaining tissue function, in particular in mechanically active tissues such as myocardium and skeletal muscle. Mutations in NE proteins such as nuclear lamins or emerin, can perturb mechanotransduction.¹⁰⁵ For example, lamin A/C-deficient fibroblasts show attenuated NF κ B-regulated transcription in response to mechanical or cytokine stimulation, despite increased transcription factor binding. Next to attenuated NF κ B-regulated transcription, *LMNA* mutations have been associated with hyperactivation of extracellular signal-regulated kinase 1/2 (ERK1/2) in fibroblasts.¹⁰⁶ Abnormally increased ERK1/2 activity has also been observed in hearts of *Lmna*^{H222P/H22P} mice, a mouse model for Emery-Dreifuss muscular dystrophy (EDMD).^{107,108} ERK1/2 are protein kinases that participate in the mitogen-activated protein kinase (MAPK) pathway, which is involved in mechanotransduction in various cell types.^{104,109} Next to increased susceptibility to mechanical stress, perturbed mechanotransduction contributes to the phenotype of muscular dystrophy, which is associated with multiple *LMNA* mutations.⁵⁵

1.1.3. Laminopathies

Mutations in lamins that lead to reduction of mature lamins and/or accumulation of aberrant immature prelamins, can induce a wide range of diseases, which are collectively termed laminopathies. These diseases belong to a larger family of nuclear envelopathies, which also cover diseases caused by mutations in genes encoding other NE proteins, such as emerin (*EMD*), *LBR*, *MAN1*, *LAP2*, and aladin WD repeat nucleoporin (*AAAS*).¹⁴ Most laminopathies are related to A-type lamins, since mutations in B-type lamins are most often lethal.^{110,111} Therefore, we will only discuss *LMNA*-related laminopathies. *LMNA*-related laminopathies can be subdivided in primary laminopathies, which are caused by mutations in the *LMNA* gene, and

secondary laminopathies which are caused by mutations in genes encoding prelamin-processing proteins, e.g. *ZMPSTE24*.¹⁴ About 350 disease-associated point mutations have been identified in the *LMNA* gene. The majority of these mutations, almost 90%, are missense mutations distributed throughout the gene.^{112,113} The bulk of these mutations are autosomal dominant and can be inherited or congenital.¹¹⁴ Disease-causing mutations can either be haploinsufficient loss-of-function mutations or dominant negative gain-of-function mutations. For example, limb girdle muscular dystrophy 1B (LGMD1B) has been associated with dominant loss-of-function mutations, while HGPS is caused by dominant negative gain-of-function mutations, resulting in the accumulation of progerin. There are currently 17 distinct diseases described which are linked to mutations in the *LMNA* gene including dilated cardiomyopathy (DCM), muscular dystrophy, Charcot-Marie-Tooth peripheral neuropathy type 2B1 (CMT-2B1), lipodystrophy and premature aging syndromes.¹¹³ So, disease manifestations can be systemic or tissue-specific. Among the muscular dystrophies we have EDMD and the aforementioned LGMD1B, these diseases also present DCM.^{115,116} Lipodystrophy syndromes include Dunnigan-type familial partial lipodystrophy (FPLD) and mandibuloacral dysplasia with type A lipodystrophy (MADA).^{117,118} Premature aging syndromes include HGPS, atypical Werner syndrome (AWS), and atypical progeroid syndromes (APS).^{119–122} Noteworthy, some MADA patients also exhibit accelerated aging and progeroid syndromes show generalized lipodystrophy, suggesting common pathological mechanisms.^{123–125} *ZMPSTE24*-related secondary laminopathies include mandibuloacral dysplasia type B (MADB), which is distinguished from type A by the pattern of fat distribution throughout the body, atypical HGPS and the lethal neonatal disease restrictive dermopathy (RD).^{31,126–131} Premature aging syndromes have the earliest onset, worst outcome, and are very hard to treat. DCM patients, on the other hand, present symptoms at later age and standard care for heart failure is applied.¹³² Hence, next to the affected tissues, the severity and onset of laminopathies are highly variable. Laminopathies caused either by decreased lamin A/C expression or prelamin A accumulation will be discussed in more detail, since these diseases are more relevant in the context of this thesis.

Molecular mechanisms underlying laminopathies

Different mechanisms have been proposed to explain the pathogenesis of laminopathies. According to the “structural mechanism”, loss of A-type lamin function affects structure and rigidity of the cell nucleus, causing nuclear ruptures and decreasing resistance to mechanical stress. This has been described in A-type lamin deficient cells, and is one of the underlying mechanisms in muscular dystrophies and DCM.^{14,19,55–57} The “cell proliferation mechanism” is based on the observation that most laminopathies are characterized by impaired cell proliferation. For example, fibroblasts from progeria patients and progeria mouse models show premature senescence.^{133,134} Next to cell proliferation, cell differentiation can be impaired. Mutations in *LMNA* can perturb interaction with pRb, impairing myoblast differentiation and promoting apoptosis.¹³⁵ The latter can also contribute to the pathogenesis of muscular dystrophies and DCM. According to the “gene expression mechanism”, pathogenesis

is a result of changes in gene expression due to altered interaction between nuclear lamins and transcription factors and impaired chromatin organization. This can influence multiple cellular processes. For example, accumulation of prelamin A can affect lipid metabolism through permanent SREBP1 sequestration^{95,100}, or loss-of-function mutations can impair mechanotransduction, as observed in muscular dystrophies. Next to altered sequestration of transcription factors or impaired chromatin organization, gene expression can also be altered by nuclear ruptures, through temporal molecular exchange between the cytoplasm and the nucleus. This can result in redistribution of transcription factors to the cytoplasm or to the nucleus and thereby affect gene expression.^{61,62} Finally the “toxicity mechanism” claims that accumulation of mutant lamin isoforms, such as progerin, or prelamin A is cytotoxic. Indeed accumulation of these proteins induces nuclear shape defects and is associated with cellular senescence and oxidative stress.^{136–138}

Laminopathies caused by haploinsufficiency of A-type lamins

The most prevalent laminopathy is DCM. Idiopathic DCM affects 1 in 2500 individuals and 50% of all cases of idiopathic DCM are familial dilated cardiomyopathy (FDM).^{139,140} It has been estimated that 8% of all FDM cases are caused by mutations in *LMNA*, thus approximately 1 case in 62500 individuals suffers from *LMNA* DCM.¹³⁹ In the case of EDMD and LGMD1B, DCM is accompanied by different types of skeletal muscular dystrophy. EDMD patients are characterized by early tendon contractures, progressive muscle weakness and wasting in a humeroperoneal distribution.¹⁴¹ In LGMD1B patients more proximal skeletal muscles are affected compared to EDMD patients.¹¹⁶ *LMNA* DCM, EDMD and LGMD1B are all adult-onset diseases, and are actually a spectrum of the same diseases and can be caused by the same *LMNA* mutations.¹⁴² They have a high penetrance (100% of mutation carriers are affected by the age of 60 years) and aggressive course, often resulting in premature death or cardiac transplant.¹⁴² In line with the majority of laminopathies, *LMNA* DCM is primarily autosomal dominant and mainly caused by missense mutations. One homozygous missense mutation (H222Y) in *LMNA* has been linked to EDMD.¹¹⁵ LGMD1B has been associated with a mutation leading to truncation of lamin A/C (Y259X), resulting in a neonatal lethal phenotype in case of homozygous inheritance. *LMNA*^{Y259X/Y259X} patients lack *LMNA* expression, so loss of lamin A/C function likely contributes to the phenotype of LGMD1B patients.¹⁴³ This is supported by experiments in *Lmna*-null and *Lmna*^{+/-} mice, which suggest that haploinsufficiency underlies the pathogenesis of *LMNA* DCM.^{144,145} Next to lack of expression, some mutations interfere with the protein structure of A-type lamins, and thereby impair protein function. For example the R453W mutation in *LMNA*, causing EDMD, destabilizes the three-dimensional structure of the Ig-fold in the carboxyl-terminal tail domain of lamin A/C.¹⁴⁶

Loss of functional lamin A/C decreases mechanical stability of the nucleus, initially affecting tissues under high mechanical stress, such as striated muscles and heart muscle. In addition, mechanotransduction is impaired through attenuated NFκβ-regulated transcription and hyperactivation of ERK1/2, as mentioned earlier.^{105–108} So

the primary molecular mechanisms underlying this group of laminopathies are the structural and gene expression mechanisms, including nuclear ruptures, as discussed earlier on.

Laminopathies characterized by prelamin A accumulation

ZMPSTE24 related secondary laminopathies, such as MADB and RD, are caused by accumulation of farnesylated prelamin A, since the final endoproteolytic cleavage is inhibited. Both diseases are autosomal recessive and can be caused by homozygous or compound heterozygous mutations.^{126,127} Interestingly, MADB is accompanied by partial loss of *ZMPSTE24* activity, while RD is associated with complete loss.¹²⁹ So the degree of prelamin A accumulation correlates with the severity of the disease. MADB is characterized by skeletal abnormalities and generalized lipodystrophy with metabolic syndromes such as insulin resistance, glucose intolerance, diabetes mellitus and hypertriglyceridemia. Some patients have features of premature aging.^{117,126} RD is a lethal neonatal genodermatosis characterized by intrauterine growth retardation, tight, rigid and easily eroded skin with prominent superficial vessels, bone mineralization defects, dysplastic clavicles, arthrogryposis and early neonatal death. RD patients usually die within several hours or days of birth.^{126,127} Prelamin A accumulation has also been observed in primary laminopathies, including FPLD, MADA and AWS.^{100,147} However, a recent study could not recapitulate these results in fibroblasts from different FPLD patients (heterozygous R482W, I299V, C591F, and T528M mutations).¹⁴⁸ Furthermore, fibroblasts from different APS patients (heterozygous P4R, E111K, D136H, E159K, and C588R mutations) do not show prelamin A accumulation, questioning the observed prelamin A accumulation in AWS.¹²² On the other hand, prelamin A accumulation could be reconfirmed in fibroblasts from MADA patients (homozygous R527H mutation) in a later study.¹⁴⁷ In contrast to MADB patients, MADA patients only present fat loss from the extremities of the body, and have normal or a slight excess in subcutaneous fat in the neck and truncal regions.¹³¹ HGPS is, without a question, the most notorious laminopathy. Children affected with HGPS appear healthy at birth. Within a year, the first clinical features of this progeroid syndrome appear, including failure to grow, delayed dentition, alopecia, loss of subcutaneous fat and sclerodermatous skin changes.^{14,125} The age of death ranges between 7 and 27.5 years, with a median age of 13.4 years. Most patients die from progressive arteriosclerosis of the coronary and cerebrovascular arteries.^{14,125} The syndrome is mainly caused by a *de novo* single-base substitution, G608G (GGC > GGT), within exon 11. This mutation does not affect amino acid sequence, but results in activation of a cryptic splice site within exon 11. Splicing results in the production of progerin, a prelamin A isoform which lacks 50 amino acids near the carboxyl terminus.¹²⁵ Progerin still contains the CAAX box and becomes farnesylated during posttranslational processing. However, the deleted 50 amino acids contain the *ZMPSTE24* cleavage site, so removal of the last 15 amino acids, including the farnesyl group, is impossible. Thus, progerin remains permanently farnesylated and accumulates at the nuclear rim.¹⁴⁹

MADA, MADB, RD and HGPS have overlapping phenotypes. Except for RD patients, MADA, MADB and HGPS patients present partial or generalized lipodystrophy.¹⁰⁰ Interestingly, RD patients have a slight increase in subcutaneous fat as well.^{119,150} Since RD is a lethal neonatal disease, it's likely that lipodystrophy is not yet presented. At cellular level these diseases all display nuclear shape defects to some extent. In MADA fibroblasts, prelamin A accumulates at the nuclear rim and at the nucleoplasmic reticulum. In addition, the LINC complex protein SUN2 is mislocalized and forms a honey-comb-like lattice in the nuclear membrane.¹⁴⁷ MADB fibroblasts show major nuclear shape defects, such as lobulations and herniations. However lamin A/C is still localized at the nuclear rim.¹²⁶ In RD patient fibroblasts nucleoplasm herniation and NE irregularities are observed, furthermore lamin A/C is distributed in clusters in the nucleus.^{119,127} HGPS fibroblasts show clear abnormalities of the nuclear membrane.¹²⁵ In addition ectopic expression of progerin in mice results in misshapen nuclei and nuclear blebs.¹⁵¹ So, accumulation of either farnesylated prelamin A or farnesylated progerin is toxic and affects nuclear shape, in line with the "toxicity mechanism" mentioned earlier. Of note, prelamin A and progerin are also present in healthy cells at very low levels. Interestingly, the amount of progerin increases with aging.^{152,153} Likely, progressive telomere damage during aging results in the release of certain telomere-binding/capping proteins which influence spliceosome function, and thereby induces extensive changes in alternatively splicing, eventually increasing progerin production.¹⁵³ Similarly prelamin A accumulates in hMSC during aging. This is caused by reduced *ZMPSTE24* expression, induced by the overexpression of miR-141-3p during senescence.¹⁵⁴ So, the aforementioned laminopathies partly reflect normal aging.

Therapeutic strategies for laminopathies

To date, no curative treatments exist for laminopathies. For muscular dystrophies and DCM the primary concern is preventing sudden cardiac death.¹³² To this end standard care for heart failure is applied, which includes angiotensin-converting enzyme inhibitors, angiotensin receptor blockers, beta-blockers, diuretics and aldosterone antagonists. As mentioned before a cardiac transplant is often a requisite.¹⁴² Potential new treatments include MAPK inhibitors (e.g. Selumetinib), to lower the abnormally increased ERK1/2 activity, and induction of autophagy (e.g. Temsirolimus), which improved cardiac function of *Lmna*^{H222P/H222P} mice.¹³² Combination treatments can further improve efficacy.¹³² MADA, MADB, RD and HGPS patients can benefit from blocking the farnesylation of prelamin A or progerin. This can be achieved by inhibiting farnesyltransferase. Farnesyltransferase can be blocked by farnesyltransferase inhibitors (FTIs). One specific FTI, lonafarnib, has been studied in children with HGPS up to a phase II clinical trial.¹⁵⁵ However, due to alternative prenylation of the CAAX box by geranylgeranyltransferase I the effect of FTIs can be reduced.^{38,156} Furthermore FTI treatment can trigger the formation of donut-shaped nuclei. This phenotype is caused by a centrosome separation defect.⁵⁹ Instead of directly inhibiting farnesyltransferase or geranylgeranyltransferase I, interfering with the mevalonate

pathway is more effective. Blocking this pathway minimizes the synthesis of the non-sterol isoprenoids farnesyl pyrophosphate (FPP) and geranylgeranyl pyrophosphate (GGPP), eventually preventing the action of farnesyltransferase and geranylgeranyltransferase I upstream.¹⁵⁷ To this end, statins (e.g. pravastatin) or aminobisphosphonates (e.g. zoledronate) can be used.¹⁵⁶ Statins inhibit 3-Hydroxy-3-methylglutaryl coenzyme A (HMG-CoA) reductase, which is essential for the biosynthesis of mevalonate, and thereby reduce FPP and GGPP, leading to a reduction in protein farnesylation.¹⁵⁷ Aminobisphosphonates inhibit two enzymes in the mevalonate pathway, namely FPP synthase and/or isopentenyl pyrophosphate (IPP).¹⁵⁷ Statin treatment of MADA fibroblasts rescues SUN2 mislocalization and combined statin/aminobisphosphonate treatment improves the aging-like phenotype in *Zmpste24*-deficient mice and improved nuclear abnormalities in HGPS fibroblasts.^{147,156} Although interference with lamin farnesylation is a promising treatment strategy, these strategies also interfere with the farnesylation of other proteins, such as Ras proteins, causing unwanted side effects. Therefore, a number of alternative therapies have been put forward. Rapamycin, a macrolide antibiotic, has been shown to reverse the cellular phenotype of HGPS fibroblasts, through progerin clearance via autophagy.¹³⁸ Rapamycin also decreased the level of farnesylated prelamin A in RD and MADA fibroblasts, and alleviated the nuclear shape defects observed in these cells.¹⁵⁸ More recently, sulforaphane, an antioxidant derived from cruciferous vegetables, was tested on HGPS fibroblasts. Sulforaphane enhanced proteasome activity and autophagy in both healthy and HGPS cells. The treatment resulted in increased progerin clearance, similar to rapamycin.¹⁵⁹ Another approach to reduce progerin or prelamin A accumulation is redirection of the alternative splicing of *LMNA* towards lamin C. To this end metformin can be used. This antidiabetic drug decreases SRSF1 expression, an RNA-binding protein which is involved in alternative splicing of *LMNA*. Through reduced SRSF1 expression, progerin expression is decreased.¹⁶⁰ Finally it has been shown that resveratrol can ameliorate the phenotype of *Zmpste24*^{-/-} mice and extend their lifespan. Resveratrol enhances the binding capacity between SIRT1, a NAD⁺-dependent histone and non-histone protein deacetylase, and A-type lamins, including prelamin A and progerin. Thereby SIRT1 is activated and physiological and metabolic functions necessary for health span are restored.^{161,162}

1.2. Modern tools for cell biology

The past decade, modern cell systems or cytomics approaches have boosted the progress in life sciences. High throughput DNA sequencing technologies have permitted the discovery of thousands of novel disease-causing mutations and more recently, RNA sequencing has enabled exhaustive analysis of the coding and non-coding transcriptome. Advances in mass spectrometry allowed high-throughput protein sequencing. Despite the holistic nature of genome- and proteome-wide approaches, which can inventorize all molecular changes upon specific perturbations or in pathologies, they do not provide insight into the location and dynamics. In other words,

they all lack spatiotemporal resolution. This gap can be bridged by the use of microscopy. In recent years there has been a surge in microscope automation, resulting in huge amounts of data. Along with this, there has a trend towards automated analysis of the resulting large image data sets. This has led to the development of a new field, called systems microscopy.

1.2.1. Genomics

The first DNA sequencing technology was developed in 1968, fifteen years after the discovery of the double helix by Francis H. Crick and James D. Watson.¹⁶³ A decade ago the overwhelming majority of DNA sequencing relied on some version of the dideoxy method of Sanger.¹⁶⁴ This method relies on the use of fluorescently (four colors) labelled chain-terminating nucleotide analogs, namely dideoxynucleotides (ddNTPs), to cause base-specific termination of primed synthesis by DNA polymerase.^{163,164} Sanger-based methods are termed first-generation sequencing. Newer methods are referred to as next-generation sequencing (NGS).¹⁶⁵ These newer methods have the ability to produce an enormous volume of data, compared to first-generation sequencing.¹⁶⁵ Second-generation sequencing include Roche/454 pyrosequencing and Illumina/Solexa sequencing. In Roche/454 pyrosequencing DNA is randomly sheared and ligated to linker sequences, which are captured on the surface of beads. The sequences are amplified within an emulsion droplet. During primed DNA synthesis each of the four dNTPs are sequentially presented, and incorporation is monitored by luminometric detection of pyrophosphate release (hence the name pyrosequencing).¹⁶³ In Illumina/Solexa sequencing template DNA is immobilized and amplified via bridge amplification.¹⁶⁵ Sequencing is based on cyclic reversible termination (CRT). This method relies on the use of reversible chain-terminating nucleotides, which contain a terminating/inhibiting group and a fluorescent dye (for each nucleotide a specific color). These reversible terminators are incorporated during primed DNA synthesis, and after a washing step incorporated nucleotides can be identified by imaging. A cleavage step removes the terminating group, including the fluorescent dye, and after a washing step, the cycle can be repeated.¹⁶⁵ Third-generation sequencing technologies are Single Molecule Real Time (SMRT) sequencing by Pacific Biosciences, the Illumina Tru-Seq Synthetic Long-Read technology, and the Oxford Nanopore Technologies sequencing platform. This last generation is characterized by high-quality genome sequencing with very long reads.¹⁶⁶ Next to DNA sequencing, NGS can be used for sequencing of RNA and microRNA. Nowadays RNA sequencing even replaces microarray-based gene expression studies.¹⁶⁵

1.2.2. Proteomics

Proteomics is the large-scale analysis of proteins in a cell, tissue, or whole organism. Proteomics as a technology is now over 20 years old and offers several advantages over genomics as it directly measures the functional molecules, which are the result of transcription, translation, and post-translational modifications.¹⁶⁷ Proteomics can be

subdivided in gel-based applications, such as one-dimensional and two-dimensional polyacrylamide gel electrophoresis (PAGE), and gel-free methods based on tandem mass spectrometry (MS/MS).¹⁶⁸ Gel-based methods identify proteins based on their molecular weight and in the case of two-dimensional PAGE also on their IEP. In contrast MS/MS-based methods can identify proteins through peptide-to-spectrum matching. In this process theoretic spectra are generated through *in silico* digestion of protein sequences and compared to the detected spectra. This can be performed by several search engines such as Mascot, X!Tandem, and OMSSA. Some proteomic methods can also provide quantitative information in a label-based or label-free manner. Label-based methods can be further subdivided into the various types of labeling approaches such as chemical and metabolic labeling.¹⁶⁷ Chemical labeling methods include proteolytic labeling (¹⁸O stable-isotope labeling), isotope-coded affinity tags (ICAT), isotope-coded protein labeling (ICPL), isobaric tags for relative and absolute quantification (iTRAQ), and tandem mass tags (TMT). Metabolic labeling methods include stable isotope labeling by amino acids in cell culture (SILAC).¹⁶⁷ The principle of iTRAQ- and SILAC-based quantitative proteomics is shown in Figure 1-5. In recent years, label-free methods have sparked interest. These methods are based on spectral counting and provide the deepest proteome coverage for identification, however its quantification performance is worse than label-based approaches. Both chemical and metabolic labeling are capable of accurate, precise, and reproducible quantification and provide deep proteome coverage for quantification.¹⁶⁹ Next to general proteomics, specific posttranslational modifications can be analyzed by “modification-specific proteomics”. In modification-specific proteomics posttranslational modified proteins are enriched prior to analysis, such as phosphopeptides (phosphoproteomics), glycopeptides (glycoproteomics), peptides containing acetylated lysine, ...¹⁷⁰ By using specific protein extraction procedures it is also possible to isolate protein fractions from specific subcellular regions. By doing so changes in protein localization can be observed. This approach is referred to as “spatial proteomics”.^{171,172}

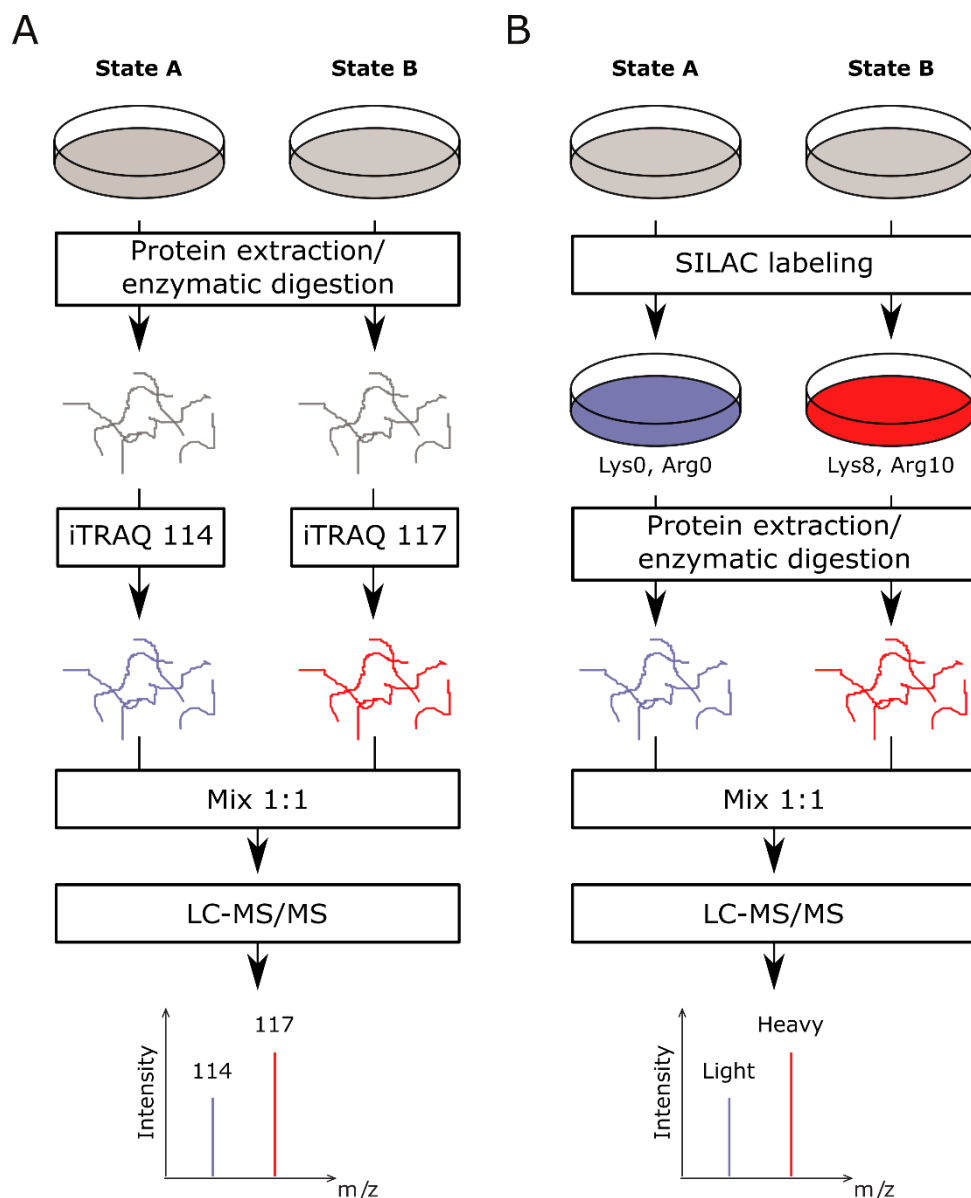


Figure 1-5. Schematic overview of chemical isobaric tags for relative and absolute quantification (iTRAQ) (A) and metabolic stable isotope labeling by amino acids in cell culture (SILAC) labeling (B). In the iTRAQ protocol proteins are extracted, enzymatically digested and peptides are labeled with isobaric tags prior to mixing. Peptides are separated with liquid chromatography (LC) and identified with MS/MS. The isobaric tags cause a mass shift which allows to quantification. SILAC labeling takes place before protein extraction, through metabolic incorporation of amino acids (arginine and lysine) containing stable isotopes.

1.2.3. High-throughput microscopy

Fluorescence microscopy is indispensable for cell biology. Fluorescent microscopes are configured to pass excitation light through the objective lens into the sample and then selectively observe the emitted fluorescent light coming back through the objective lens from the sample.¹⁷³ The most popular mode of fluorescence microscopy is widefield microscopy, using an inverted epifluorescence microscope, in which the objective images the sample from below. The choice of the objective dictates most of

the key properties of the microscope, and its performance is largely determined by the magnification and numerical aperture (NA). Objective magnification ensures that the image is magnified sufficiently on the camera. At least two camera pixels per resolvable element are required to capture the full resolution of the microscope objective (Nyquist rate). The NA of the objective correlates with the light-gathering power and inversely with the resolution limit (D) of the objective ($NA = \frac{0.61\lambda}{D}$).¹⁷⁴ A huge drawback of widefield microscopy is the fact that the entire specimen is bathed in light.¹⁷⁵ Both out-of-focus light and light emitted by the focal plane of the sample are detected by the camera. This out-of-focus light makes it impossible to achieve well-resolved 3D images. Confocal fluorescence microscopy can resolve this issue. This mode uses a focused laser beam to obtain a point-like illumination, and emitted light from this point is detected after passage through a pinhole. Hence, light from out-of-focus planes is blocked by the pinhole, resulting in a point-like detection.^{174,175} The use of point-like illumination necessitates raster scanning to generate a microscopic image. To this end, scanning mirrors are used to scan across the sample and build up the image point by point.¹⁷⁴ A disadvantage of point scanning is that it is slow. One solution, termed spinning disk confocal microscopy, is based spreading the laser beam over a rotating disk comprising a series of pinholes, through which many spots of the sample are illuminated simultaneously. The emitted fluorescence light is focused onto another or the same pinhole of the spinning disk. Simultaneous imaging and the rapid disk rotation allows much higher frame rates compared to CLSM.¹⁷⁶ On the other hand most of the light is blocked, resulting in an ineffective illumination of the sample, although this can be surpassed by adding a second disk of microlenses, referred to as the Yokogawa modification.^{176,177} The principle of widefield fluorescence microscopy and CLSM is shown in Figure 1-6.

To study cellular processes, the dynamic behaviour and microscopic scale need to be taken into account. By fixing cells a snapshot can be taken of the cellular processes at that specific moment. However, fixation protocols can damage and alter the cellular environment, complicating the interpretation of these images. Therefore, live cell imaging is more reliable to study the dynamic behaviour of cells. In the latter case automating image acquisition is indispensable. However, automation is also relevant for fixed cell imaging, since this enables the generation of large image data sets, which is termed high-throughput microscopy (HTM) (Figure 1-6).^{178,179} Furthermore, multiple features can be extracted from one microscopic field, such as multiple wavelengths, multiple focal planes, and morphological parameters. Automated analysis and exhaustive feature extraction is described as high-content analysis.¹⁸⁰ Combining HTM and high-content analysis is often referred to as “deep imaging”.¹⁸¹

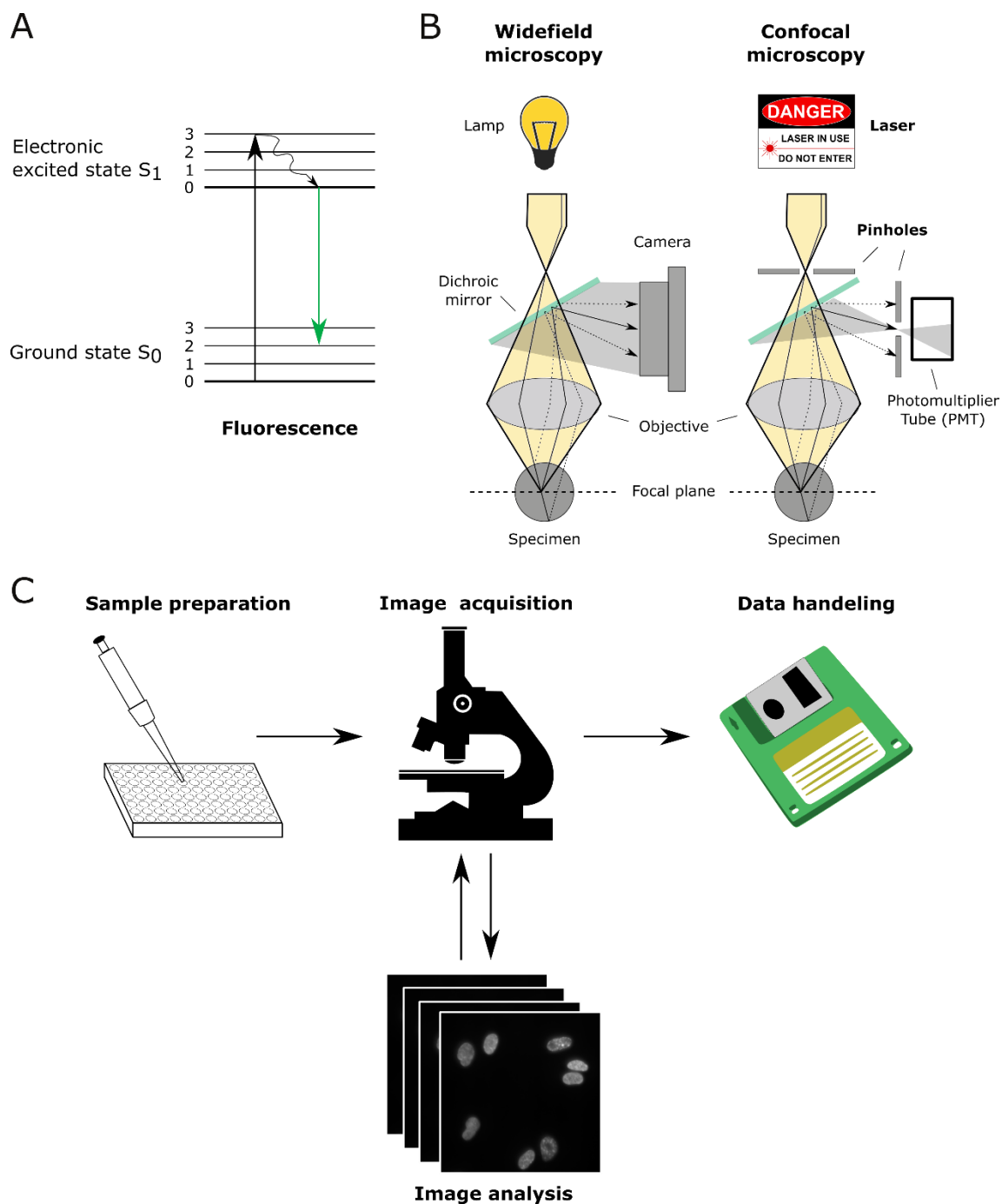


Figure 1-6. A: Energy diagrams of fluorescence. B: The light path and key components of a widefield microscopy (left) and a confocal microscopy. C: Scheme illustrating the workflow of high-throughput microscopy.

1.2.4. Raman microspectroscopy

Although fluorescence microscopy is a very important technique in life sciences, the technique has several limitations. First of all, in most cases fluorescent labels (fluorescent dyes or fluorescent fusion proteins) are required, which is invasive and can be harmful or even lethal (in case of fixation) for the examined cells.¹⁸² Secondly, only a limited number of fluorescent labels can be combined, and the narrow absorption spectra make it hardly possible to efficiently excite several dyes at once,

except for quantum dots (QDs).¹⁸³ One way to bypass these limitations is by making use of Raman microspectroscopy (RMS). This is a microscopic variant of Raman spectroscopy, and probes molecular vibrations in a biological sample per pixel, through the measurement of Raman scattering.¹⁸⁴ Raman scattering was discovered in 1928 by C.V. Raman and K.S. Krishnan, and is observed when a sample is irradiated with visible or near-infrared light.¹⁸⁵ Most of the incident photons undergo elastic scattering (Rayleigh scattering), while a small fraction are inelastically scattered by the interaction with molecular bonds. During interaction energy is exchanged with the vibrational energy levels of the molecules in the sample. This process can result in a loss in energy of the scattered photon, termed Stokes-shifted Raman scattering. Exceptionally, the interaction can result in a gain in energy of the scattered photon causing anti-Stokes-shifted Raman scattering, but due to the extreme rareness of this event, this type of scattering is hard to detect.¹⁸⁴ The energy diagrams of the various kinds of scattering are shown in Figure 1-7A. Conventional RMS measured spontaneous Stokes-shifted Raman scattering with a CLSM-based setup. Hence, Raman spectra are recorded via raster scanning a sample with a laser, Raman scatter is separated from Rayleigh scatter via an edge/notch filter, and the Raman spectra are resolved by dispersing the Raman scatter by a monochromator and finally detected by a CCD camera.¹⁸⁶ Raman spectra are multivariate datasets which require extensive processing prior to data analysis. Reconstruction of microscopic images can be obtained via complex spectral unmixing and clustering algorithms.¹⁸⁷ The setup of a Raman microscope is shown in Figure 1-7B. Its typical output is shown in Figure 1-7C, relevant Raman bands corresponding with DNA/RNA, lipids and proteins are indicated with arrows.

Due to the weak nature of Raman signals, RMS requires long acquisition times. Reducing acquisition time can result in insufficient signal-to-noise ratios, or spatial under-sampling.¹⁸⁸ Another way to cope with the weak Raman signals is by boosting them through the use of nonlinear RMS, for example, coherent anti-Stokes-shifted Raman scattering (CARS) microscopy and stimulated Raman (SRS) microscopy. In the latter techniques two laser pulses with different angular frequencies are used, and when the difference between the angular frequencies of the two incident lasers coincides with that of the vibrational mode of the sample molecule, intense and unidirectional radiation is emitted due to a nonlinear Raman process.¹⁸⁶

In summary, RMS can be used to capture molecular changes in cells, tissues or biofluids, without the need of labeling. Therefore, RMS can complement fluorescence microscopy. Furthermore the technique can be used for medical diagnostics, and Raman spectra can be collected *in vivo* through the use of a Raman needle probe.¹⁸⁸ Previous studies have shown that RMS can be used to study a wide variety of diseases, but most studies focus on cancer, including brain cancer, breast cancer, lung cancer, skin cancer, colorectal cancer, and prostate cancer.^{188–191} For example, Raman spectra of high-grade gliomas presented a higher contribution from nucleic acids compared to those of normal tissue, or the ratio of the Raman band intensity of lung cancer tissue was different from normal tissue at 1445 cm^{-1} and 1655 cm^{-1} .¹⁸⁸ RMS can be exploited as a diagnostic tool by developing supervised classification

models. To this end several techniques can be used such as support vector machines (SVM), linear discriminant analysis (LDA), and partial least squares discriminant analysis (PLS-DA). The robustness and performance of classification models largely depends on the sample size. It has been shown that 75 to 100 samples are needed to train a good, however not perfect classifier.¹⁹² The large sample size complicates the use of the time-consuming unstimulated RMS as a diagnostic tool favoring the use of stimulated RMS.

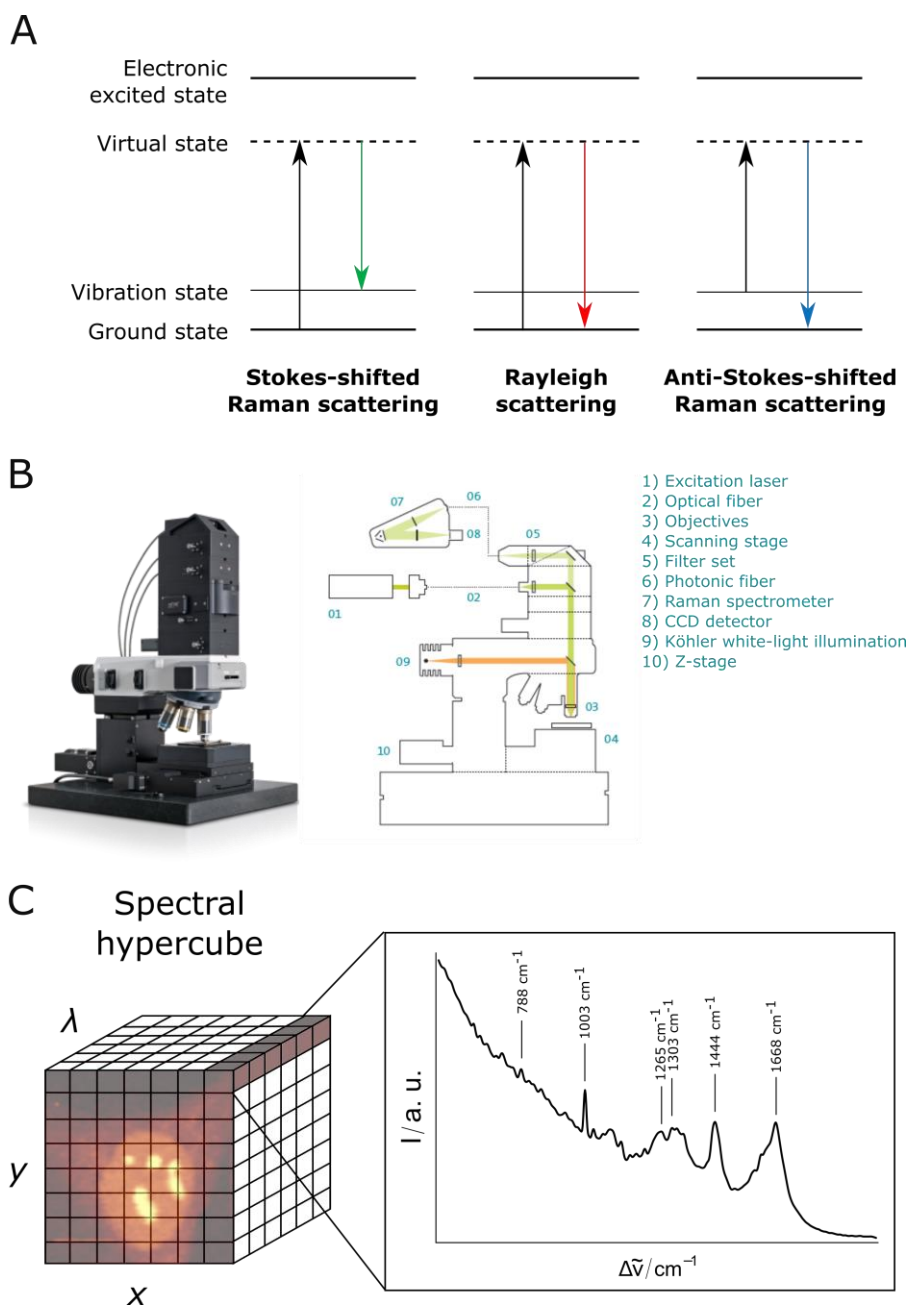


Figure 1-7: A: Energy diagrams of Stokes-shifted Raman scattering, Rayleigh scattering, and anti-Stokes shifted Raman scattering. B: Scheme of a Raman microscope (Alpha R300, WITec). C: Illustration of the hyperspectral Raman image acquired by Raman microspectroscopy together with a typical Raman spectrum, arrows highlight relevant Raman bands such as the O-P-O stretching vibration at 788 cm^{-1} ,

corresponding with the DNA/RNA backbone¹⁹³; the symmetric ring breathing in phenylalanine at 1000 cm⁻¹, corresponding with protein content¹⁹³; the amide III in-plane deformations and in-plane C-H bending modes at 1263 cm⁻¹, corresponding with proteins and unsaturated lipids, respectively^{184,194}; the twisting and wagging modes of CH₂ groups at 1303 cm⁻¹, corresponding with lipids and proteins¹⁸⁴; the bending and scissoring modes of CH₂ groups at 1444 cm⁻¹, corresponding with lipids and proteins¹⁸⁴; and the C=C stretching modes and amide I C=O stretching modes at 1668 cm⁻¹, corresponding with unsaturated lipids and proteins.¹⁸⁴

1.3. Scope

A-type lamins have a wide variety of functions in the nucleus, ranging from structural support to sequestration of transcription factors and chromatin organization. The wide spectrum of diseases caused by mutations in the *LMNA* gene is illustrative of this diversity of functions. Although a large number of disease-causing mutations have been identified, the underlying pathogenic mechanisms are still not well understood. This lack of knowledge complicates the development of novel therapeutic strategies. The goal of this work is to unveil pathways that are regulated by A-type lamins using modern cytomics. Previous studies mainly used patient cells, which are scarce and have heterogeneous genetic backgrounds, or cells retrieved from animal models. Therefore we developed isogenic human cellular models, through the use of siRNA-mediated knockdown or CRISPR/Cas9-mediated genome editing.^{195–197}

Lamins have been documented as mediators of oxidative stress, and laminopathy patient cells show increased levels of reactive oxygen species (ROS). A number of theories have been proposed, although several questions remain unanswered, such as the involvement of mitochondria in this phenomenon.⁵² Therefore we analyzed the influence of *LMNA* and *ZMPSTE24* knockdown in human dermal fibroblasts, on the generation of cellular ROS and the mitochondrial membrane potential (chapter 2). We used a quantitative microscopy-based analysis to measure ROS levels and mitochondrial membrane potential in real time. This allowed us to study the involvement of mitochondria in the onset of oxidative stress, triggered by *LMNA* and *ZMPSTE24* knockdown.

Laminopathies have been primarily studied with genomic and transcriptomic techniques, such as sequencing and microarrays. However, gene expression data cannot be directly extrapolated to protein level changes, due to the influence of post-translational modifications and protein turnover. Therefore, we used a SILAC-based quantitative proteomics approach to identify the impact of *LMNA* knockdown on global protein expression (chapter 3). Gene ontology (GO) analysis was used to identify disrupted pathways in *LMNA* knockdown fibroblasts.

Genomics, transcriptomics and proteomics can highlight changes in DNA, RNA expression and protein production, respectively. However, these techniques are not able to point out general molecular changes in a biological sample (e.g. lipids, carbohydrates, ...). This can be addressed by RMS. We used this technique to generate a molecular fingerprint of HeLa cells in which *ZMPSTE24* was knocked out,

using CRIPR/Cas9-mediated genome engineering (chapter 4). This allowed us to identify high-level molecular changes triggered by prelamin A accumulation in HeLa cells.

2

SUSTAINED ACCUMULATION OF PRELAMIN A AND DEPLETION OF LAMIN A/C BOTH CAUSE OXIDATIVE STRESS AND MITOCHONDRIAL DYSFUNCTION BUT INDUCE DIFFERENT CELL FATES

This work is published in: Sieprath T*, Corne TD*, Nootboom M, Grootaert C, Rajkovic A, Buyschaert B, Robijns J, Broers JL, Ramaekers FC, Koopman WJ, et al. Sustained accumulation of prelamin a and depletion of lamin A/C both cause oxidative stress and mitochondrial dysfunction but induce different cell fates. *Nucleus* 2015; :1–11.

* Shared first authorship

Abstract

The cell nucleus is structurally and functionally organized by lamins, intermediate filament proteins that form the nuclear lamina. Point mutations in genes that encode a specific subset of lamins, the A-type lamins, cause a spectrum of diseases termed laminopathies. Recent evidence points to a role for A-type lamins in intracellular redox homeostasis. To determine whether lamin A/C depletion and prelamin A accumulation differentially induce oxidative stress, we have performed a quantitative microscopy-based analysis of reactive oxygen species (ROS) levels and mitochondrial membrane potential ($\Delta\Psi_m$) in human fibroblasts subjected to sustained siRNA-mediated knockdown of *LMNA* and *ZMPSTE24*, respectively. We measured a highly significant increase in basal ROS levels and an even more prominent rise of induced ROS levels in lamin A/C depleted cells, eventually resulting in $\Delta\Psi_m$ hyperpolarization and apoptosis. Depletion of *ZMPSTE24* on the other hand, triggered a senescence pathway that was associated with moderately increased ROS levels and a transient $\Delta\Psi_m$ depolarization. Both knockdowns were accompanied by an upregulation of several ROS detoxifying enzymes. Taken together, our data suggest that both persistent prelamin A accumulation and lamin A/C depletion elevate ROS levels, but to a different extent and with different effects on cell fate. This may contribute to the variety of disease phenotypes witnessed in laminopathies.

2.1. Introduction

The nuclear lamina provides structural support to the nucleus and plays a central role in nuclear organization and gene regulation.¹⁴ Point mutations in the *LMNA* gene, which encodes its major constituent proteins, lamin A and C, cause a broad range of diseases termed laminopathies.¹⁴ During maturation, lamin A (LA) is extensively processed, with consecutive steps of farnesylation, proteolytic cleavage of the C-terminal three amino acids, carboxymethylation and removal of the C-terminal 15 amino acids, including the farnesyl group.³⁷ The final step is exclusively catalyzed by the zinc-metalloproteinase ZMPSTE24. Accumulation of different prelamin A (PLA) intermediates is correlated with disease but especially the farnesylated variants are presumed to be cytotoxic.¹⁹⁸ The Hutchinson-Gilford progeria syndrome (HGPS) for example is caused by an accumulation of the mutant farnesylated PLA intermediate progerin.¹⁹⁹ Likewise, in restrictive dermopathy (RD), loss of functional ZMPSTE24 results in the accumulation of farnesylated PLA.^{127,200} The underlying disease causing mechanisms are still largely unknown but it is becoming increasingly more clear that next to its structural function and role in nuclear dynamics⁵⁴, the nuclear lamina also modulates intracellular redox homeostasis.⁵² Various studies revealed that reactive oxygen species (ROS) levels are increased in laminopathy patient cells and during PLA accumulation.^{201–204} For example, fibroblasts from various lipodystrophy patients as well as cells treated with protease inhibitors demonstrate increased ROS levels.²⁰⁴ Proteomic and metabolic profiling suggest that this increase can be attributed to dysfunctional mitochondria.^{128,205}

To corroborate these findings, we developed a microscopy-based strategy for combined measurement of ROS and mitochondrial membrane potential ($\Delta\Psi_m$) in cellular models of PLA accumulation or LA deficiency. Using this approach, we found that both accumulation of PLA and reduction of mature LA increased intracellular ROS levels, albeit not at the same rate nor to the same extent, and also caused changes in $\Delta\Psi_m$. These effects were accompanied by reduced mitochondrial respiration and altered gene expression of ROS detoxifying enzymes.

2.2. Results

Sustained knockdown of ZMPSTE24 and LMNA reduce cell proliferation via different mechanisms

Accumulation of PLA or reduction of mature LA was achieved in human fibroblasts by respectively silencing the expression of *ZMPSTE24* or *LMNA* with specific siRNAs. A pool of non-targeting (NTkd) siRNAs was used as control. To maintain the knockdowns for prolonged periods of time, repetitive rounds of siRNA transfection were performed, separated by 72 h to 96 h. 48 h after the first transfection there was a highly significant downregulation of both genes at the RNA-level: ~4-fold (~75%) for *ZMPSTE24* knockdown (ZMPSTE24kd) and ~17-fold (~94%) for *LMNA* knockdown (LMNAkd). Similar levels were found after 168 h (two rounds of transfection) (Figure 2-1A). At the protein level, however, the effect became more pronounced with time. Quantitative immunofluorescence revealed an ~1.8-fold increase in PLA levels 48 h after the initial transfection, and a ~4-fold increase after 264 h (3 consecutive transfections) (Figure 2-1B). Similarly, the abundance of mature LA dropped 1.3-fold after 48 h and decreased more than 4-fold after 264 h (Figure 2-1C). The effects were qualitatively confirmed by Western blot (Figure 2-1D). Immunostaining also revealed that knockdowns were accompanied by progressive changes in nuclear morphology. Whereas LMNAkd led to nuclear elongation and erosion of peripheral chromatin, sustained ZMPSTE24kd led to a dramatic increase in nuclei with folds and blebs (Figure 2-1E & F).

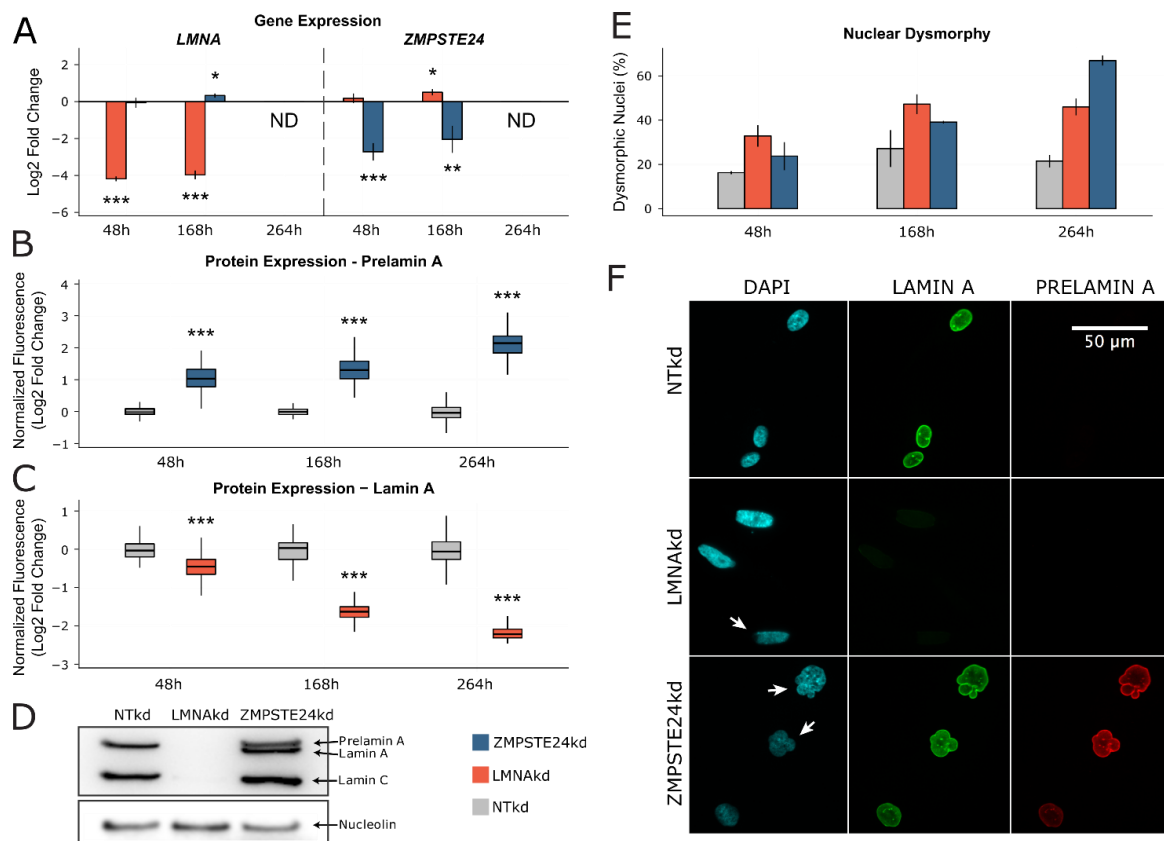


Figure 2-1. Sustained siRNA-mediated knockdown of *LMNA* (LMNAkd) and *ZMPSTE24* (ZMPSTE24kd). A: Gene expression levels of *LMNA* and *ZMPSTE24* measured by real-time qPCR relative to non-targeting control (NTkd). B and C: PLA and LA protein levels in ZMPSTE24kd resp. LMNAkd cells versus NTkd control, as measured by immunofluorescence staining and quantitative image analysis. D: Western blot with an A-type lamin antibody that recognizes lamin A, lamin C and PLA, showing absence of lamin A/C in LMNAkd and accumulation of PLA in ZMPSTEkd cells at the 168h time point. Nucleolin was used as a loading control. E: Quantification of the number of dysmorphic nuclei, expressed relative to the total number of cells. F: Representative images of LMNAkd, ZMPSTEkd and NTkd control cells at the 168h time point, after immunofluorescence staining for LA (green), PLA (red) and counterstaining with DAPI (cyan). Arrows indicate nuclear aberrations. The experiments were performed in triplicate and a minimum of 100 cells were imaged per replicate. In the boxplots, the horizontal line indicates the median, boxes the 25th and 75th percentile, and whiskers the 5th and 95th percentile. Error bars indicate the standard deviation on the mean value. (* = p-value < 0.05; ** = p-value < 0.01; *** = p-value < 0.001)

Both knockdowns had an adverse impact on cell proliferation, resulting in significantly increased population doubling times (decreased population doubling level, PDL) with respect to the NTkd control (Figure 2-2A). The effect of LMNAkd was markedly stronger than that of ZMPSTE24kd. Quantification of β -galactosidase positive cells and p21-positive cells – two markers for senescence²⁰⁶ – revealed that only ZMPSTE24kd triggered cellular senescence (Figure 2-2B,C,E). LMNAkd predominantly triggered cell death, as evidenced by a marked increase in the number of fragmented nuclei (Figure 2-2D & E).

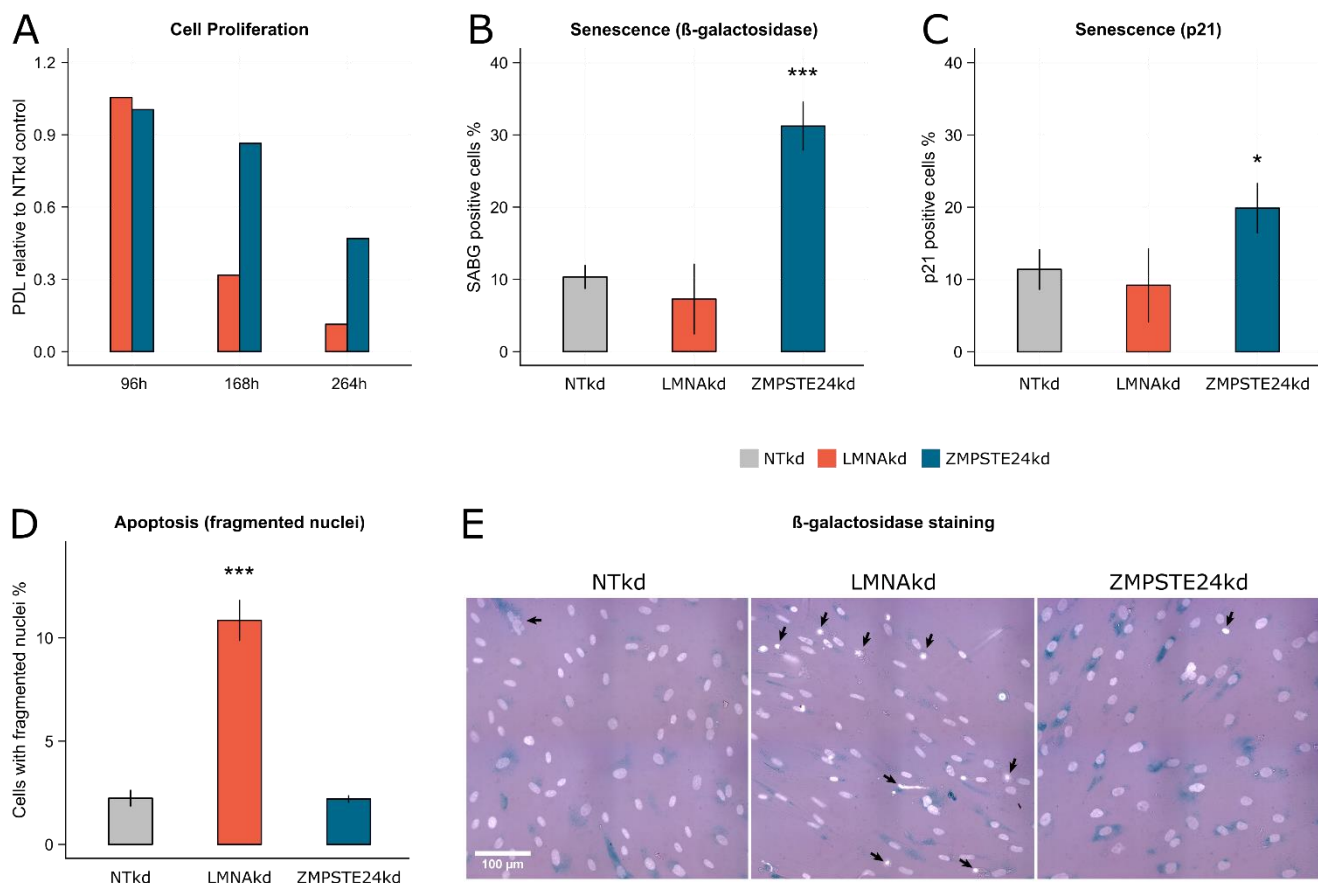


Figure 2-2. Sustained siRNA-mediated knockdown of *LMNA* and *ZMPSTE24* affects cell proliferation. A: The relative population doubling speed compared to the NT-control expressed as population doubling level (PDL) at different time points. B: Quantification of the number of β -galactosidase positive cells at 168 h, relative to the total number of cells. C: Quantification of the number of p21 positive cells at 168 h, relative to the total number of cells. D: Quantification of apoptosis, expressed by the number of fragmented nuclei relative to the total number of cells. E: Representative images of β -galactosidase stained NT control, LMNAkd and ZMPSTE24kd cells (senescent cells in blue), merged with DAPI channel (grey/white). Arrows indicate nuclear aberrations. Except for the PDL measurements, the experiments were performed in triplicate. Error bars indicate the standard deviation on the mean value. (* = p-value < 0.05; ** = p-value < 0.01; *** = p-value < 0.001)

***LMNAkd* significantly raises basal and induced ROS levels; *ZMPSTE24kd* only causes a modest increase of the basal ROS level**

We established and validated a high-content workflow to simultaneously measure intracellular ROS levels and $\Delta\psi_m$, using the fluorescent reporter molecules CM-H₂DCFDA and TMRM, respectively (see M&M and Figure 2-9 for details). Using this method, we quantified ROS levels in human fibroblasts subjected to sustained knockdown of *ZMPSTE24* or *LMNA* under basal conditions and after acute application of 20 μ M of the oxidant tert-butyl hydrogen peroxide (TBHP). The latter served as proxy for induced ROS and was expressed as the relative increase with respect to the basal ROS levels.

LMNAkd caused a time-dependent increase in both basal and induced ROS levels. Whereas the increase in basal ROS levels only became significant after 168 h, the induced ROS levels were already significantly higher at 96 h. ZMPSTE24kd on the other hand, only resulted in a modest, but significant increase in basal ROS levels after 264 h. Within the experimental time frame, this treatment did not cause a significant increase of induced ROS (Figure 2-3A & B).

Next to the knockdowns, passage-matched fibroblasts from specific laminopathy patients ($LMNA^{Y259X/Y259X}$, $LMNA^{G608G/+}$, $LMNA^{+/+}$) were subjected to the same analysis. $LMNA^{Y259X/Y259X}$ cells are incapable of producing mature lamin A/C²⁰⁷ and $LMNA^{G608G/+}$ cells accumulate a truncated, farnesylated prelamin A variant termed progerin.²⁰⁸ In line with the results from the sustained knockdown, $LMNA^{Y259X/Y259X}$ demonstrated an increase in both basal and induced ROS, whilst $LMNA^{G608G/+}$ cells only showed an increase in basal ROS (Figure 2-3C & D).

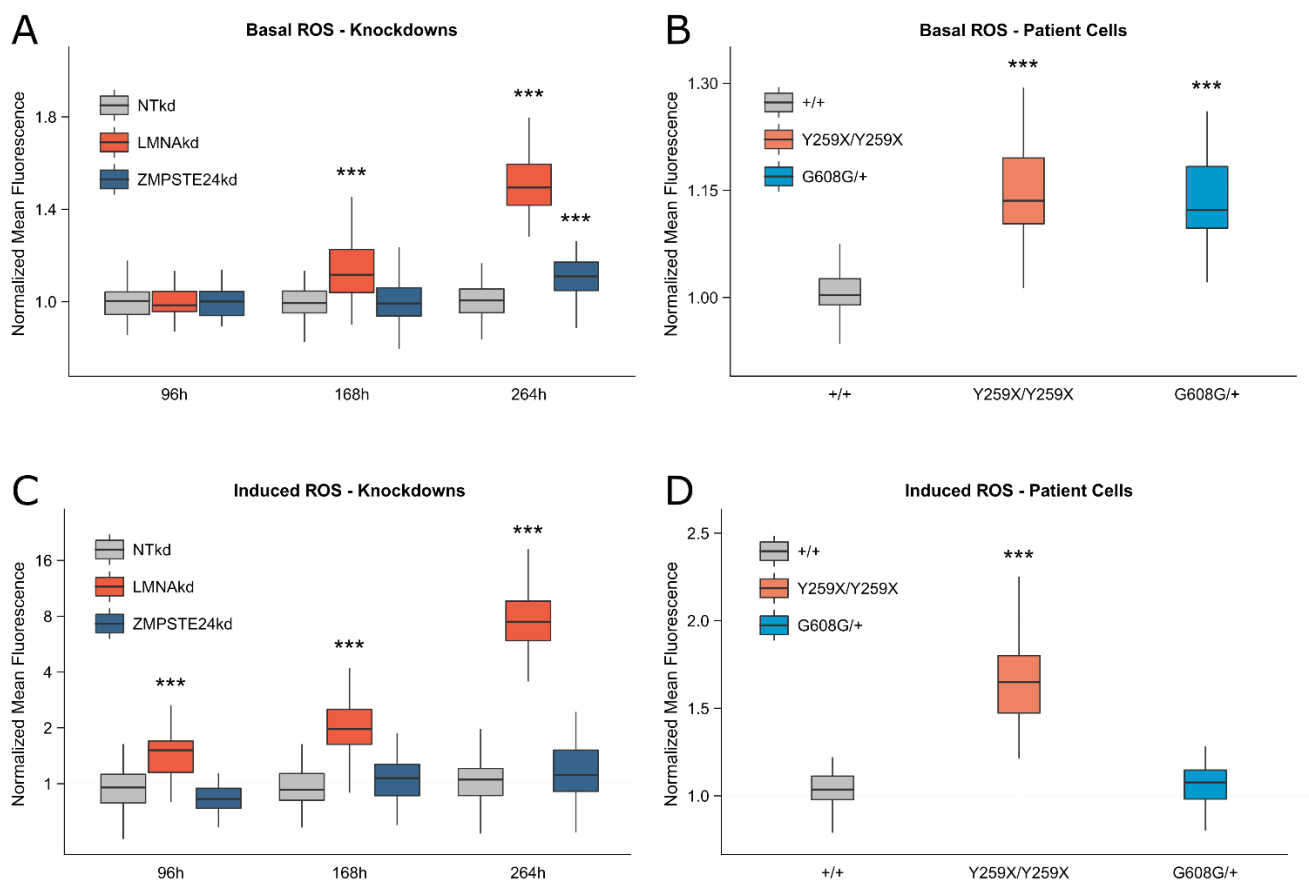


Figure 2-3. Both, LMNAkd and ZMPSTE24kd cells have increased basal ROS levels. LMNAkd are more susceptible towards induced ROS. A and B: Normalized basal levels of intracellular ROS measured by CM-H₂DCFDA high content microscopy analysis and response towards induced ROS, measured as relative gain in intensity after 20µM TBHP addition at different time points in LMNAkd and ZMPSTE24kd cells. C and D: Normalized basal levels of intracellular ROS and response towards induced ROS in $LMNA^{Y259X/Y259X}$ and $LMNA^{G608G/+}$ cells. The experiments were performed in triplicate and a minimum of 100 cells were imaged per replicate. In the boxplots, the horizontal line indicates the median, boxes the 25th and 75th percentile, and whiskers the 5th and

95th percentile. (* = p-value < 0.05; ** = p-value < 0.01; *** = p-value < 0.001; the range of the y-axes has been adjusted to optimally display the differences)

ZMPSTE24kd and LMNAkd affect $\Delta\psi_m$ in a time dependent manner

As dysfunctional mitochondria can generate increased amounts of ROS, we estimated $\Delta\psi_m$ as a functional readout, by quantifying the mitochondrial accumulation of the reporter dye TMRM using the high content microscopy method described above. Dynamic and time-dependent changes were observed for the different treatments. LMNAkd induced $\Delta\psi_m$ depolarization at 96 h and 168 h and $\Delta\psi_m$ hyperpolarization at 264 h. On the other hand, ZMPSTE24kd resulted in a transient $\Delta\psi_m$ depolarization at 168 h (Figure 2-4A). In the case of patient cells, *LMNA*^{Y259X/Y259X} fibroblasts displayed slight $\Delta\psi_m$ hyperpolarization that was not significantly different from *LMNA*^{+/+} control cells. In contrast, *LMNA*^{G608G/+} fibroblasts displayed significant $\Delta\psi_m$ depolarization (Figure 2-4B).

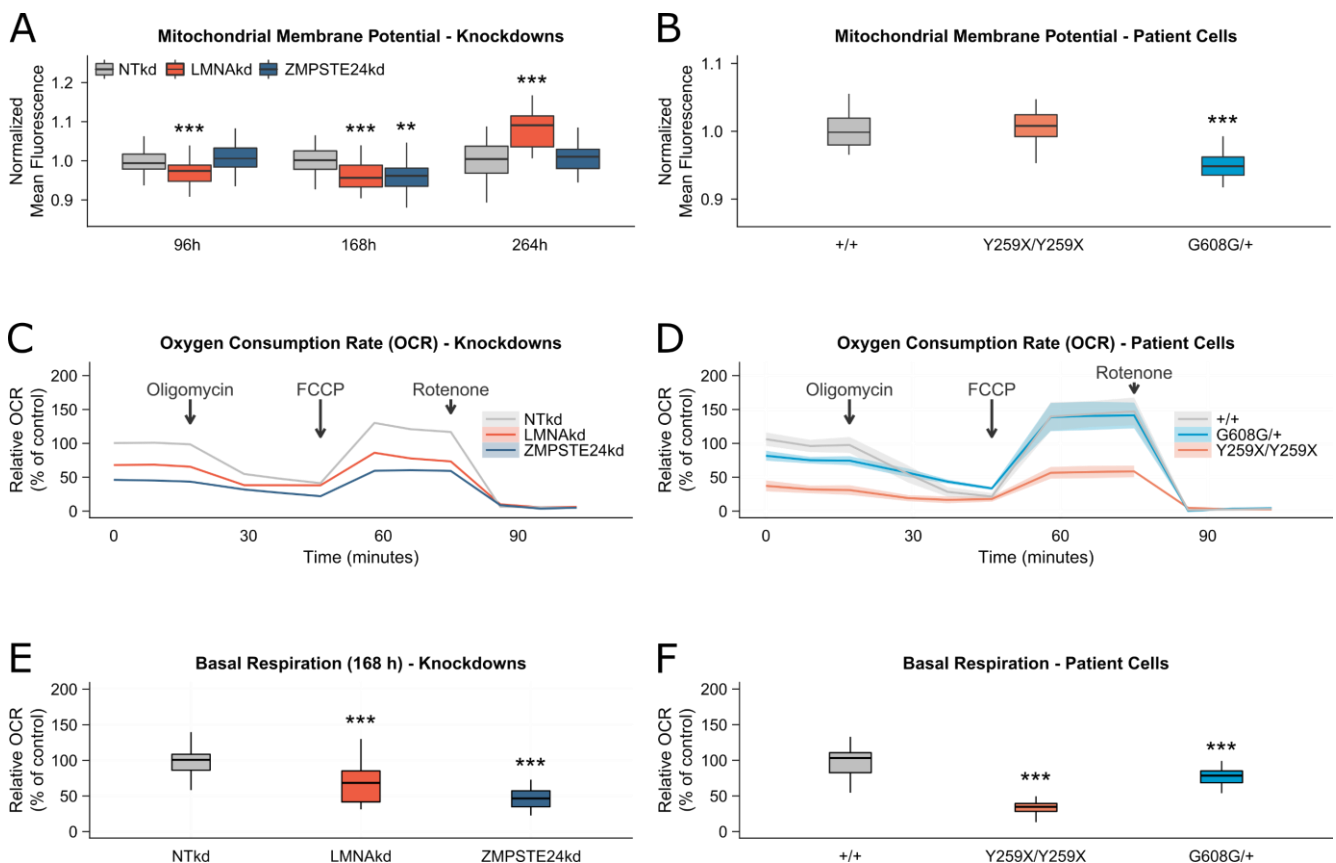


Figure 2-4. Sustained siRNA-mediated knockdown of LMNA and ZMPSTE24 induces time-dependent alterations in mitochondrial membrane potential ($\Delta\psi_m$) and decreased basal mitochondrial respiration. A: Normalized $\Delta\psi_m$ as measured by TMRM at different time points in LMNAkd and ZMPSTE24kd cells. B: Normalized $\Delta\psi_m$ in LMNA^{Y259X/Y259X} and LMNA^{G608G/+} cells. The $\Delta\psi_m$ experiments were performed in triplicate and a minimum of 100 cells were imaged per replicate. In the boxplots, the horizontal line indicates the median, boxes the 25th and 75th percentile, and whiskers the 5th and 95th percentile. C and D: Normalized basal respiration of LMNAkd, ZMPSTE24kd, LMNA^{Y259X/Y259X} and LMNA^{G608G/+} cells. E and F: Normalized respiration profiles of LMNAkd, ZMPSTE24kd, LMNA^{Y259X/Y259X} and LMNA^{G608G/+}

cells. The experiments were performed in triplicate and the shaded region represents the standard error on the measurements. See the materials and methods section for more information about the different chemical components that were added. (* = p-value < 0.05; ** = p-value < 0.01; *** = p-value < 0.001; the range of the y-axes has been adjusted to optimally display the differences)

ZMPSTE24kd and LMNAkd decrease basal oxygen consumption rates

Since the TMRM measurements suggested a (transient) defect in mitochondrial function, we next investigated mitochondrial oxygen consumption (Figure 2-4C-F). At the 168 h time point, we found strong deviations between the respiration curves (Figure 2-4C & D).

Especially, the basal oxygen consumption rate (OCR) was significantly lower in both ZMPSTE24kd and LMNAkd cells (Figure 2-4E). This was also the case for *LMNA*^{Y259X/Y259X} and *LMNA*^{G608G/+} patient fibroblasts (Figure 2-4F).

LMNAkd nor ZMPSTE24kd are correlated with significant changes in mitochondrial superoxide

To verify whether a change in $\Delta\psi_m$ was accompanied by a change in mitochondrial superoxide ($\bullet O_2^-$) production, we measured the latter using the mitochondria-targeted $\bullet O_2^-$ sensor MitoSOX. After 168h hours, no significant change in $\bullet O_2^-$ levels was observed, despite a transient decrease in $\Delta\psi_m$ in both knockdowns. After 264h LMNAkd cells clearly displayed a significant increase in $\Delta\psi_m$ as well as in $\bullet O_2^-$ (Figure 2-5).

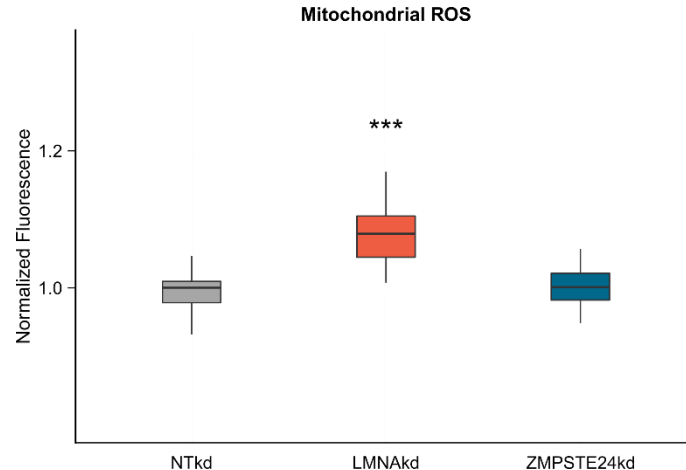


Figure 2-5. 264h of sustained siRNA-mediated knockdown of LMNA results in significantly increased mitochondrial ROS levels. A: Normalized basal levels of mitochondrial ROS measured by MitoSOX high content microscopy after 264h of knockdown. The experiments were performed in triplicate and a minimum of 100 cells were imaged per replicate. In the boxplots, the horizontal line indicates the median, boxes the 25th and 75th percentile, and whiskers the 5th and 95th percentile. Significance was calculated with the Wilcoxon rank sum test; *** = p-value < 0.001.

LMNAkd and ZMPSTE24kd differentially affect antioxidant gene expression

Oxidative stress arises from an imbalance between ROS production and removal. To find out whether the accumulation of ROS correlated with a change in expression of

ROS detoxifying enzymes, we performed a qPCR analysis. In general, LMNAkd more profoundly affected the expression of these enzymes than ZMPSTE24kd. In both conditions, most of the investigated genes became upregulated with the strongest effect being observed on the *GSTT2* transcript levels. Strikingly, ZMPSTE24kd and LMNAkd oppositely affected the expression of the mitochondrial manganese-(Mn)-superoxide dismutase (*SOD2*). This ROS-detoxifying enzyme converts superoxide ($O_2^{\cdot-}$) into hydrogen peroxide (H_2O_2). Expression of *SOD2* is regulated by the key cytokine *IL6*.²⁰⁹ Subsequent quantification of *IL6* transcript levels revealed a strong upregulation in ZMPSTE24kd and downregulation in LMNAkd cell cultures (Fig. 5). The same opposite expression pattern was also observed in *LMNA*^{Y259X/Y259X} and *LMNA*^{G608G/+} patient fibroblasts (Figure 2-6).

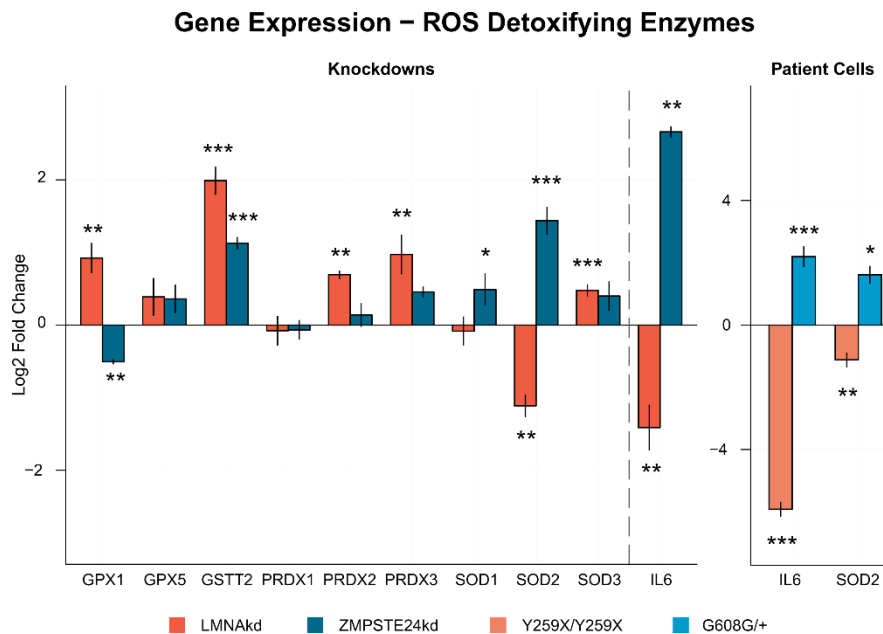


Figure 2-6. LMNAkd and ZMPSTE24kd cells show altered gene expression of ROS defusing enzymes. A: Gene expression levels of *GPX1*, *GPX5*, *GSTT2*, *PRDX1*, *PRDX2*, *PRDX3*, *SOD1*, *SOD2*, *SOD3* and *IL6* were measured in LMNAkd and ZMPSTEkd cells by real-time qPCR relative to NTkd control at 168 h. B: Gene expression levels of *IL6* and *SOD2* were measured in *LMNA*^{Y259X/Y259X} and *LMNA*^{G608G/+} fibroblasts by real-time qPCR relative to untreated passage matched control fibroblasts. The values in this plot represent the average of 3 technical replicates, but only one biological replicate because we only have one cell line for each mutation. Therefore, we cannot provide biologically relevant error bars. (* = p-value < 0.05; ** = p-value < 0.01; *** = p-value < 0.001)

Proteasome inhibition increases intracellular ROS and $\Delta\psi_m$

To check whether proteasome inhibition could induce ROS or alter $\Delta\psi_m$, human fibroblasts were treated with 10 μ M MG132 for 16h and analyzed using the microscopy based assay described earlier. Similar to the results obtained in LMNAkd cells, these

cells display increased basal and induced ROS levels, as well as an increased $\Delta\psi_m$ (Figure 2-7).

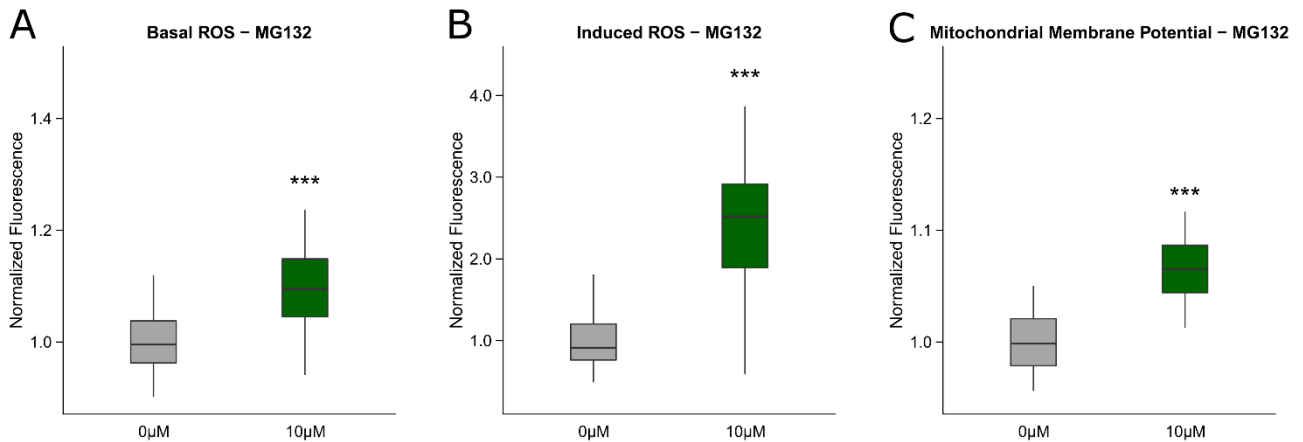


Figure 2-7. Treatment of human fibroblasts with 10µM of MG-132 for 16h results in increased basal ROS levels, increased induced ROS levels and an increased $\Delta\psi_m$ comparable to observations made on LMNAkd cells. Healthy human fibroblasts were treated with 10µM of MG-132, a known potent inhibitor of the proteasome, and analyzed with CM-H₂DCFDA- and TMRM-based high content microscopy to check whether proteasomal dysfunction could give rise to the same kind of observations made in the knockdown cells. Indeed, both a sustained knockdown of LMNA and a treatment with 10µM of MG-132 give rise to the same observations for basal and induced ROS (A & B), as well as for mitochondrial membrane potential (C). This adds to the hypothesis that proteasomal overload caused by LMNA knockdown might trigger generation of intracellular ROS in the mitochondria. The experiments were performed in triplicate and a minimum of 100 cells were imaged per replicate. In the boxplots, the horizontal line indicates the median, boxes the 25th and 75th percentile, and whiskers the 5th and 95th percentile. For all figures, significance was calculated with the Wilcoxon rank sum test; *** = p-value < 0.001.

2.3. Discussion

With this work, we set out to enhance our understanding of how PLA accumulation and LA deficiency affect cellular redox homeostasis and ROS levels at the cellular level. Since mature LA is firmly integrated within the nuclear lamina, it is characterized by low turnover rates.²¹⁰ This makes studying LA biology by acute siRNA-mediated knockdown strategies unreliable. We therefore induced sustained knockdown in human fibroblasts by repetitive siRNA transfection. After the initial transfection, gene expression levels dropped relatively quickly to a minimum (within 72 h), but the actual protein levels progressively changed over a time span of 264 h (LA declined, PLA increased). In LMNAkd cells, and especially in ZMPSTE24kd cells, this was accompanied by overt changes in nuclear morphology in a large fraction (60-70%) of cells. Similar levels of nuclear dysmorphism were quantified in human mesenchymal stem cells (hMSCs) after siRNA-mediated knockdown of *ZMPSTE24*¹³⁷ and the observed morphological changes were similar to those seen in *Zmpste24*^{-/-} mouse embryonic fibroblasts (MEF)²¹¹ and HGPS patient fibroblasts.²¹² As a rough validation, we extended our experiments with measurements of cells from *LMNA*^{Y259X/Y259X} and

LMNA^{G608G/+} patients, although it should be noted that the patient's genetic background might play a role in the outcome of the experiments. In addition, knockdown of *ZMPSTE24* causes accumulation of a farnesylated full-length PLA, whereas HGPS cells (*LMNA*^{G608G/+}) produce a different farnesylated PLA variant lacking 50 amino acids.

To measure ROS levels and mitochondrial function in a robust and reliable manner at the single cell level, we established and benchmarked a high-content microscopy workflow in which we measured both intracellular ROS levels and mitochondrial membrane potential ($\Delta\Psi_m$). Using this approach, we observed that both accumulation of farnesylated PLA and reduction of mature LA increased intracellular ROS levels, albeit at different rates. Compared to *ZMPSTE24kd*, *LMNAkd* induced a progressive increase in basal ROS that was much more pronounced and started much earlier in the experimental time frame. And whereas *ZMPSTE24kd* cells showed no significant alteration in their response to the exogenous oxidant TBHP, *LMNAkd* cells proved to be hypersensitive. These observations correlate well with those obtained by Pekovic et al.²¹³ and support the hypothesis that the nuclear lamina acts as an intracellular ROS-sink via conserved redox-reactive cysteine residues within the lamin tail.²¹³ When A-type lamins (and their cysteine residues) are depleted, the ability of the lamina to act as a ROS buffering system is abrogated, rendering the cell more sensitive against (potentially dangerous) increases of the intracellular ROS levels. PLA accumulation however does not decrease the concentration of these cysteine residues, leaving the ROS-sink intact. If PLA concentrations rise above a certain threshold though, as observed in *ZMPSTE24kd* cells at 264h, ROS levels do increase. This was also recently reported by a study in fibroblasts of centenarians.²¹⁴

To determine whether elevated ROS levels correlated with mitochondrial dysfunction, we also quantified $\Delta\Psi_m$. Our results revealed that *LMNAkd* induces $\Delta\Psi_m$ depolarization at early time points, followed by $\Delta\Psi_m$ hyperpolarization at 264 h. In contrast, *ZMPSTE24kd* induced a transient $\Delta\Psi_m$ depolarization. In accordance with the increase in $\Delta\Psi_m$, we also observed a significant increase in mitochondrial $\bullet\text{O}_2^-$ levels in *LMNAkd* cells after 264h, as reported by the MitoSOX sensor dye. Indeed, it has been demonstrated before that mitochondria produce more ROS at high membrane potential.^{215,216}

Since mitochondria are the initial sites of oxidative damage and the instigators of oxidative stress in the cytosol upon proteasome dysfunction²¹⁷, a possible connection with the knockdowns may lie in their potential to cause proteasome inhibition. Depletion of LA has been linked to accumulation of nuclear envelope proteins (SUN2, Emerin and Nesprin-1) in the endoplasmic reticulum and upregulation of various ubiquitin ligases, resulting in proteasome overload.^{114,218–220} Supporting this hypothesis, treatment of fibroblasts for 16h with 10 μM of MG-132, a potent proteasome inhibitor, also resulted in a significant increase of basal and induced ROS levels, as well as increased $\Delta\Psi_m$, as observed in *LMNAkd* cells at 264h.

In accordance with a defect in mitochondrial function, and consistent with observations in *Zmpste24*^{-/-} mouse adult fibroblasts²⁰⁵, the basal mitochondrial respiration rate in both LMNAkd and ZMPSTE24kd cells as well as in *LMNA*^{Y259X/Y259X} and *LMNA*^{G608G/+} patient cells was lowered.

Parallel to the increase in intracellular ROS, both knockdowns showed increased expression of ROS detoxifying enzymes. The greater induction of basal ROS in LMNAkd with respect to ZMPSTE24kd cells correlated with a larger number of upregulated genes. In both conditions, the general trend was preserved except a differential expression of *GPX1* and *SOD2*. *SOD2* is a mitochondrial superoxide converting enzyme, the expression of which is regulated by *IL6*, a senescence associated cytokine.^{221–223} We found that both *IL6* and *SOD2* were upregulated in ZMPSTE24kd and downregulated in LMNAkd cells. The same opposite expression was observed in *LMNA*^{G608G/+} and *LMNA*^{Y259X/Y259X} fibroblasts, respectively, even with a much stronger (~78 fold) downregulation of *IL6* in *LMNA*^{Y259X/Y259X} cells. The upregulation of *SOD2* in ZMPSTE24kd cells might explain why these cells display no significant increase in mitochondrial superoxide.²¹⁷ When following this reasoning, downregulation of *SOD2* should then trigger a rise in mitochondrial ROS levels, which we indeed observed in LMNAkd cells after 264h. Previously, we have shown that repetitive ruptures of the nuclear envelope in lamin A/C deficient cells temporarily relocate various transcription factors, several of which controlling oxidative stress response.⁶² In addition, we found that lamin A/C deficiency caused cytoplasmic translocation of nuclear PML bodies⁶⁰, known sensors of oxidative stress and regulators of redox homeostasis.^{224,225} It is conceivable that these phenomena contribute to the oxidative stress phenotype witnessed in LMNAkd cells as well.

Irrespective of the ROS source, we witnessed a decreased cell proliferation in both ZMPSTE24kd and LMNAkd cells. However, the actual cell fate between both knockdowns differed. Whereas ZMPSTE24kd cells resorted to a senescence pathway (shown by β -galactosidase and p21 staining as well as upregulation of *IL6*), LMNAkd cells rather experienced increased apoptosis (evidenced by an increased number of cells with fragmented nuclei and $\Delta\psi_m$ hyperpolarization, which is known to precede apoptosis^{226,227}). These results align well with earlier findings. Indeed, premature senescence was observed in *Zmpste24*^{-/-} MEFs, *Lmna*^{G609G/G609G} MEFs, ZMPSTE24 depleted hMSCs and HGPS fibroblasts^{136,221,228,229}, and apoptosis was increased in *Lmna*^{-/-} MEFs, especially when subjected to mechanical stress^{55,219}, in myocytes from *Lmna*^{E82K/+} transgenic mice²³⁰ and in *Lmna*^{+/-} atrioventricular nodal mouse myocytes.¹⁴⁵ This bifurcation in cell fate might be triggered by the extent of mature lamin A reduction, which translates into a ROS dosage effect. It has been shown that modestly increased levels of intracellular ROS induce and maintain cellular senescence, as observed in ZMPSTE24kd cells, while higher doses provoke apoptosis, i.e. LMNAkd cells.^{231–234}

In conclusion, we demonstrated that sustained knockdown of *LMNA* or *ZMPSTE24* resulted in increased basal ROS levels, which were accompanied by changes in mitochondrial function and altered gene expression of ROS detoxifying enzymes.

Reduction of LA caused a dramatic increase in basal and, especially, induced ROS levels ultimately leading to $\Delta\psi_m$ hyperpolarization and apoptosis. Depletion of *ZMPSTE24* on the other hand, triggered a senescence pathway, associated with moderately increased ROS levels and transient $\Delta\psi_m$ depolarization. Thus, LA and PLA differentially regulate cell fate, in part via a redox-dependent pathway. Uncovering the pathways that lead to increased ROS production will help understanding laminopathy diversity and disease progression.

2.4. Materials and methods

Cell culture

Normal human dermal fibroblasts (NHDF, *LMNA*^{+/+}, Promocell, C-12300), fibroblasts from a patient with a lethal laminopathy phenotype due to a nonsense Y259X homozygous mutation in the *LMNA* gene (*LMNA*^{Y259X/Y259X})²⁰⁷ and fibroblasts from a patient suffering from HGPS (*LMNA*^{G608G/+})²⁰⁸ were cultured in T25 or T75 culture flasks in DMEM High Glucose with L-Glutamine medium (Lonza, BE12-604F) supplemented with 10% fetal bovine serum (Gibco, 10500-064) and 1% penicillin/streptomycin/L-glutamine (Gibco, 10378-016), at 37°C and 5% CO₂, according to standard procedures. All experiments were performed with cells in between passage 9 and 20. In case of direct comparison, passage-matched cells were used. At set time points, viable cells were counted using Trypan blue and a Bürker chamber. Proliferative capacity was expressed in terms of population doubling level (PDL), the base 2 logarithm of the number of cells at the current time point divided by the number of cells that was seeded.

siRNA-mediated knockdown

Expression of *ZMPSTE24* and *LMNA* was silenced with siGENOME Lamin A/C siRNA (Thermo Scientific, D-001050-01-20) and siGENOME Human *ZMPSTE24* siRNA (Thermo Scientific, M-006104-02-0020), respectively. Stealth RNAi siRNA Negative Control, Med GC (Life Technologies, 12935-300) was used as a negative non-targeting control (NTkd). siRNA transfections were performed using Lipofectamine® RNAi-MAX Transfection Reagent (Life Technologies, 13778-075), according to manufacturer's instructions following the scheme outlined in Figure 2-8.

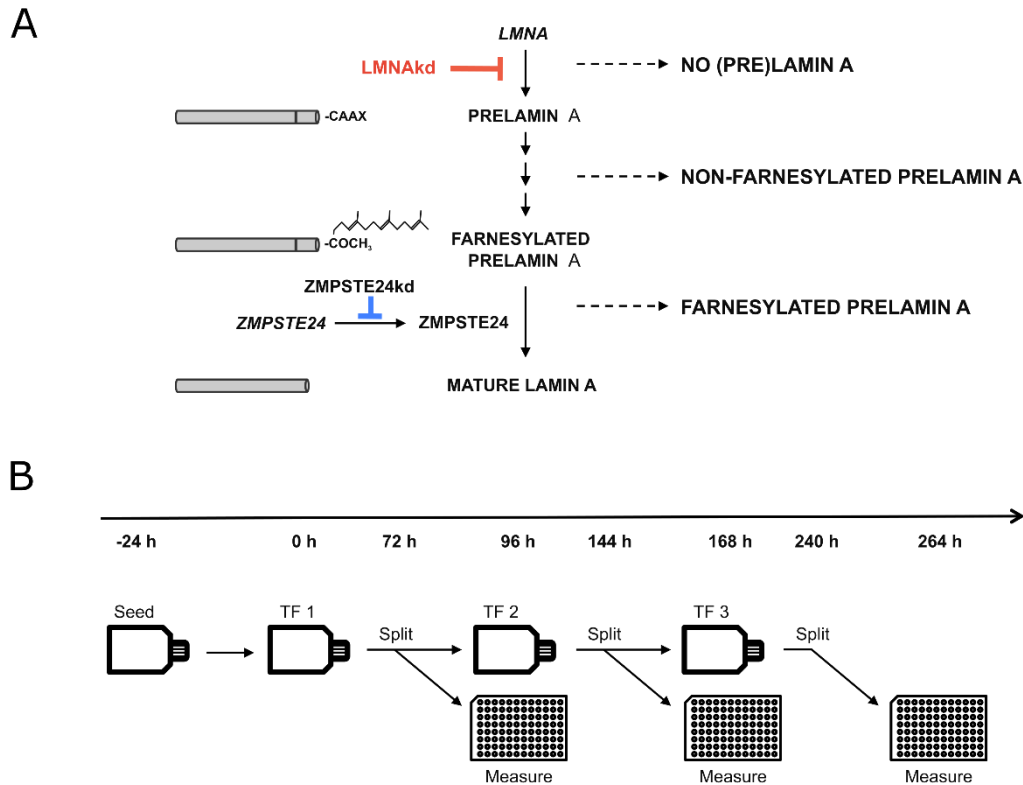


Figure 2-8. A: Schematic overview of the maturation process of prelamin A to mature lamin A and interference by siRNA-mediated knockdown. B: Experimental design of the sustained siRNA-mediated knockdown by repetitive transfections (TFs).

Quantitative PCR

RNA was extracted from cells using the RNeasy mini kit (Qiagen, 74104), with on-column DNase digestion. Concentrations of purified RNA were measured with the NanoDrop 2000 (Thermoscientific). Per sample, 1 μ g of RNA was converted to cDNA using SuperScript® III Reverse Transcriptase (RT) (Life Technologies, 18080-044). All qPCR reactions were performed on a RotorGene 3000 (Qiagen/Corbett) using the SensiMix™ SYBR® No-ROX Kit (Bioline, QT650) according to the manufacturer's instructions. Relative abundance of *LMNA* transcripts (forward: TGGACGAGTACCAGGAGCTT; reverse: ACTCCAGTTTGCCTTTTTG), *ZMPSTE24* transcripts (forward: CGAGAAGCGTATCTTCGGG; reverse: TGTGCTAGGAAGGTCTCCCA), *SOD1* transcripts (forward: GACCTGCACTGGTACAGCCT; reverse: GCATCATCAATTTGAGCAG), *SOD2* transcripts (forward: GGAGAAGTACCAGGAGGCGT; reverse: TAGGGCTGAGGTTTGTCCAG), *SOD3* transcripts (forward: TCTCTTGAGGAGCTGGAAA; reverse: CGAGTCAGAGTTGGGCTCC), *IL6* transcripts (forward: AGTGAGGAACAAGCCAGAGC; reverse: GTCAGGGGTGGTTATTGCAT), *GSTT2* transcripts (forward: ACGCTCAAGGATGGTGATTT; reverse: AGGTACTCATGAACACGGGC), *GPX1* transcripts (forward: CCGAGAAGGCATACACCGAC; reverse: ...)

GCCGGCCAGTTAAAAGGAGG), *GPX5* transcripts (forward: ACAAGTCCCAAGCAGGAGAA; reverse: TGACGAAGAGGATGTGCTTG), *PRDX1* transcripts (forward: GCTGTTATGCCAGATGGTCAG; reverse: GGGCACACAAAGGTGAAGTC), *PRDX2* transcripts (forward: GTCCTTCGCCAGATCACTGT; reverse: TGGGCTTAATCGTGTCACTG) and *PRDX3* transcripts (forward: CCACATGAACATCGCACTCT; reverse: TTGACGCTCAAATGCTTGAT) were measured relative to *ACTB* (forward: CCTTGCACATGCCGGAG ; reverse: GCACAGAGCCTCGCCTT) and *GAPDH* (forward: TGCACCACCAACTGCTTAGC; reverse: GGCATGGACTGTGGTCATGAG) reference transcripts. Ct-values were calculated using the 'comparative quantification' (CQ) method supplied as part of the Rotor Gene 3.0 software (Corbett Research). Analysis was done using the $\Delta\Delta$ Ct-method.²³⁵

Immunofluorescence staining

NHDF cells were grown on glass coverslips and fixed in 4% paraformaldehyde for 15 minutes at room temperature and washed (3x, 5 minutes) with PBS. Subsequently, cells were permeabilized with 0.5% Triton X-100 (5 minutes), after which they incubated with primary antibody diluted in 50% fetal bovine serum (FBS) for 60 minutes. After minimally 3 PBS wash steps, slides were incubated with secondary antibody diluted in 50% FBS for 30 minutes, washed again, and mounted with VECTASHIELD™ Mounting Medium (VWR, 101098-042) containing 1 µg/ml 4',6-diamino-2-phenylindole (DAPI). Primary antibodies were directed against lamin A (Abcam, ab26300) and prelamin A (Santa Cruz Biotechnology Inc., SC-6214). As secondary antibodies DyLight 488 conjugated donkey anti-rabbit (Jackson ImmunoResearch Laboratories Inc., JAC-705606147), and DyLight 649 conjugated donkey anti-goat (Jackson ImmunoResearch Laboratories Inc., JAC-705496147) were used. Immunofluorescent stained cells were visualized using a Nikon Ti Eclipse inverted widefield fluorescence microscope (Nikon Instruments) with 40x Plan Apo oil (NA = 1.3) and 60x Plan Apo VC (NA = 1.4) objectives.

β-galactosidase staining

NHDF cells were grown on glass coverslips and fixed in 4% paraformaldehyde for 15 minutes at room temperature and washed (2x, 5 minutes) with PBS. Fixed cells were incubated overnight at 37°C in 1 mg/ml X-Gal, 40 mM citric acid/phosphate buffer (pH 6), 5 mM ferricyanide, 5 mM ferrocyanide, 2 mM MgCl₂ and 150 mM NaCl. After incubation, the cells were washed (3x, 5 minutes) with PBS and permeabilized with 0.5% Triton X-100 (5 minutes). The cells were washed (3x, 5 minutes) with PBS and mounted with VECTASHIELD™ Mounting Medium (VWR, Belgium, 101098-042) containing 1 µg/ml 4',6-diamino-2-phenylindole (DAPI). Cells were visualized using a Nikon Ti Eclipse inverted widefield fluorescence microscope (Nikon Instruments) with a 40x Plan Apo oil (NA = 1.3) objective.

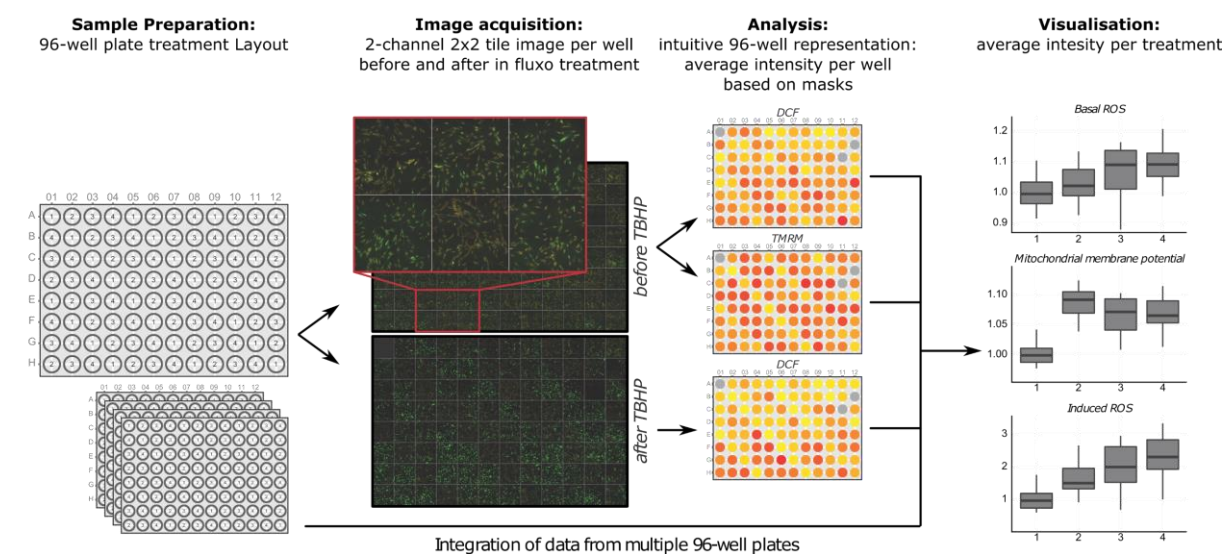
Western blot

Cells were grown in T75 culture flasks and lysed using the whole-cell extraction protocol of the Nuclear Extract Kit (Active Motif, 40010). Protein concentration was measured with the Pierce 660 nm assay (Thermo Scientific, 22662). Cell lysates were subjected to SDS-PAGE (8% bis-tris with MOPS running buffer) and transferred to BioTrace PVDF membranes (Pall Corporation, 66542). Primary antibodies were directed against lamin A/C (Santa Cruz Biotechnology Inc., sc-56139) and nucleolin (control) (Novus Biologicals, NB600-241). HRP conjugated goat anti-mouse (Sigma-Aldrich, A4416) and HRP conjugated goat anti-rabbit (Sigma-Aldrich, A6154) were used as secondary antibodies. Proteins were detected by chemiluminescence with Immobilon Western chemiluminescent HRP substrate (Millipore, WBKLS0100).

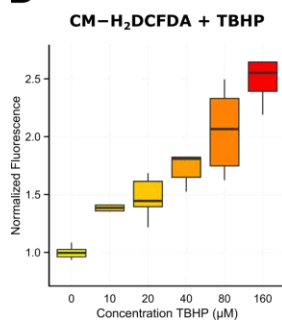
High content live cell imaging of intracellular ROS and $\Delta\psi_m$

Intracellular ROS and $\Delta\psi_m$ were measured after dual staining with the fluorescent cell-permeable probes 5-(and-6)-chloromethyl-2',7'-dichlorodihydrofluorescein diacetate (CM-H₂DCFDA) (Life Technologies, C6827) and tetramethyl rhodamine methyl ester (TMRM, Invitrogen, T-668). Measurements were done 96 h, 168 h and 264 h after initiation of the knockdown (Figure 2-8B). 24 h before measurement, cells were transferred to 96-well plates at 2500 cells per well. Right before measurement they were washed in HBSS + Hepes (HH) (pH 7.2), incubated for 25 minutes in the dark at room temperature in HH-buffer containing 2 μ M CM-H₂DCFDA and 20nM TMRM, washed again in HH-buffer and then imaged (also in HH-buffer) on a Nikon Ti Eclipse inverted widefield fluorescence microscope with a 20x air Plan Apo objective (NA 0.75) using a 480/40 nm excitation, 520/35 nm emission filter combination for the CM-H₂DCFDA signal and a 540/25 nm excitation, 605/55 nm emission filter combination for the TMRM signal. Since fluorescence excitation induces the formation of ROS²³⁶, the CM-H₂DCFDA signal increases during microscopic observation. To avoid excessive light exposure, the focal plane was searched with diffuse transmitted light. Subsequently an infrared-led based autofocus (Perfect Focus System, Nikon) was used, after which images were acquired automatically across the plate (4 images per well and per channel), the CM-H₂DCFDA channel first. After the complete plate was imaged, 20 μ M *tert*-butyl peroxide (Sigma-Aldrich, 458139-100mL) was added to all wells and after a 3-minute interval the acquisition was repeated. The workflow is depicted in Figure 2-9A. The method was benchmarked with different doses of TBPH (Figure 2-9B). TMRM reporter potential was validated with valinomycin (Sigma) (Figure 2-9C) and oligomycin (Sigma) (Figure 2-9D), known inducers of $\Delta\psi_m$ depolarization, respectively hyperpolarization.

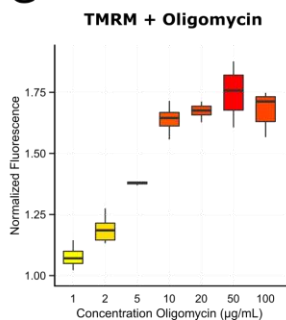
A



B



C



D

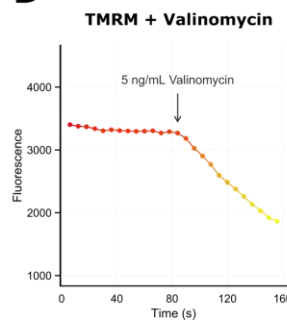


Figure 2-9. A: Schematic overview of the high-content workflow to simultaneously measure intracellular ROS levels and $\Delta\psi_m$. B: Normalized levels of intracellular ROS measured by CM-H₂DCFDA high content microscopy in human fibroblasts treated for 15 minutes with increasing concentrations of TBHP. C: Normalized $\Delta\psi_m$ as measured by TMRM in human fibroblasts treated for 30 minutes with increasing concentrations of oligomycin. D: Live cell imaging of $\Delta\psi_m$ in human fibroblasts loaded with TMRM and treated with 5 ng/mL valinomycin after 85s. The experiments were performed in triplicate and a minimum of 100 cells were imaged per replicate. In the boxplots, the horizontal line indicates the median, boxes the 25th and 75th percentile, and whiskers the 5th and 95th percentile.

An analogous experimental setup was used for measuring mitochondrial superoxide levels with MitoSOX Red Reagent (Life technologies – M36008). This dye was combined with the pan-cellular, viability dye Calcein Green (Life Technologies – C34852) to simplify cell segmentation in downstream image analysis and exclude dead cells from the analysis.²³⁷ In brief, cells were grown in 96-well plates, washed in HH-buffer, incubated in HH-buffer with 5 µM MitoSOX Red Reagent and 0.930 µM Calcein for 10 minutes at 37°C in the dark, washed again and imaged 1x with the same 4 images/well acquisition protocol. The dynamic range of MitoSOX was determined via TBPH addition. All experiments were performed with at least 8 replicates per treatment per plate (depending on the experiment), on at least 3 different plates.

For MG132 treatment, 2000 cells were seeded in 96-well plates 2 days before measurement, 16h prior to staining, cells were treated with 10 μ M MG132 (Santa Cruz – SC-201270).

Image analysis

All image processing was performed in FIJI (<http://fiji.sc>), a packaged version of ImageJ freeware (W.S. Rasband, U.S.A. National Institutes of Health, Bethesda, Maryland, USA, <http://rsb.info.nih.gov/ij/>, 1997–2014). Quantification of nuclear signal intensities of immunostained cell cultures using INSCYDE.ijm, a script for high content analysis.⁵⁶ Additionally, a new script was written for automated analysis of intracellular ROS and mitochondrial characteristics (RedoxMetrics.ijm). In brief, the image analysis pipeline consists of a flatfield correction to correct for illumination heterogeneity, noise reduction by Gaussian filtering and cell or mitochondrial segmentation and subsequent feature analysis of regions of interest. For CM-H2DCFDA or Calcein counterstained images, cells were segmented by autothresholding according to Huang's algorithm and average intensities were measured within the segmented regions. For measurement of mitochondrial signals, mitochondria were first selectively enhanced by local contrast enhancement and multi-scale Laplacian filtering⁵⁶ after which binarization was performed using Huang's algorithm. The resulting mask was used for analyzing shape metrics of objects larger than a predefined size (> 3 pixels) on the original image. All scripts are available upon request.

Respirometry

The Seahorse Extracellular Flux XF24 analyzer (Seahorse Bioscience) was used to provide a comprehensive assessment of the relative state of aerobic metabolism in live cells in assessing mitochondrial function. Seeding density and concentration of Mitostress kit (Seahorse Bioscience, 101848-400) components were optimized according to the manufacturers guidelines. Fibroblasts were seeded at a concentration of 20000 cells per well the day prior to the experiment. OCR was measured before addition of any compound (basal OCR), after addition of oligomycin (0.5 μ M final concentration), carbonyl cyanide p-trifluoromethoxyphenylhydrazone (FCCP, 0.5 μ M) and rotenone/antimycin (0.5 and 0.05 μ M). The OCR linked to coupled respiration was obtained by subtracting OCR after the addition of oligomycin from basal OCR. OCR after addition of the mitochondrial uncoupler FCCP reflected the maximal respiratory rate (spare respiratory capacity). Non-mitochondrial respiration was defined as the rate after rotenone/antimycin A application and was subtracted from the basal OCR to determine the mitochondrial OCR.

Statistical analyses

Data analysis and visualization was performed in R statistical freeware (<http://www.r-project.org>). Standard statistical methods were employed, including the Shapiro-Wilk Normality Test to assess normality of the data, Levene's test to assess homoscedasticity, student's t-test, ANOVA and the Kruskal-Wallis rank sum test to

assess differences between the group means and Tukey (after ANOVA) and Dunnett type (After Kruskal-Wallis) post-hoc tests to assess significance for each group. We also used non-parametric contrast-based multiple comparison tests.²³⁸ Significance levels were indicated as follows: $p < 0.05$ (*), $p < 0.01$ (**), and $p < 0.001$ (***). For graphics and annotation, the R program was expanded with the ggplot2 package.²³⁹

3

DEREGULATION OF FOCAL ADHESION FORMATION AND CYTOSKELETAL TENSION DUE TO LOSS OF A-TYPE LAMINS

This work is published in: Corne TDJ, Sieprath T, Vandenbussche J, Mohammed D, te Lindert M, Gevaert K, Gabriele S, Wolf K, De Vos WH. Deregulation of focal adhesion formation and cytoskeletal tension due to loss of A-type lamins. *Cell Adhes Migr* 2016; 0:1–17.

Abstract

The nuclear lamina mechanically integrates the nucleus with the cytoskeleton and extracellular environment and regulates gene expression. These functions are exerted through direct and indirect interactions with the lamina's constituent proteins, the A-type lamins, which are encoded by the *LMNA* gene. Using quantitative stable isotope labeling-based shotgun proteomics we have analyzed the proteome of human dermal fibroblasts in which we have depleted A-type lamins by means of a sustained siRNA-mediated *LMNA* knockdown. Gene ontology analysis revealed that the largest fraction of differentially produced proteins was involved in actin cytoskeleton organization, in particular proteins involved in focal adhesion dynamics, such as actin-related protein 2 and 3 (ACTR2/3), subunits of the ARP2/3 complex, and fascin actin-bundling protein 1 (FSCN1). Functional validation using quantitative immunofluorescence showed a significant reduction in the size of focal adhesion points in A-type lamin depleted cells, which correlated with a reduction in cell adhesion capacity after seeding on collagen, and an increased cell motility. At the same time, loss of A-type lamins led to more pronounced stress fibers and higher traction forces in cells undergoing enzymatic detachment. This phenotype could not be mimicked or reversed by experimental modulation of the STAT3-IL6 pathway, but it was partly recapitulated by chemical inhibition of the ARP2/3 complex. Thus, our data suggest that the loss of A-type lamins perturbs the balance between focal adhesions and cytoskeletal tension. This imbalance may contribute to mechano-sensing defects observed in certain laminopathies.

3.1. Introduction

The nuclear lamina, a thin filamentous protein layer beneath the nuclear envelope, physically supports the cell nucleus and has a central role in nuclear organization and gene regulation.¹⁴ The major constituents of this meshwork are type V intermediate filament proteins, known as lamins. Mutations in the *LMNA* gene, which encodes A-type lamins, cause a wide spectrum of tissue-specific and systemic diseases collectively called laminopathies. Disease manifestations include muscular dystrophies, lipodystrophies, dilated cardiomyopathies and the premature aging syndromes Hutchinson-Gilford progeria (HGPS) and restrictive dermopathy (RD).¹⁴ Since the nuclear lamina is involved in gene regulation through chromatin organization and sequestration of transcription factors^{14,136,240–242}, mutations in genes encoding nuclear lamins directly affect gene expression. Indeed, microarray analysis of HGPS fibroblasts^{136,243} and of *Lmna* deficient MEFs⁸⁵ have revealed large-scale changes in the transcriptome with respect to their wild-type counterparts. However, the stability and function of the encoded proteins are regulated by post-translational modifications and interactions, precluding direct extrapolation of gene expression data to protein level changes. A limited number of pioneering studies has documented changes in global protein expression in laminopathy patient cells or mouse model cells.^{128,205,244,245} However, the genetic variability between patients and the lower translational value of

animal model cells complicate extraction of causal effects.^{195–197} Therefore we have now analyzed proteome changes in a controlled, isogenic cell system, namely human dermal fibroblasts in which we depleted A-type lamins by means of sustained siRNA-mediated knockdown²⁴⁶, with the underlying reasoning that this may have value for better understanding laminopathies that are characterized by reduction (haploinsufficiency) or loss of A-type lamins, among which certain cardiomyopathies.^{142,144} We identified several proteins with significantly altered abundance that were involved in focal adhesion (FA) kinetics: actin-related protein 2 (ACTR2), actin-related protein 3 (ACTR3) and fascin actin-bundling protein 1 (FSCN1). We validated and complemented proteomics with functional studies, showing an unexpected uncoupling between cell adhesion and cytoskeletal tension.

3.2. Results

SILAC-based quantitative analysis in A-type lamin depleted fibroblasts reveals changes in the cytoskeletal proteome

To study the impact of A-type lamin depletion on global protein expression, we performed a SILAC-based quantitative proteomics experiment on human dermal fibroblasts after sustained knockdown of *LMNA* (LMNAkd). RT-qPCR revealed a ~16-fold decrease of *LMNA* transcripts in LMNAkd cells. Lamins A and C were virtually absent on western blot and a ~2.8-fold decrease was observed via immunofluorescent staining of lamin A, essentially approximating background levels. LMNAkd cells also showed a significant increase of dysmorphic nuclei compared to control cells that were treated with a non-targeting control siRNA (NTkd) (3.0-fold increase).

Using the SILAC based proteomics approach depicted in Figure 3-1A, we identified a total of 1,341 proteins, of which 75 showed significant differential expression ($p < 0.05$). 42 proteins were more abundantly and 33 were less abundantly present in LMNAkd cells than in NTkd cells. Gene ontology (GO) analysis of the protein class indicated that the largest group (23.7%) of the proteins were cytoskeletal or cytoskeleton-associated. Gene ontology enrichment analysis (GOzilla) returned five GO terms that were significantly enriched for this protein set, namely 1) positive regulation of cellular component biogenesis, 2) regulation of cellular component biogenesis, 3) regulation of actin filament-based process, 4) ARP2/3 complex-mediated actin nucleation, and 5) regulation of actin filament polymerization (Figure 3-1B). A subset of 16 top hits that showed a relative fold change higher than 2 (CLIC4, DES, DLD, HSPB1, PLOD2, SAP18, SERPINB8, TGM2 and TPM1) or lower than 0.5 (ANXA4, ACTR2, ACTR3, ARPC4, EIF4G2, FSCN1 and LMOD1) was analyzed with RT-qPCR to assess transcript levels. Nine genes showed a clear positive correlation between transcript and SILAC ratio, whereas 7 did not (Figure 3-1C).

Sustained LMNA knockdown alters abundance of ACTR2, ACTR3, FSCN1 and CLIC4

GO analysis revealed that the cytoskeletal proteome became strongly affected in LMNAkd cells. We therefore validated four of the most prominently altered cytoskeletal or cytoskeleton-associated proteins using western blot, namely actin-related protein 2 (ACTR2) and actin-related protein 3 (ACTR3), subunits of the ARP2/3 complex, fascin actin-bundling protein 1 (FSCN1), a protein that organizes F-actin into parallel bundles and is involved in FA disassembly and chloride intracellular channel protein 4 (CLIC4), which is involved in diverse processes such as cell migration and wound healing and may be important for regulating cytoskeletal organization during the cell cycle.^{247,248} ACTR2, ACTR3 and FSCN1 proteins were found to be significantly less abundant in LMNAkd cells (ACTR2: 2.6-fold, ACTR3: 2.3-fold, and FSCN1: 2.8-fold decrease) in accordance with their SILAC ratio (ACTR2: 2.5-fold, ACTR3: 2.8-fold, and FSCN1: 3.0-fold decrease), but only *FSCN1* also showed lower mRNA levels (3.7-fold decrease). CLIC4 protein abundance and mRNA levels were both significantly increased (2.3-fold and 5.7-fold increase respectively) similar to the SILAC ratio (3.1-fold increase) (Figure 3-1D & E).

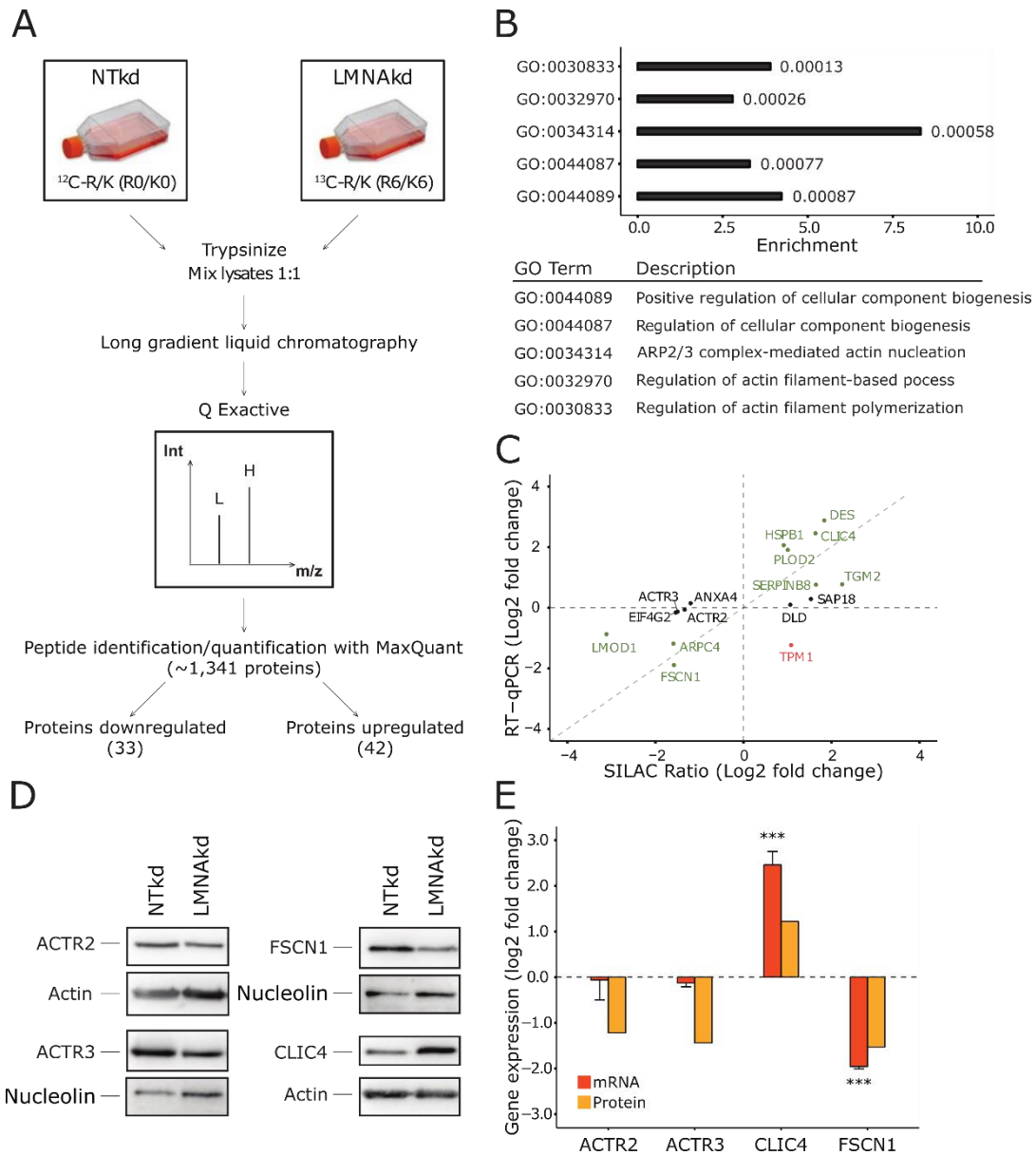


Figure 3-1. SILAC based quantitative proteomics of human dermal fibroblasts after sustained LMNAkd indicate that depletion of lamin A/C influences the levels of proteins involved in actin cytoskeleton organization. A: Schematic overview of the SILAC experiment (see materials and methods for details). L = light medium, H = heavy medium, Int = intensity, m/z = mass/charge ratio. B: Proteins that showed significant differences ($p < 0.05$) in the SILAC dataset were analyzed with Gorilla, yielding a subset of significantly affected pathways (p-value for the respective GO term depicted next to the bars). C: Scatterplot between mRNA level, measured by RT-qPCR relative to non-targeting control (NTkd), and SILAC ratio. Genes in green text color showed correlation, genes in black text color showed no correlation, and genes in red text color showed inverse correlation. D: Western blot analysis of ACTR2, ACTR3, FSCN1 and CLIC4. Nucleolin or actin was used as a loading control. E: Gene expression levels of ACTR2, ACTR3, FSCN1 and CLIC4 measured by real-time qPCR relative to NTKd (in orange) and protein levels of ACTR2, ACTR3, FSCN1 and CLIC4 semi-quantified with western blot analysis (in yellow). Error bars indicate the standard deviation on the mean value of three biological replicates; significance was calculated with a Student's t -test; *** = p -value < 0.001 .

A-type lamin depletion reduces focal adhesion area

Since ARP2/3 and FSCN1 are directly involved in FA formation and disassembly, respectively, we quantified FAs by immunofluorescent staining of paxillin, vinculin and focal adhesion kinase (FAK) (Figure 3-2A) and quantitative image analysis (Figure 3-2B-D).⁵⁶ In contrast with paxillin and vinculin, the FAK antibody did not reliably stain FA. However, we did observe a significant decrease in nuclear FAK signal in LMNAkd cells (Figure 3-2I). Fluorescence intensity of paxillin foci was significantly decreased in LMNAkd cells compared to NTkd cells (-11.6%), as was the number of FAs per cell (-46%), and the area per FA (-11.5%). In contrast, the number, shape (circularity) and fluorescence intensity of vinculin foci was not significantly altered; only the area showed a significant decrease in LMNAkd cells (-13.2%). Western blot analysis revealed a 2.4-fold decrease in paxillin protein abundance after LMNAkd, which was in line with the (non-significant) 1.6-fold decrease in the SILAC data. Vinculin and FAK protein levels were unaltered (Figure 3-2E). We also analyzed mRNA expression of paxillin with RT-qPCR and measured a 2.1-fold decrease of *PXN* expression. To assure that the effects on FA were specifically caused by A-type lamin depletion, we rescued *LMNA* expression in LMNAkd cells by prolonged culturing after a sustained knockdown in absence of siRNA. The number and area of paxillin foci restored when lamin A/C levels returned back to basal levels after 1 week in the absence of siRNA, suggesting a direct causal effect (Figure 3-2F-H).

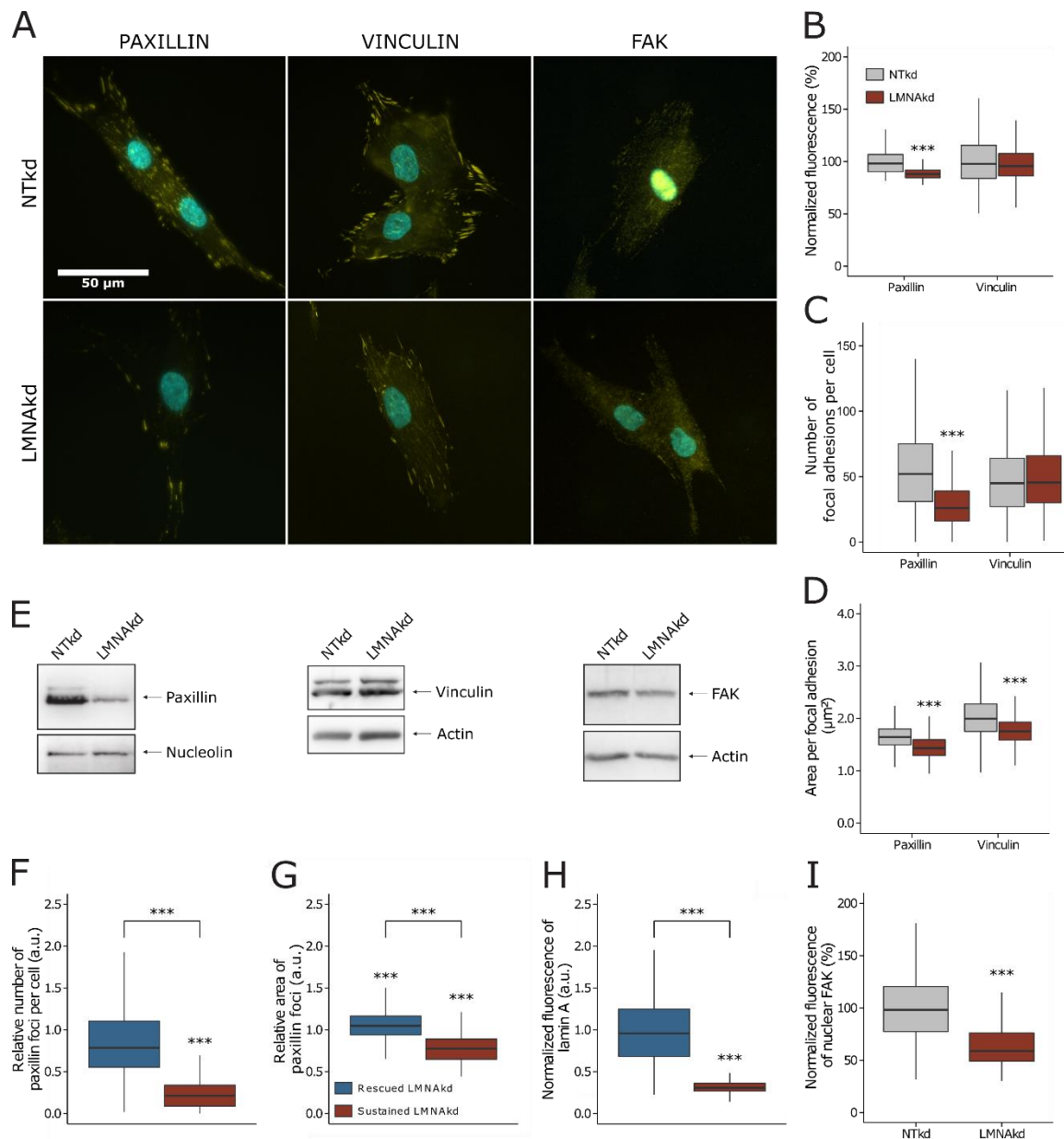


Figure 3-2. A-type lamin depletion reduces focal adhesion and rescue of LMNA expression alleviates the de-adhesive phenotype. A: Representative images of NTkd and LMNAkd cells after immunofluorescence staining for paxillin, vinculin or FAK (yellow) and counterstaining with DAPI (cyan). B: Normalized mean fluorescence (%) of FA points relative to the average of NTkd. C: Quantification of the number of FAs per cell. D: Area per FA (μ m²). E: Western blot for Paxillin, vinculin and FAK. Nucleolin or actin was used as a loading control. F: Number of FAs per cell relative to NTkd control 1 week after LMNAkd was either arrested or continued. G: FA area relative to NTkd control cells. H: Lamin A level relative to NTkd control cells. I: Normalized mean fluorescence (%) of nuclear FAK relative to NTkd cells. Immunofluorescent staining was performed in triplicate and a minimum of 100 cells were imaged per replicate. In the boxplots, the horizontal line indicates the median, boxes the 25th and 75th percentile, and whiskers the 5th and 95th percentile. For all figures, significance was calculated with the Wilcoxon rank sum test; *** = p-value < 0.001.

LMNAkd reduces adhesive capacity but increases contractile tension

Since a reduction in FA number or size may reduce cell adhesion we analyzed the net adhesive capacity of the fibroblasts seeded onto collagen-coated wells using a colorimetric cell adhesion assay. We observed a 60% reduction in initial cell adhesion in LMNAkd cells (Figure 3-3A). Intuitively, a reduced number of FA points, would also suggest less contractile tension in those cells that are attached. Concurrent phalloidin staining however, revealed more pronounced stress fibers in laminin A/C depleted cells as evidenced by an increased fluorescence intensity for the fibers (Figure 3-3B). To analyze whether the more pronounced stress fibers also increased contractile tension we performed traction force microscopy (TFM) using trypsin-mediated detachment of micro-patterned cells. TFM measurements showed a significant 2.8-fold increase in traction force, suggesting that LMNAkd cells display higher contractility (Figure 3-3C).

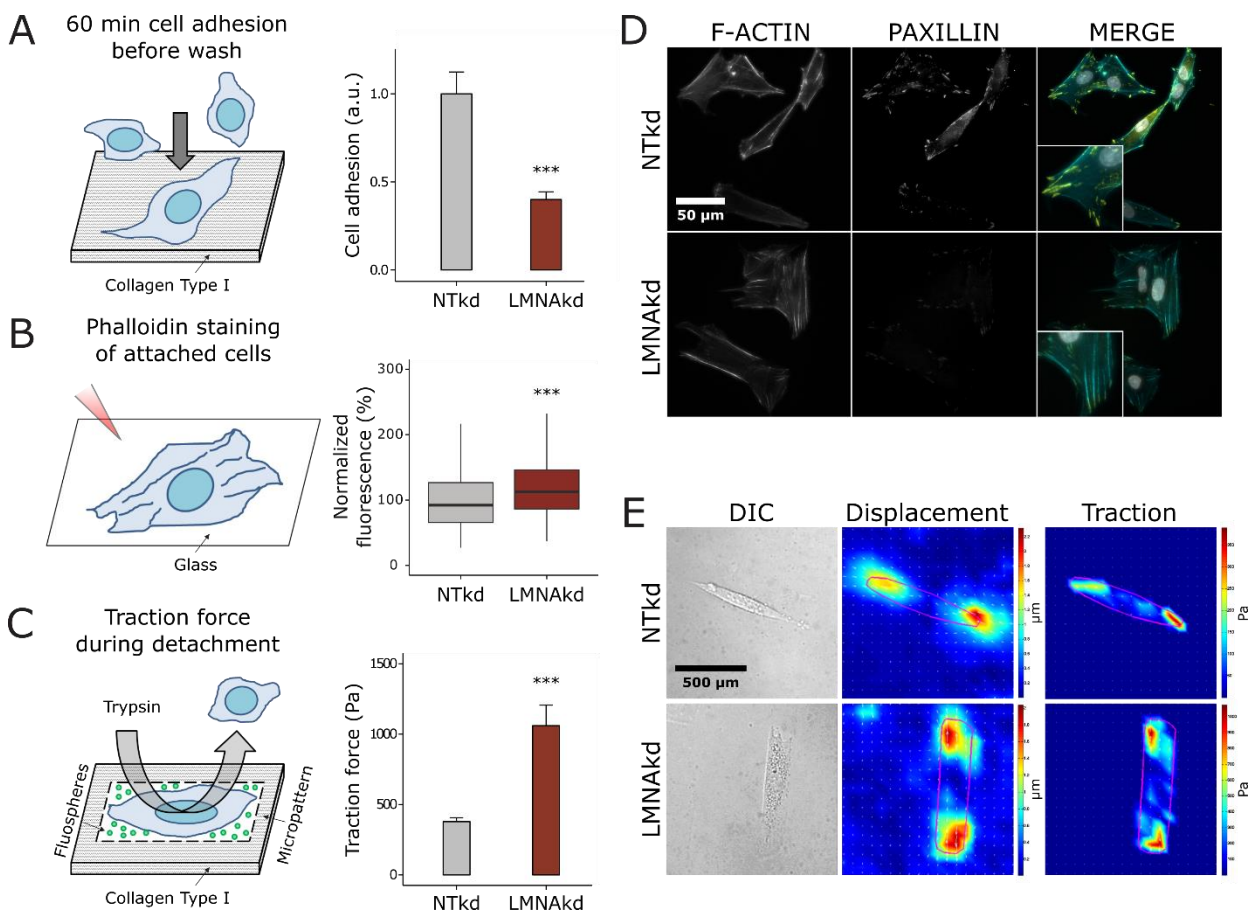


Figure 3-3. LMNAkd increases contractile tension, but reduces adhesive capacity. A: Schematic overview of the colorimetric cell adhesion assay. On the right site, the results of the assay are expressed relative to NTkd cells. Error bars indicate the standard deviation on the mean value of 10 replicates. B: Schematic overview of the rhodamine phalloidin staining used to characterize stress fibers of attached cells. On the right site, the normalized mean fluorescence intensity (relative to NTkd cells (%)) of stress fibers per cell is shown, isolated by fast Fourier transformation filtering on rhodamine phalloidin images. Staining was conducted in triplicate and a minimum of 100 cells were imaged per replicate. In the boxplot, the horizontal line indicates the median, boxes the 25th and 75th percentile, and whiskers the 5th and 95th percentile. C: Schematic overview of the traction force microscopy experiment. On the right site,

maximum traction force in NTkd and LMNAkd cells is shown. Error bars indicate the standard deviation on the mean value of 8 NTkd cells and 10 LMNAkd cells. D: Representative images of NTkd and LMNAkd cells after immunofluorescence staining for paxillin (yellow), rhodamine phalloidin staining for actin (cyan) and counterstaining with DAPI (grey). E: Representative DIC images, heat maps of the displacement and heat maps of the traction forces in NTkd and LMNAkd cells based on TFM measurements (see materials and methods for details). For the TFM experiment, significance was calculated with the Students t test; *** = p-value < 0.001. For the other experiments significance was calculated with the Wilcoxon rank sum test; *** = p-value < 0.001.

A-type lamin depletion increases cell mobility but impairs directionality in wound healing

Since FA size dictates cell migration rate we analyzed cell migration by means of a wound healing assay.^{249–251} In general, LMNAkd induced a significant decrease in wound healing performance: the wound healing rate, expressed as the decrease of wound area as a function of time (see materials and methods), was approximately 38% lower than the rate of NTkd cells (Figure 3-4A, C & D). The average displacement of individual NTkd fibroblasts was not significantly different from that of the entire field of view, but for LMNAkd, cells at the leading edge (i.e. the first row of cells) displayed a significant increase in motility as compared to NTkd cells. Despite this increased motility, LMNAkd fibroblast movement lacked direction: whereas 100% of the NTkd cells moved towards the wound, only 33% of the LMNAkd cells showed this directionality (Figure 3-4B & E).

STAT3 knockdown does not reproduce the LMNAkd phenotype, nor does IL6/IL6R treatment alleviate the effects of LMNAkd

Previous studies have shown that signal transducer and activator of transcription 3 (*STAT3*) and interleukin 6 (*IL6*) induce *FSCN1* expression in breast cancer cells and human glioblastoma multiforme cells.^{252,253} In addition, both *STAT3* and *IL6* can affect cell migration.^{254,255} Since LMNAkd reduced *FSCN1* expression, we analyzed the gene expression of *STAT3*, *IL6* and interleukin 6 receptor (*IL6R*) with RT-qPCR. A significant decrease in expression of *STAT3* (7.1-fold) and *IL6R* (6.8-fold) was observed after LMNAkd. The protein level of *STAT3* was also decreased 2.3-fold, as shown by western blot.

To elucidate whether an LMNAkd-associated decrease in *STAT3* expression caused the decreased expression of *FSCN1*, *STAT3* gene expression was reduced by RNAi. Despite a 64-fold reduction in *STAT3* expression, no significant change in *FSCN1* expression could be detected. *IL6* expression was also unaffected by *STAT3* knockdown (*STAT3kd*), but the expression of *IL6R* was significantly decreased (10-fold). Wound healing potential was slightly increased, but this was not significant (Figure 3-5A & B). Immunofluorescent staining of paxillin indicated that the number of FAs per cell and the area was unaltered after *STAT3kd* (Figure 3-5C & D).

To check whether reduced *IL6R* expression contributed to the phenotype of LMNAkd cells, we treated LMNAkd cells with recombinant human *IL6* and *IL6* receptor (*IL6R*).

This however, did not restore *FSCN1* expression, nor did it affect wound healing potential, the number of FAs per cell or FA area (Figure 3-5E-H).

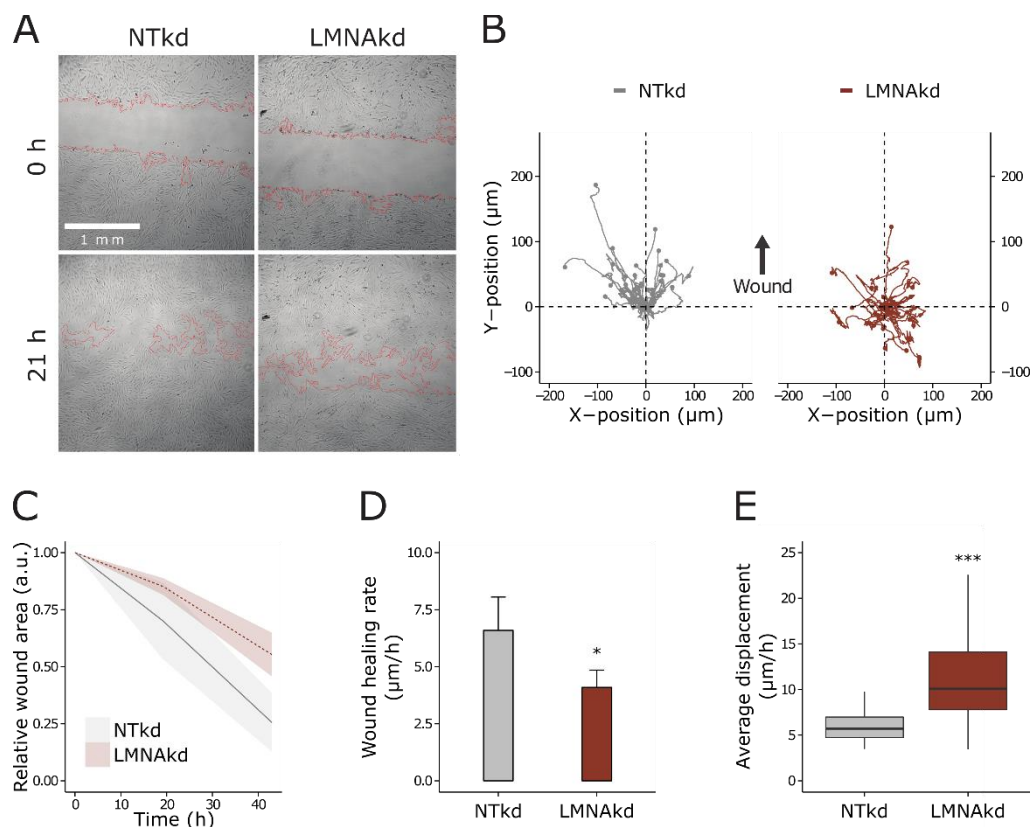


Figure 3-4. Lamin A/C depletion reduces wound healing potential, but increases single cell motility. A: Representative transmission images of the wound healing assay at two time points (0 and 21 h) of the experiment, the wound area is delineated in red. B: XY-movement of individual cells over 28 h, relative to the initial position. C: Normalized wound area at different time points, relative to the initial wound area. The line is the mean value, the shaded region indicates the standard deviation on the mean value of 8 replicates. D: Cell migration rate ($\mu\text{m}/\text{h}$) of NTKd and LMNAkd cells. Error bars indicate the standard deviation on the mean value of 8 replicates. E: Average displacement ($\mu\text{m}/\text{h}$) of cells, measured by tracking individual cells in time-lapse images of a wound healing assay. The line is the mean value, the shaded region indicates the standard deviation on the mean value of 8 replicates. In the boxplots, the horizontal line indicates the median, boxes the 25th and 75th percentile, and whiskers the 5th and 95th percentile. Significance was calculated in D with the Student's *t*-test and in E with the Wilcoxon rank sum test; * = *p*-value < 0.05; *** = *p*-value < 0.001.

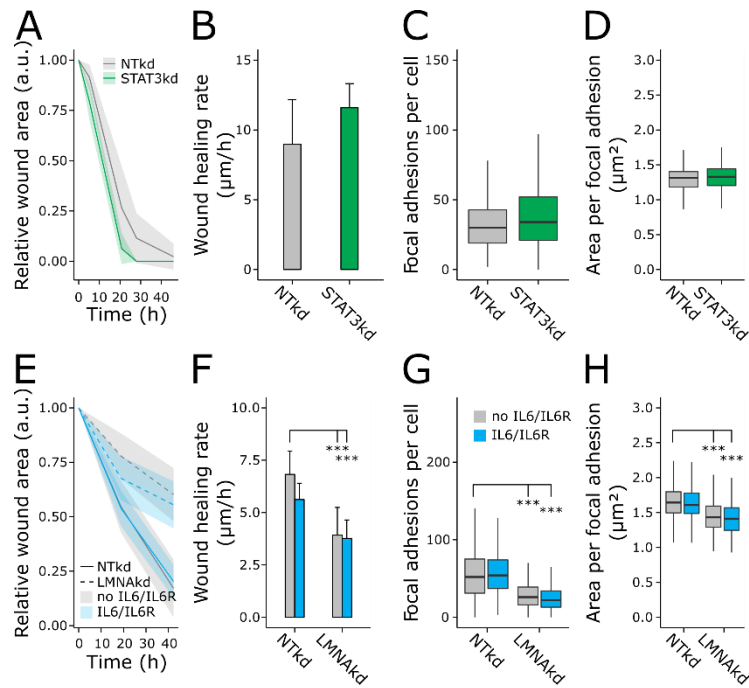


Figure 3-5. Impaired wound healing and FA after LMNAkd is not attributed to decreased *STAT3* or decreased *IL6/IL6R* expression. A: Normalized wound area at different time points, relative to the initial wound area, after STAT3kd compared to NTKd control. B: Cell migration rate ($\mu\text{m}/\text{h}$) of control and STAT3kd cells. C: Average number of FAs per cell after STAT3kd compared to NTKd control. D: Area per FA (μm^2) after STAT3kd compared to NTKd control. E: Normalized wound area at different time points, relative to the initial wound area, after LMNAkd compared to NTKd control in presence (blue) or absence of IL6/IL6R (grey). F: Cell migration rate ($\mu\text{m}/\text{h}$) of control and LMNAkd cells in presence (blue) or absence of IL6/IL6R (grey). G: Average number of FAs per cell after LMNAkd compared to NTKd control in presence (blue) or absence of IL6/IL6R (grey). H: Area per FA (μm^2) after LMNAkd compared to NTKd control in presence (blue) or absence of IL6/IL6R (grey). The lines in A and E are the mean values, the shaded regions indicate the standard deviation on the mean value of 8 replicates. Error bars in B and F indicate the standard deviation on the mean value of 8 replicates. Immunofluorescent staining was conducted in triplicate and a minimum of 100 cells were imaged per replicate. In the boxplots, the horizontal line indicates the median, boxes the 25th and 75th percentile, and whiskers the 5th and 95th percentile. For all figures, significance was calculated with either ANOVA or non-parametric contrast-based multiple comparison tests; *** = p-value < 0.001.

A-type lamin depletion affects nuclear translocation of MKL1

MKL1-SRF signaling is crucial for cytoskeletal organization and FA assembly and *FSCN1* is a target gene of serum response factor (SRF).^{256–258} Previous studies have shown that megakaryoblastic leukemia 1 (MKL1) – serum response factor (SRF) signaling is impaired in lamin A/C deficient cells.¹⁰⁵ We quantified MKL1 localization via immunofluorescence and observed a significant decrease in nuclear translocation of MKL1 in LMNAkd fibroblasts (Figure 3-6).

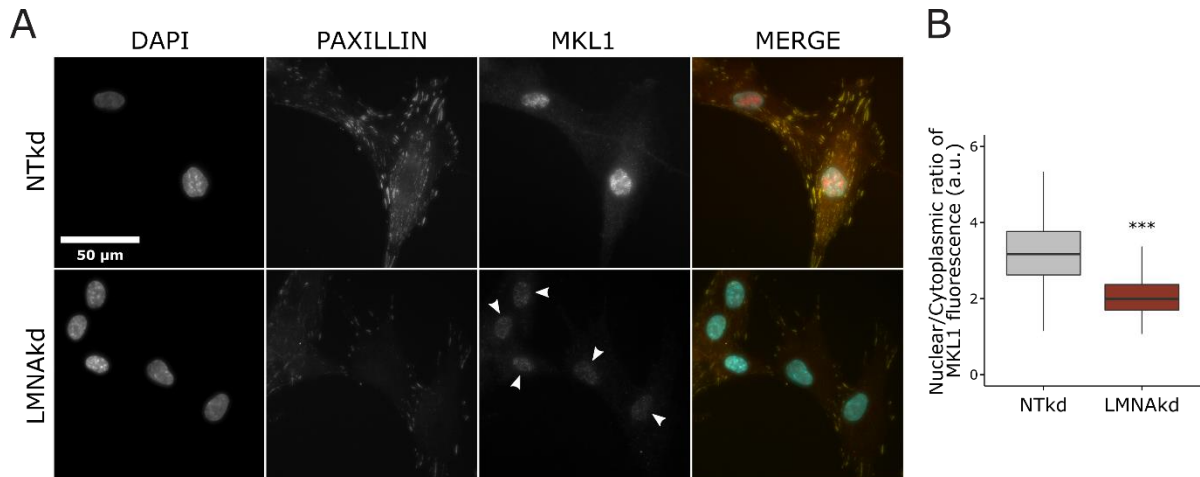


Figure 3-6. A-type lamin depletion reduces nuclear translocation of MKL1. A: Representative images of NTkd and LMNAkd cells after immunofluorescence staining for paxillin (yellow), MKL1 (red) and counterstaining with DAPI (cyan). Arrowheads show reduced nuclear MKL1 in LMNAkd cells. B: Normalized mean fluorescence (%) of nuclear MKL1 relative to NTkd cells. The immunofluorescent staining was conducted in triplicate and a minimum of 100 cells were imaged per replicate. In the boxplots, the horizontal line indicates the median, boxes the 25th and 75th percentile, and whiskers the 5th and 95th percentile. Significance was calculated with the Wilcoxon rank sum test; *** = p-value < 0.001.

ARP2/3 inhibition causes FA attrition

To investigate whether reduced protein levels of ACTR2 and ACTR3 impaired FA formation, we inhibited the ARP2/3 complex in normal fibroblasts with bardoxolone methyl (CDDO-me). Fibroblasts were treated for 2 hours with 5 µM or 10 µM CDDO-me. Both concentrations reduced the number, the fluorescence, and the area of paxillin foci as compared to vehicle treated cells (Figure 3-7), suggesting that ARP2/3 complex contributes to lamin A/ C mediated FA formation.

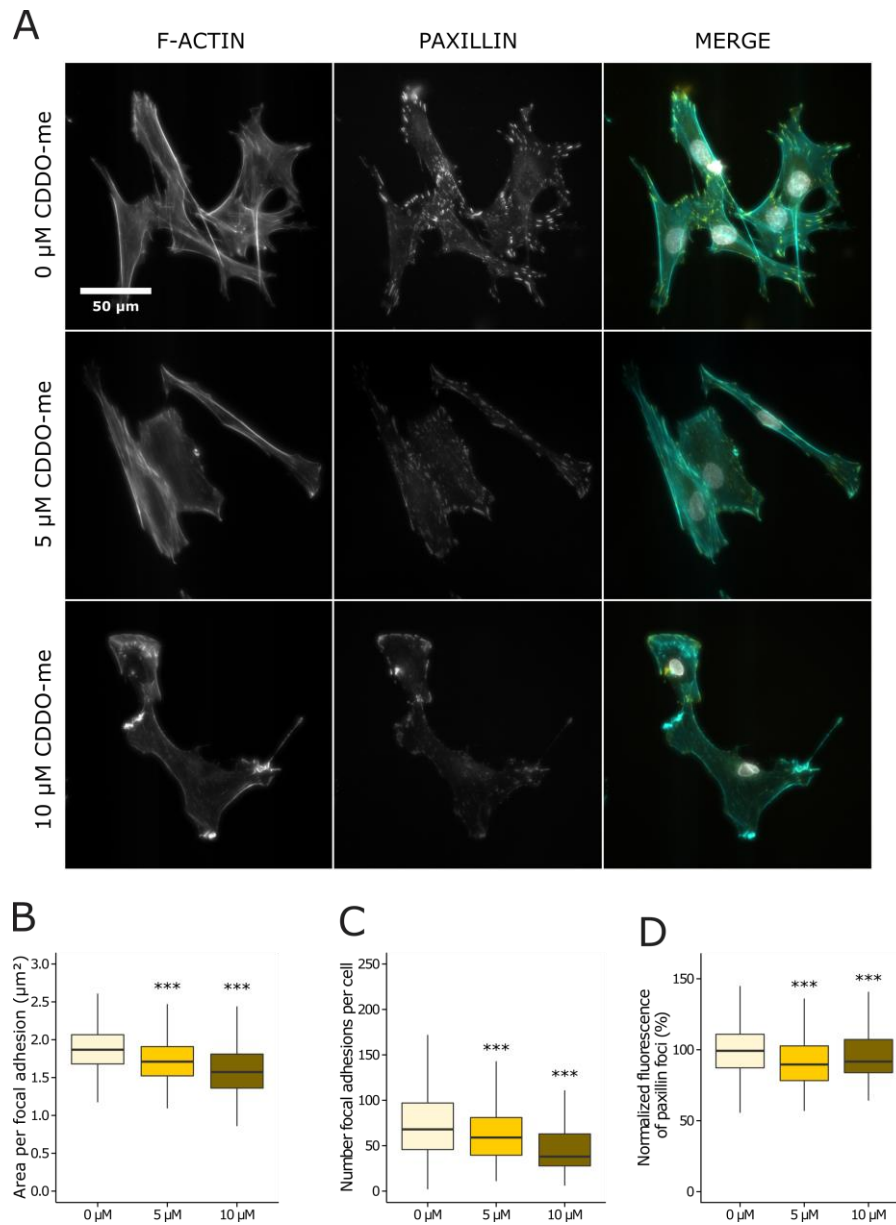


Figure 3-7. Chemical inhibition of the ARP2/3 complex by CDDO-me reduces FA and causes cell detachment. A: Representative images of fibroblasts treated with different concentrations of CDDO-me (0 μM , 5 μM and 10 μM) for two hours after rhodamine phalloidin staining for actin (cyan), immunofluorescence staining for paxillin (yellow), and counterstaining with DAPI (grey). B: Area per paxillin foci (μm^2). C: Number of paxillin foci per cell. D: Normalized mean fluorescence (%) of paxillin foci relative to vehicle treated cells. The immunofluorescent staining was conducted in triplicate and a minimum of 100 cells were imaged per replicate. In the boxplots, the horizontal line indicates the median, boxes the 25th and 75th percentile, and whiskers the 5th and 95th percentile. For all figures, significance was calculated with the Wilcoxon rank sum test; * = p-value < 0.05; ** = p-value < 0.01; *** = p-value < 0.001.

3.3. Discussion

To highlight the molecular changes that appear in the context of loss of A-type lamins, we performed a SILAC based quantitative proteomics experiment on human dermal fibroblasts after LMNAkd. Using GO enrichment analysis we found that proteins involved in actin cytoskeleton organization were affected by LMNAkd, which is in line with previous observations in fibroblasts from patients carrying *LMNA* mutations.²⁴⁵ What is novel in our data is a direct connection between the A-type lamins and FA formation. Specifically, proteins involved in FAs such as ACTR2, ACTR3, and FSCN1 were significantly downregulated in LMNAkd cells. Since *FSCN1* knockdown has been shown to increase FA surface and ARP2/3 has been shown to trigger FA formation, FA formation could be affected in both ways (up or down).²⁵⁹⁻²⁶¹ Via immunofluorescent staining and image analysis we discovered a significant reduction in the average FA size per cell for vinculin and paxillin, and a significant reduction in paxillin positive foci in LMNAkd cells. This corresponds well with earlier results reporting smaller FAs in *Lmna*^{-/-} MEFs, and a decrease in cell-matrix adhesion sites after mechanical challenge of *LMNA*-mutated (Δ K32-P1, R429W and L380S) myoblasts.^{262,263} Next to the effects on FA size, a remarkable decrease of nuclear FAK was observed in LMNAkd cells, which might be associated with decreased cell proliferation and increased inflammatory responses.²⁶⁴ Proliferation defects and increased apoptosis have been observed in LMNAkd and lamin A/C deficient cells.^{55,219,246} A reduction of FA size may suggest that LMNAkd cells are not as strongly attached to the substrate as NTKd cells, which was also indicated by an adhesion assay in which cells were allowed to attach for an hour before washing. However, such an assay only reflects the speed of attachment and not the actual adhesive potential or level of pre-stress in the attached cells. For those cells that were attached, we found more pronounced stress fibers and measured significantly higher traction forces during detachment, indicating increased cytoskeletal tension. More pronounced stress fibers might be attributed to a reduction in *FSCN1* expression, since *FSCN1* depletion has been shown to reorganize actin filaments into thicker, more contractile bundles, plausibly by slowing down actin polymerization at the stress fiber termini enabling the incorporation of a higher number of myosin II molecules.²⁶¹ Counter intuitively, the actin stress fibers can still attach to and exert even stronger traction forces on smaller FAs. However it should be emphasized that stress fibers, which are not directly anchored at FAs, such as transverse arcs, will also cover a portion of the measured traction forces, albeit to a lesser extent.²⁶⁵ Moreover, whilst FA are considered to be the predominant mechanism by which cells exert traction forces on their extracellular matrix, it has also been noted that small FA at the leading edge of a migrating cell developed greater traction force than the larger FA further away from the front, suggesting that there is no one-to-one relationship between FA size and tensile force.^{266,267} Increased traction force may represent a compensatory mechanism that arises from the loss or reduction of mechanical coupling between the cytoskeleton and the nucleus. Supporting this notion, is the increased traction force observed in Nesprin 1-depleted cells, aligning with their shared role in the LINC.²⁶⁸ However, in the latter cells a concomitant increase

in the number of focal adhesions was observed, whereas we have not detected a significant change in the absolute number of FA (as measured by vinculin).²⁶⁸ Our data thus revealed an apparent uncoupling between cell adhesive mechanisms and cytoskeletal tension. Similar uncoupling has previously also been documented for DAP kinase²⁶⁹, as it seems to promote disassembly of focal adhesions but not stress fibers in cells receiving serum factors²⁶⁹. Interestingly, DAP kinase enhances the formation of stress fibers in response to oxidative stress²⁷⁰, a hallmark of lamin A/C depleted cells.^{213,245,246} Loss of A-type lamins may thus activate a similar pathway. Since FA size dictates cell migration rate, we measured cell mobility by tracking individual cells at the leading edge in a wound healing assay. Whereas LMNAkd cells showed an overall lower wound healing potential quite similar to previous observations in *Lmna*^{-/-} MEFs and after LMNAkd in SW480 colon cancer cells^{263,271,272} motility of individual cells was indeed increased. This may be a direct effect of reduced *PXN* expression, since low levels of paxillin have been shown to increase motility in lung cancer cells.^{273,274} Similar observation have been linked to a decrease in vinculin expression.²⁷⁵ The reduced wound healing potential is rather due to a loss of directionality, which may be caused by delayed reorientation of the nucleus and the microtubule-organizing center towards the wound, but may also be aggravated by impaired FA formation.^{271,276}

The reduced expression of *FSCN1* after LMNAkd correlated with reduced *IL6R* and *STAT3* expression. In contrast, *IL6* showed a moderate increase in gene expression, possibly representing a compensatory mechanism. *STAT3* depletion could not reproduce the de-adhesive phenotype seen after LMNAkd nor did *IL6/IL6R* treatment alleviate the adhesive defects seen in LMNAkd cell. This might point to a cell-type specific regulation of *FSCN1* expression by the *IL6-STAT3* axis or cross-talk with other regulatory pathways.

Since MKL1-SRF signaling regulates the expression of a large number of genes involved in actin cytoskeleton organization and FA, we analyzed the subcellular localization of MKL1.²⁵⁷ In line with studies in *Lmna*^{-/-} MEFs and *LMNA*-mutated muscle precursors, we observed a decrease in nuclear MKL1 in LMNAkd cells.^{105,262} Hence, as postulated by Ho *et al.*¹⁰⁵ lamin A/C depletion might affect actin polymerization, through mislocalized emerin, which in turn blocks nuclear translocation of MKL1, subsequently disturbing expression of MKL1-SRF target genes.¹⁰⁵ Indeed, knockdown experiments in human mesenchymal stem cells (hMSCs) have shown that *LMNA* expression correlates with expression of SRF and its cofactors and functional emerin-lamin A/C interactions are required for cell spreading and proliferation.^{32,106} Interestingly, *FSCN1* has been identified as a putative novel SRF target gene.^{256,258} However, SRF-deficient cells show defective formation of stress fibers²⁵⁸, as opposed to LMNAkd cells. A possible explanation for this discrepancy might be elevated yes associated protein (YAP) signaling, which counteracts this effect, as observed in *LMNA*-mutated muscle precursors²⁶², or the DAP kinase pathway mentioned earlier.

To elucidate whether decreased protein levels of ACTR2 and ACTR3 contribute to impaired FA formation in LMNAkd cells, we inhibited the ARP2/3 complex with CDDO-me. ARP2/3 inhibition affected FA and induced cell detachment. This was also observed after knockdown of *ACTR3* in HeLa cells.²⁶⁰ However, it should be stressed that the effects of chemical inhibition of ARP2/3 are exaggerated, since LMNAkd cells still express ACTR2 and ACTR3. Low levels of ACTR2 and ACTR3 proteins probably affect the number of the hybrid vinculin-ARP2/3 complexes which are involved in FA formation.²⁶⁰ Next to reduced protein levels of the APR2/3 subunits, reduced paxillin expression might also contribute to impaired FA formation in LMNAkd cells, as shown in pulmonary arterial muscle cells after paxillin knockdown and in paxillin null mouse embryonic stem cells.^{277,278} In contrast, *FSCN1* knockdown has been associated with larger FAs and a higher number per cell²⁶¹, so it is likely that decreased ACTR2, ACTR3 and paxillin protein levels overrule the effect of *FSCN1* depletion on FA.

In conclusion, our data suggest that reduced *LMNA* expression influences the levels of proteins involved in actin cytoskeleton organization, in particular those of FA formation/turnover. This altered protein expression perturbs the balance between focal adhesions and cytoskeletal tension as it is accompanied by decreased FA size, reduced initial cell attachment, but increased cell migration and cytoskeletal tension. Decreased protein levels of ACTR2, ACTR3 and paxillin likely contribute to the phenotype, whereas the STAT3-IL6 axis does not. Resolving the exact pathways underlying this uncoordinated regulation may help to better understand mechanosignaling defects witnessed in certain laminopathies. Future studies should be complemented with 3D cell culture, since 3D cell migration can differ greatly from 2D cell migration, and 3D cell culture is a better approximation of an *in vivo* environment.^{279,280}

3.4. Materials and Methods

Cell culture

Normal human dermal fibroblasts (NHDF, Promocell, C-12300) were cultured in T25 or T75 culture flasks in DMEM High Glucose with L-Glutamine medium (Lonza, BE12-604F) supplemented with 10% fetal bovine serum (Gibco, Life Technologies, 10500-064) and 1% penicillin/streptomycin (Westburg, DE17-602E/12), at 37°C and 5% CO₂, according to standard procedures. All experiments were performed with cells in between passages 9 and 20. In case of direct comparison, passage-matched cells were used. Where indicated, fibroblasts were treated with 100 ng/ml human recombinant IL6 (Thermo Fisher Scientific, F10395-HNAE-25) and 200 ng/ml human recombinant IL6 receptor (IL6R) (Sigma-Aldrich, SRP3097-20UG) for 24 h.

siRNA-mediated knockdown

Expression of *LMNA* was silenced with siGENOME Lamin A/C siRNA (Dharmacon, D-001050-01-20). *STAT3* expression was silenced with ON-TARGETplus *STAT3* siRNA (Dharmacon, L-003544-00-0005). Stealth RNAi siRNA Negative Control, Med GC (Life

Technologies, 12935-300) was used as a negative non-targeting control (NTkd). siRNA transfections were performed using Lipofectamine RNAi-MAX Transfection Reagent (Life technologies, 13778-075) according to the manufacturer's instructions. A sustained knockdown was induced by two transfection rounds separated by 72 h. All measurements were carried out 168 h (1 week) after the initial transfection.

Stable isotope labeling and mass spectrometry

NHDF cells were grown in SILAC DMEM (lacking L-arginine and L-lysine, Cambridge Isotope Laboratories, DMEM-500) supplemented with 1% penicillin/streptomycin/L-glutamine (Gibco, 10378-016) and 10% dialyzed FBS (Cambridge Isotope Laboratories, FBS-50). Before knockdown, LMNAkd fibroblasts were grown in medium supplemented with [¹³C₆]-L-arginine (Cambridge Isotope Laboratories, CLM-2265-H-0.1) and [¹³C₆]-L-lysine (Cambridge Isotope Laboratories, CLM-2247-H-0.05) and control (NTkd) fibroblasts in medium supplemented with 0.47 mM L-arginine (Cambridge Isotope Laboratories, ULM-8347-0.1) and 0.46 mM L-lysine (Cambridge Isotope Laboratories, ULM-8766-0.05) for at least five passages. A labeling efficiency of 99.2% was obtained with no significant arginine to proline conversion (Suppl. Doc. S2). NTkd and LMNAkd fibroblasts (passage 17) were lysed by applying three freeze-thaw cycles and digested using trypsin. A fraction of the samples was mixed and analyzed by the Orbitrap Velos mass spectrometer, based on the results, the mixing was changed to obtain a 1:1 ratio. The peptide mixture was analyzed by a LC-MS/MS system using an Ultimate 3000 RSLC nano liquid chromatograph (Thermo Fisher Scientific, Bremen, Germany) in-line connected to a Q Exactive mass spectrometer (Thermo Fisher Scientific). Peptides were identified and quantified with MaxQuant²⁸¹, which used Mascot²⁸² as search engine. Reversed sequences and commonly observed contaminants were removed and the relative quantification ratios were normalized and log transformed using Perseus software (Computation Systems Biochemistry, Max Planck Institute of Biochemistry, München, Germany). An outlier significance score for log protein ratios (significance A) was calculated, a p-value of 0.05 was used as threshold value.²⁸¹ The SILAC experiment was conducted in triplicate, but one replicate was omitted since no significant depletion of A-type lamins was observed in that replicate. The complete dataset is provided as supplementary material (Suppl. Doc. S1), in which SILAC ratio's (log₂ fold change), posterior error probability (PEP), intensity, significance A levels, sequence coverage, peptide counts (razor and unique peptides), molecular weight (kDa), protein IDs, protein names and gene names are presented. Gene ontology of identified proteins was analyzed for protein class with the online resource PANTHER (Protein ANalysis THrough Evolutionary Relationships)²⁸³ and gene ontology enrichment analysis was performed with GOrilla (Gene Ontology enRIchment AnaLysis and VisuaLizAtion tool).²⁸⁴

Quantitative PCR

RNA was extracted from cells using the RNeasy mini kit (Qiagen, 74104), with on-column DNase digestion. Concentrations of purified RNA were measured with the NanoDrop 2000 (Thermoscientific). Per sample, 1 µg of RNA was converted to cDNA

using SuperScript® III Reverse Transcriptase (RT) (Life Technologies, 18080-044). All qPCR reactions were performed on a RotorGene 3000 (Qiagen/Corbett) using the SensiMix™ SYBR® No-ROX Kit (Bioline, QT650) according to the manufacturer's instructions. Relative abundance of *LMNA* transcripts (forward: TGGACGAGTACCAGGAGCTT; reverse: ACTCCAGTTTGCGCTTTTTG), *IL6* transcripts (forward: AGTGAGGAACAAGCCAGAGC; reverse: GTCAGGGGTGGTTATTGCAT), *IL6R* transcripts (forward: GGCACGCCTTGGACAGAATC; reverse: AAGAATCTTGCACTGGGAGGC), *STAT3* transcripts (forward: CAGGAGCATCCTGAAGCTGAC; reverse: GGTGAGGGACTCAAAGTCC), *ACTR2* transcripts (forward: GTAGCCATCCAGGCAGTTCT; reverse: AAGGCGTATCCTCGCAACAG), *ACTR3* transcripts (forward: CTGTGTGGTGGACTGTGGCA; reverse: TCAACACCTTTCATCACCTCC), *FSCN1* transcripts (forward: CCAACCGCTCCAGCTATGAC; reverse: CTGCCACCGTCCAGTATTT), *CLIC4* transcripts (forward: GAGGACAAAGAGCCCCTCATC; reverse: GGGGCAGTTTCCTATGCTTTC) and *PXN* transcripts (forward: GGAAAAGTTGCGGGGCATAG; reverse: GTGGTAGACTCCAAGTCCGC), were measured relative to *ACTB* (forward: CCTTGCACATGCCGGAG; reverse: GCACAGAGCCTCGCCTT) and *GAPDH* (forward: TGCACCACCAACTGCTTAGC; reverse: GGCATGGACTGTGGTCATGAG) reference transcripts. Analysis was done using the $\Delta\Delta C_t$ -method.²³⁵

Immunofluorescence staining

Cells were grown on glass coverslips and fixed in 4% paraformaldehyde for 15 min at room temperature and washed (3 x 5 min) with PBS. Subsequently, cells were permeabilized with 0.5% Triton X-100 (5 min), and incubated with primary antibody diluted in 50% fetal bovine serum (FBS) for 60 min. After minimally 3 PBS washing steps, slides were incubated with secondary antibody diluted in 50% FBS for 30 min and, where indicated, with rhodamine phalloidin (ThermoFisher Scientific, R415) for the labeling of F-actin. After the incubation, the slides were washed again, and mounted with VECTASHIELD™ Mounting Medium (Vector Labs, VWR, 101098-042) containing 1 µg/ml 4',6-diamino-2-phenylindole (DAPI, ThermoFisher Scientific, D1306). Primary antibodies used were directed against lamin A (Rabbit, Abcam, ab26300), paxillin (Mouse, Merck Millipore, 05-417), vinculin (Mouse, Sigma-Aldrich, V9131), FAK (Rabbit, Santa Cruz Biotechnology Inc., sc-932) and MKL1 (Rabbit, Abcam, ab49311). Secondary antibodies were DyLight 488 conjugated donkey anti-rabbit (Jackson ImmunoResearch Laboratories Inc., JAC-705606147) and DyLight 488 conjugated donkey anti-mouse (Jackson ImmunoResearch Laboratories Inc., JAC-715486150). Immunofluorescent stained cells were visualized using a Nikon Ti Eclipse inverted widefield fluorescence microscope (Nikon Instruments) with 40x Plan Apo oil (NA = 1.3) or 60x Plan Apo VC (NA = 1.4) objectives. Immunofluorescent staining was performed in triplicate, and per microscope slide a minimum of 9 regions was imaged.

Western blot

Cells were grown in T75 culture flasks and lysed using the whole-cell extraction protocol of the Nuclear Extract Kit (Active Motif, 40010). Protein concentration was measured with the Pierce 660 nm assay (Thermo Scientific, 22662). Cell lysates were subjected to SDS-PAGE (8% or 12% bis-tris with MOPS running buffer) and transferred to BioTrace PVDF membranes (Pall Corporation, 66542). Primary antibodies were directed against lamin A/C (Mouse, Santa Cruz Biotechnology Inc., sc-56139), ARP2 (Rabbit, Abcam, ab47654), ARP3 (Mouse, Abcam, ab49671), Fascin (Mouse, Abcam, ab78487), STAT3 (Cell Signaling, #9139), paxillin (Mouse, Merck Millipore, 05-417), vinculin (Mouse, Sigma-Aldrich, V9131), FAK (Rabbit, Santa Cruz Biotechnology Inc., sc-932), beta actin (Mouse, Abcam, ab8226) and nucleolin (control) (Rabbit, Novus Biologicals, NB600-241). HRP conjugated goat anti-mouse (Sigma-Aldrich, A4416) and HRP conjugated goat anti-rabbit (Sigma-Aldrich, A6154) were used as secondary antibodies. Proteins were detected by chemiluminescence with Immobilon Western chemiluminescent HRP substrate (Millipore, WBKLS0100).

Wound healing assay and cell tracking

Cells were seeded into a 24 well plate and grown up to 100% confluency. A scratch was applied using a pipette tip. The cells were washed twice with PBS to remove floating debris. To inhibit cell division, DMEM without FBS was used. Cell migration was monitored by transmission microscopy with a Nikon Ti Eclipse inverted widefield fluorescence microscope (Nikon Instruments), and cell migration rate was determined by plotting the scratch area as a function of time. By fitting a linear trend line to this plot, the slope of the curve can be estimated, and by dividing the slope by two times the length (l) of the wound (as cells are migrating of both edges of the wound towards each other) the cell migration rate was calculated.²⁸⁵

$$v_{migration} = \frac{|slope|}{2 \times l}$$

The wound healing assay was complemented with individual cell tracking; therefore, nuclei were stained with Hoechst 33342 (ThermoFisher Scientific, H3570) and time-lapse images, with a temporal resolution of 10 min, were acquired. Image analysis is described below.

Cell adhesion assay

A 96 well plate was coated with bovine collagen type I (10 μ g/ml in PBS) (VWR, 392-2502) and stored overnight at 4°C, and rinsed. Remaining protein binding sites were blocked with BSA (1% in PBS) and incubated for 30 min at room temperature and rinsed. In the meantime, cells were detached with 2 mM EDTA (in PBS) and counted. 20,000 cells per 96 well plate were seeded and incubated for 60 min at 37°C and 5% CO₂ humidified atmosphere. Coated wells without cells were used as background control. The wells were 5 times thoroughly washed with PBS and fixed with 96% ethanol for 10 min at room temperature. The cells were stained with crystal violet (0.1% in 10% ethanol) and incubated for 30 min at room temperature. The wells were

thoroughly washed with demineralized water to remove excess stain, and acetic acid (10% in demineralized water) was added and incubated for 20 min at room temperature on a shaker. Absorbance was measured at 595 nm with a spectrophotometer (Tecan Infinite 200 Pro, Männedorf, Switzerland). Cell adhesion was registered as absorbance corrected for background.

Traction force microscopy

Traction force microscopy is based on measuring the displacement of fluorescent beads embedded in polyacrylamide gels, which is triggered by cell detachment. By tracking the movement of the fluorescent beads, the displacement can be calculated, which correlates with cellular traction force.

Polyacrylamide gels (0.1% bis and 5% acrylamide; 70 μm thick) containing 1:50 volume of carboxylate-modified fluorescence latex beads (0.2 μm Fluospheres, Molecular Probes, Eugene, OR) were fabricated on 25-mm diameter glass coverslips.²⁸⁶ The Young's modulus of the gel was estimated to be 15 kPa using Dynamic Mechanical Analysis (Mettler Toledo, Switzerland). Collagen-coated PDMS stamps were allowed to react with the activated gel for 1 h at 37°C to create collagen-coated adhesive islands. After removal of the excess of collagen by washing with PBS, unprinted areas of the gels were passivated with a bovine serum albumin solution overnight. Cells (5000/ml) were seeded on the gel and incubated till they were completely spread. Fluorescence images of the gel containing fluorescent beads immediately beneath the patterned cells were taken during cell detachment with trypsin. The change of the position of the fluorescence beads were measured in MATLAB software using an algorithm described previously.²⁸⁷ This yielded the discretized displacement field between two consecutive frames. The calculated displacements were summed up to determine the overall two-dimensional displacement field. The traction field was then calculated from the displacement field by solving the inverse of the Boussinesq solution from the displacement field on the surface of an elastic half space to obtain the traction field when the mechanical properties of the gel are known. The Poisson ratio of the gel was assumed to be close to 0.5. The interior of the cell was subdivided into 64 μm^2 squares to approximate the discretized localization of contractile forces.

Image analysis

Image processing was performed in Fiji (<http://fiji.sc>), a packaged version of ImageJ freeware (W.S. Rasband, U.S.A. National Institutes of Health, Bethesda, Maryland, USA, <http://rsb.info.nih.gov/ij/>, 1997–2014).

The focal adhesion points were quantified by means of a custom-designed image processing pipeline²⁸⁸, which is essentially based on a high-content analysis workflow described before⁵⁶ and is available upon request. In brief, the analysis consists of a few image preprocessing steps, followed by hierarchical segmentation of nuclei, cells, and focal adhesion points (FAs) to allow region-specific analysis of objects. Nuclear regions of interest (ROIs) are segmented in the DAPI channel after filtering with a

Gaussian kernel of small radius ($\Sigma = 3$), automatic thresholding according to Otsu's algorithm and watershed-based separation. Cellular boundaries are then delineated by conditional region growing from the nuclear seeds restricted by a Voronoi tessellation. Finally, FAs are specifically enhanced in the FA channel by means of a Laplacian operator and binarized using the Triangle autothresholding algorithm. The Triangle algorithm was selected since this is a geometric method, resulting in a better coverage of the complete FA size. The resulting ROIs were used for analyzing shape (area and circularity) and intensity metrics of objects larger than a predefined size (>5 pixels) on the original image.

Stress fiber thickness was quantified in microscopic images of phalloidin-stained cells by applying a fast Fourier transformation, low frequency filtering, inverse transformation and Isodata autothresholding, after which fluorescence intensity and area per stress fiber was calculated per cell.

Cell mobility was determined by tracking nuclei from Hoechst 33342 counterstained individual cells through time using a dedicated script (trackRuptures.ijm; available upon request).⁶¹ In this analysis, nuclei are detected using a Laplacian of Gaussian blob detector, binarized using an automatic threshold algorithm and touching nuclei are separated using a conditional watershed algorithm. Once nuclei have been detected in all time points, they are connected through time based on a nearest neighbor algorithm, which is confined by a maximum displacement. If for a given nucleus, no corresponding neighbor is found in the next time point, potential candidates are sought in the closest subsequent time point. After, this automatic procedure, the operator can manually check and correct tracks.

Statistical analyses

Data analysis and visualization was performed in R statistical freeware (<http://www.r-project.org>). Standard statistical methods were employed, including the Shapiro-Wilk Normality Test to assess normality of the data; Levene's test to assess homoscedasticity; Student's *t*-test, ANOVA, and the Kruskal-Wallis rank sum test to assess differences between the group means; and Tukey (after ANOVA) and Dunnett type (After Kruskal-Wallis) post-hoc tests to assess significance for each group. We also used non-parametric contrast-based multiple comparison tests and Wilcoxon tests.²⁸⁹ Significance levels were indicated as follows: $p < 0.05$ (*), $p < 0.01$ (**), and $p < 0.001$ (***). For graphics and annotation, the R program was expanded with the ggplot2 package.²³⁹

4

ZMPSTE24 DEFICIENCY IMPAIRS INTRACELLULAR LIPID STORAGE AS REVEALED BY RAMAN MICROSPECTROSCOPY

Abstract

The metalloprotease ZMPSTE24 catalyzes maturation of lamin A, a key component of the nuclear lamina. Loss of ZMPSTE24 leads to premature aging disorders and severe metabolic alterations, including lipodystrophy. However, as yet, the molecular changes that accompany ZMPSTE24 deficiency at the cellular level are not completely understood. Here, we explore the potential of label-free confocal Raman microspectroscopy (RMS) to discriminate genome-edited *ZMPSTE24* knockout (ZKO) cells from non-targeting controls. Hyperspectral image data sets were collected from individual living cells at 785 nm excitation. Unsupervised classification of average cellular spectra allowed separating both cell types with high fidelity. Subsequent analysis of spectral differences revealed that ZKO cells had a decreased lipid content. Cross-correlation with fluorescent labeling revealed that this decrease was associated with a significant reduction in lipid droplet (LD) number and size in ZKO cells. Counterintuitively, this was accompanied with increased expression of several LD biogenesis genes (*GPAM*, *PEMT*, and *PGC1 α*). Thus, our data suggest that loss of *ZMPSTE24* impairs intracellular lipid storage and proves that RMS is a powerful tool for label-free interrogation of pathological cells.

4.1. Introduction

Laminopathies are diseases of the nuclear lamina. They are caused by mutations in genes encoding nuclear lamins, such as the *LMNA* gene (producing lamin A/C), or in genes involved in lamin processing, such as *ZMPSTE24*. The latter encodes the zinc metalloprotease ZMPSTE24, which is crucial for proper maturation of lamin A. Lamin A is produced as a precursor protein, prelamin A, and undergoes a sequence of posttranslational modifications at its C-terminus, including carboxymethylation, farnesylation and proteolytic cleavage. This final step is solely catalyzed by ZMPSTE24.¹⁴ Consequently, loss of ZMPSTE24 results in the accumulation of farnesylated prelamin A. Diseases that are caused by *ZMPSTE24* deficiency include mandibuloacral dysplasia type B (MADB) and restrictive dermopathy (RD).²⁻⁵ MADB is caused by partial loss of ZMPSTE24 activity, while RD is associated with complete loss.¹²⁹ MADB is characterized by skeletal abnormalities and generalized lipodystrophy, and some patients have features of premature aging.^{117,126} On the other hand, RD is a lethal neonatal genodermatosis. RD patients usually die within several hours or days of birth.^{126,127}

A vast array of omics tools has become available to study pathologies at the cellular level. However, these methods only highlight changes in selected subsets of molecules (e.g., gene and protein expression) and offer no cellular context. Raman microspectroscopy or Raman microscopy (RMS) offers an interesting tool for obtaining insight into the true molecular markup (lipids, proteins, carbohydrates ...) of the intracellular environment. By probing molecular vibrations with a laser, RMS is able to assess the chemical microenvironment of the biological sample at a submicron scale.²⁹⁰ This technique can be used to characterize and image cells in absence of

fluorescent stains.^{290,291} Since molecular changes in cells, tissues or biofluids can either cause or be the effect of diseases, RMS can be applied for medical diagnostics.^{188–191} Here we used RMS to study HeLa cells in which the *ZMPSTE24* gene was stably knocked out using CRISPR/Cas9-mediated genome editing.

4.2. Results

Stable ZKO cells accumulate prelamin A

To avoid the heterogeneity and bypass the limited availability of patient cells, we established a set of isogenic model cell lines with a stable *ZMPSTE24* knockout using targeted CRISPR/Cas9 genome editing. We further refer to these cells as HeLa-ZKO. Multiple clones were isolated and compared with control-treated, wild type HeLa cells (HeLa-WT), which underwent identical operational procedures but without the specific guide RNA. All HeLa-ZKO clones demonstrated a significant reduction of *ZMPSTE24* transcripts, as measured by qPCR analysis (Figure 4-1C), albeit with high interclonal variability. In contrast, all HeLa-ZKO clones showed a strong and comparable > 2-fold prelamin A (PLA) accumulation as compared to HeLa-WT clones, as measured by quantitative microscopy after immunofluorescence staining for PLA (Figure 4-1B & D). Western blotting confirmed a specific accumulation of PLA, and complete absence of mature lamin A in HeLa-ZKO clones, as shown by the upward shift of the lamin A band as compared to the HeLa-WT control cells (Figure 4-1A). The accumulation also affected the nuclear phenotype as evidenced by quantitative image analysis. Despite some variability between clones, knockout of *ZMPSTE24* resulted in a slightly increased nuclear area, except for clone Z6 (Figure 4-1F). The effect on nuclear dysmorphism was less pronounced, presumably because of the high basal nuclear morphology aberrations (Figure 4-1G). However, nuclear herniations and nuclear blebs were more frequently observed in HeLa-ZKO cells compared to HeLa-WT control cells (Figure 4-1D).

Unsupervised clustering of Raman spectra discriminates HeLa-ZKO cells from HeLa-WT cells

Fixed HeLa-ZKO (clone Z6) and HeLa-WT cells (clone C1) were subsequently subjected to confocal RMS. Raman spectra were collected by raster-scanning individual cells ($n \geq 50$ per cell type) with a 785 nm laser. The resulting hyperspectral image data sets were processed according to the workflow depicted in Figure 4-2 (cfr. also M&M).

First, spectral information from all cellular pixels was pooled into average cellular spectra. Hierarchical cluster analysis (HCA) of average spectra allowed separating HeLa-ZKO cells from HeLa-WT cells with an accuracy of 91.96%, a sensitivity (true positive rate) of 90.74%, and a selectivity (true negative rate) of 93.10%, with a false discovery rate (FDR) of 7.54% (Figure 4-3A). Unsupervised clustering through principal component analysis (PCA) performed worse compared to HCA. The biplot of the first two principal components (PCs) showed strong overlap between the 98%

confidence interval of the HeLa-WT cells and the 98% confidence interval of HeLa-ZKO cells (Figure 4-3B). In addition, PCA was used to reduce the data prior to the former mentioned HCA by selecting the first 3 PCs. However, this resulted in a decreased sensitivity and selectivity (data not shown).

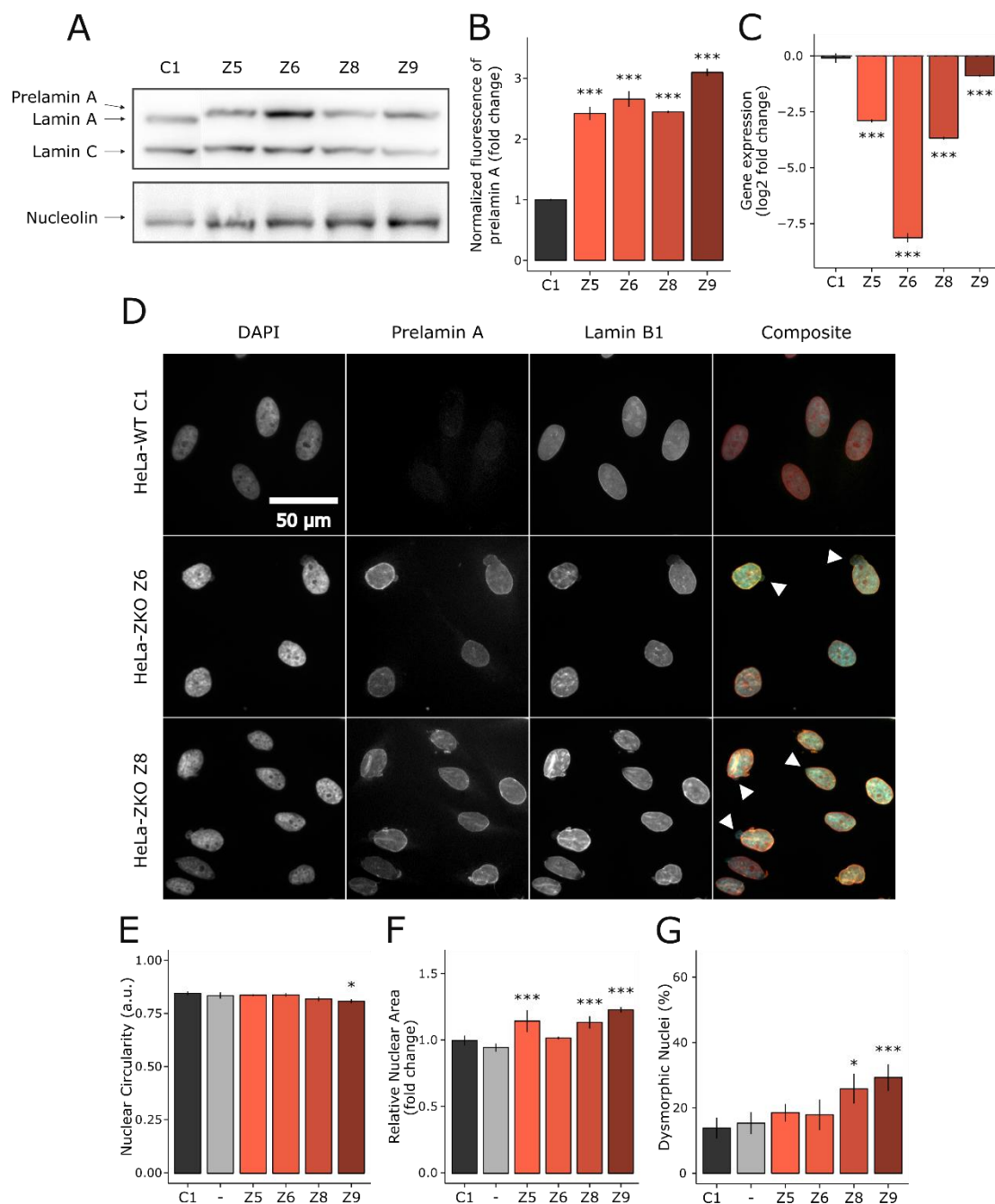


Figure 4-1. *ZMPSTE24* knockout induces prelamin A accumulation in HeLa cells. **A**: Western blot analysis of lamin A, lamin C and prelamin A in HeLa-WT (C1) and HeLa-ZKO clones (Z5, Z6, Z8, and Z9). Nucleolin was used as a loading control. **B**: Normalized mean fluorescence (fold change) of prelamin A in different HeLa-ZKO clones (Z5, Z6, Z8, and Z9) relative to HeLa-WT cells (C1). Error bars indicate the standard deviation on the mean value of three biological replicates; significance was calculated with a Student's *t*-test; *** = *p*-value < 0.001. **C**: Gene expression level of *ZMPSTE24* measured by real-time qPCR in HeLa-ZKO clones relative to HeLa-WT cells (C1). Error bars indicate the standard deviation on the mean value of three technical

replicates. Significance was calculated with a Student's *t*-test; *** = *p*-value < 0.001. D: Representative images of HeLa-WT (C1) and HeLa-ZKO (Z6 and Z8) cells after immunofluorescence staining for prelamin A (yellow), lamin B1 (red) and counterstaining with DAPI (blue). Arrowheads indicate nuclear blebs. E-G: Nuclear circularity (E), nuclear area (relative C1) (F), and the number of dysmorphic nuclei (G) were measured through analysis of microscopic images from all HeLa-WT (C1) and HeLa-ZKO clones (Z5, Z6, Z8, and Z9), untreated HeLa cells were included as an extra control (-). Error bars indicate the standard deviation on the mean value of four biological replicates; significance was calculated with ANOVA or non-parametric contrast-based multiple comparison tests; * = *p*-value < 0.05, *** = *p*-value < 0.001.

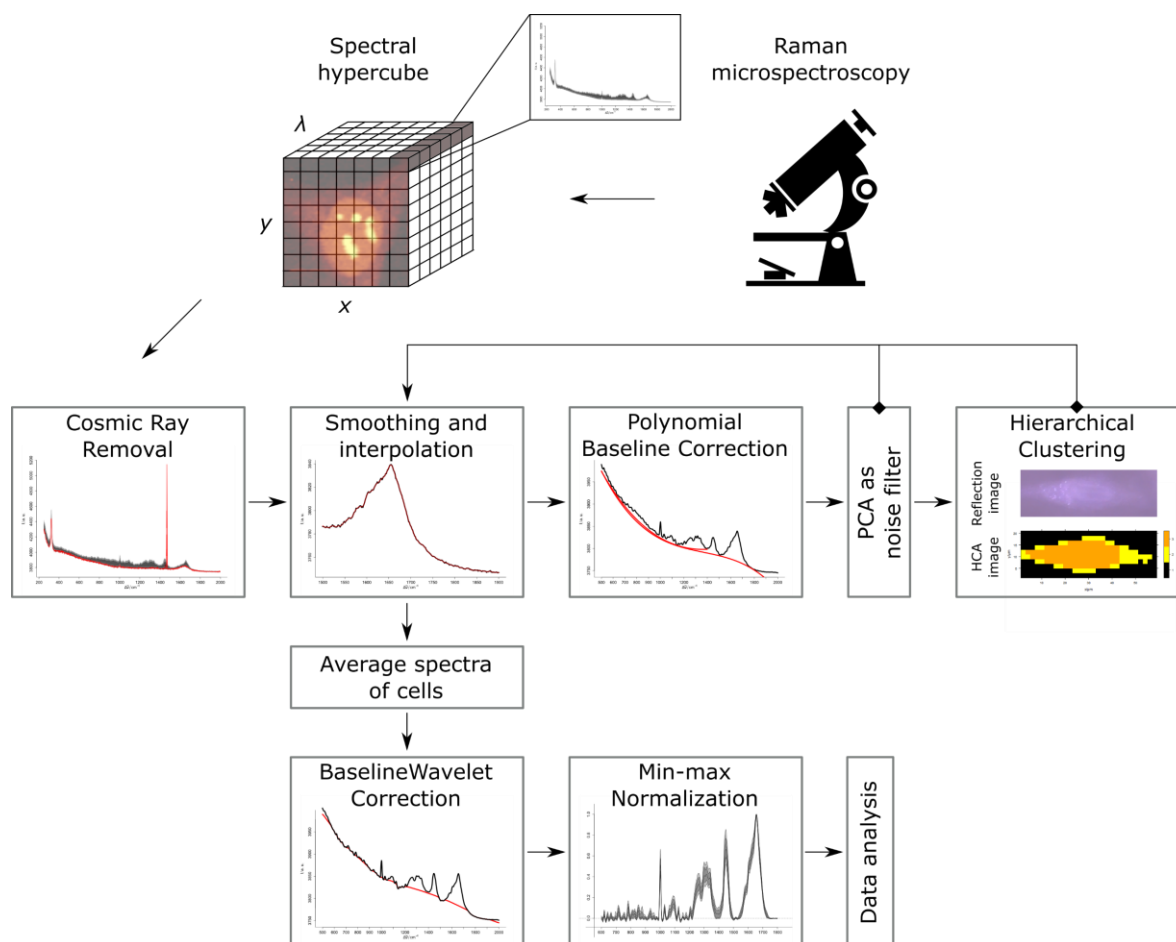


Figure 4-2. Raman spectra were collected by raster-scanning individual cells with a 785 nm laser. The spectra were preprocessed in R using the hyperSpec package.²⁹² Initial preprocessing involved cosmic ray removal and smoothing and interpolation. Cellular pixels were selected by HCA after fast polynomial baseline removal and outlier removal with PCA. The average spectrum of the cellular pixels was calculated the background was accurately removed with baselineWavelet correction. Finally, the average spectra were min-max normalized. The preprocessing is described in more detail in the M&M section.

Difference spectrum highlights changes in lipid content of HeLa-ZKO cells

To determine which spectral components contributed the most to the discriminatory power, we compared the average spectra of HeLa-ZKO and HeLa-WT cells, and generated a difference spectrum (Figure 4-3C & D). This revealed that 4 bands

deviated strongly in HeLa-ZKO cells: namely a Raman peak at 876 cm^{-1} , in close vicinity to a peak at 856 cm^{-1} , which might be attributed to hydroxyproline, a major component of collagen²⁹³; chain C-C stretching vibration at 1065 cm^{-1} ; CH_2 twisting at 1301 cm^{-1} ; and CH_2 deformation at 1439 cm^{-1} .^{291,294} The last three are typical bands for lipids. Hydroxyproline is also associated with a Raman band at 957 cm^{-1} and 1207 cm^{-1} , however no significant differences were observed at these regions. Furthermore, dermal fibroblast from patients with *LMNA* mutations show normal synthesis and mobility of type I collagen.²⁹⁵ Therefore this Raman peak was not further investigated and we focused our work on the lipid specific Raman peaks. We calculated the area of these peaks, by integrating a fitted spline, and observed a significant decrease for all three bands in HeLa-ZKO cells (Figure 4-3E-G), suggesting a significant reduction in lipid content.

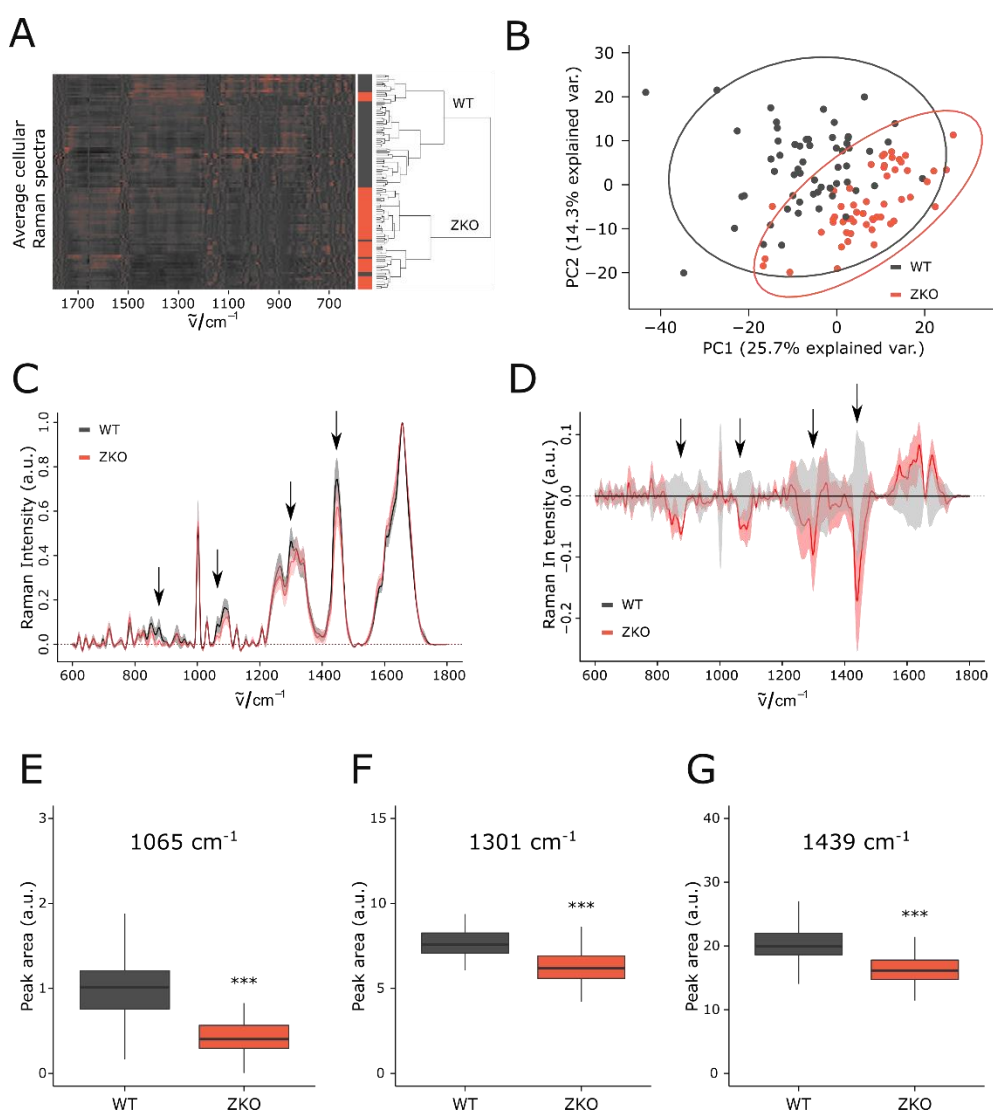


Figure 4-3. Raman spectra of HeLa-ZKO show significant changes compared to control cells. A: Heatmap of the average spectra of HeLa-ZKO (red) and HeLa-WT cells (gray), clustered by HCA. B: Biplot of the first two principal components (PCs) of HeLa-ZKO (red) and HeLa-WT cells (gray). The ellipse represents the 98% coincidence interval. C: Mean Raman spectrum of HeLa-ZKO (red) and HeLa-WT cells (gray). D: Mean difference spectrum of HeLa-ZKO (red) cells relative to HeLa-WT cells (gray). The

shaded region in C and D indicates the standard deviation on the mean value. Arrows indicate significant differences in the Raman spectra. E: Integrated area of the Raman spectra at 1065 cm^{-1} relative to HeLa-WT cells. F: Integrated area of the Raman spectra at 1301 cm^{-1} relative to HeLa-WT cells. G: Integrated area of the Raman spectra at 1439 cm^{-1} relative to HeLa-WT cells. In the boxplots, the horizontal line indicates the median, boxes the 25th and 75th percentile, and whiskers the 5th and 95th percentile. For all figures, significance was calculated with the Wilcoxon rank sum test; *** = p-value < 0.001.

HeLa-ZKO cells have less lipid droplets and lipid droplet size is decreased

We next asked whether the reduction in specific bands could also be assigned to specific regions within the cells. We found that the three major bands were strongly enriched in micron-sized cytoplasmic regions that resembled lipid droplets (LDs). Supporting this idea, the average Raman spectrum of these regions showed high similarity with the reference spectrum of triolein, a symmetrical triglyceride derived from glycerol and oleic acid (Figure 4-4B).²⁹⁴ To ascertain these regions were LDs, we performed a correlative confocal RMS-confocal fluorescence microscopy experiment in which we revisited identical cells before and after counterstaining for LDs using the fluorescent marker bodipy 493/503. To promote LD formation, cells were treated with cycloheximide prior to the recordings. Quantitative colocalization analysis between RMS images after Vertex Component Analysis (VCA) and confocal fluorescence images confirmed colocalization, thus proving that indeed these bands were characteristic for LDs (Figure 4-4A). An average Pearson correlation coefficient of 0.72 ± 0.06 was calculated for three biological replicates. More importantly, quantitative analysis of LDs in fluorescence microscopy images revealed a significant reduction in the number of LDs in HeLa-ZKO clones compared to HeLa-WT. In addition, LD size was in most clones, except clone 6 (p-value = 0.052), significantly reduced in HeLa-ZKO cells compared to HeLa-WT cells (Figure 4-4C-E).

HeLa-ZKO cells show increased expression of LD biogenesis genes

To elucidate the potential cause of the reduction in LD size in HeLa-ZKO cells, we analyzed the expression of genes involved in LD biogenesis using qPCR: acylglycerolphosphate acyltransferase (*AGPAT*); seipin (*BSCL2*); diacylglycerol O-acyltransferase 1 (*DGAT1*); fat storage inducing transmembrane protein 2 (*FITM2*); mitochondrial glycerol-3-phosphate acyltransferase (*GPAM*); phosphatidylethanolamine N-methyltransferase (*PEMT*); and peroxisome proliferator-activated receptor gamma coactivator 1-alpha (*PGC1- α*). Transcript levels of *GPAM*, *PEMT* and *PGC1- α* were significantly increased in HeLa-ZKO cells compared to HeLa-WT cells (1.77-fold, 2.06-fold and 2.07-fold increase respectively, Figure 4-4F).

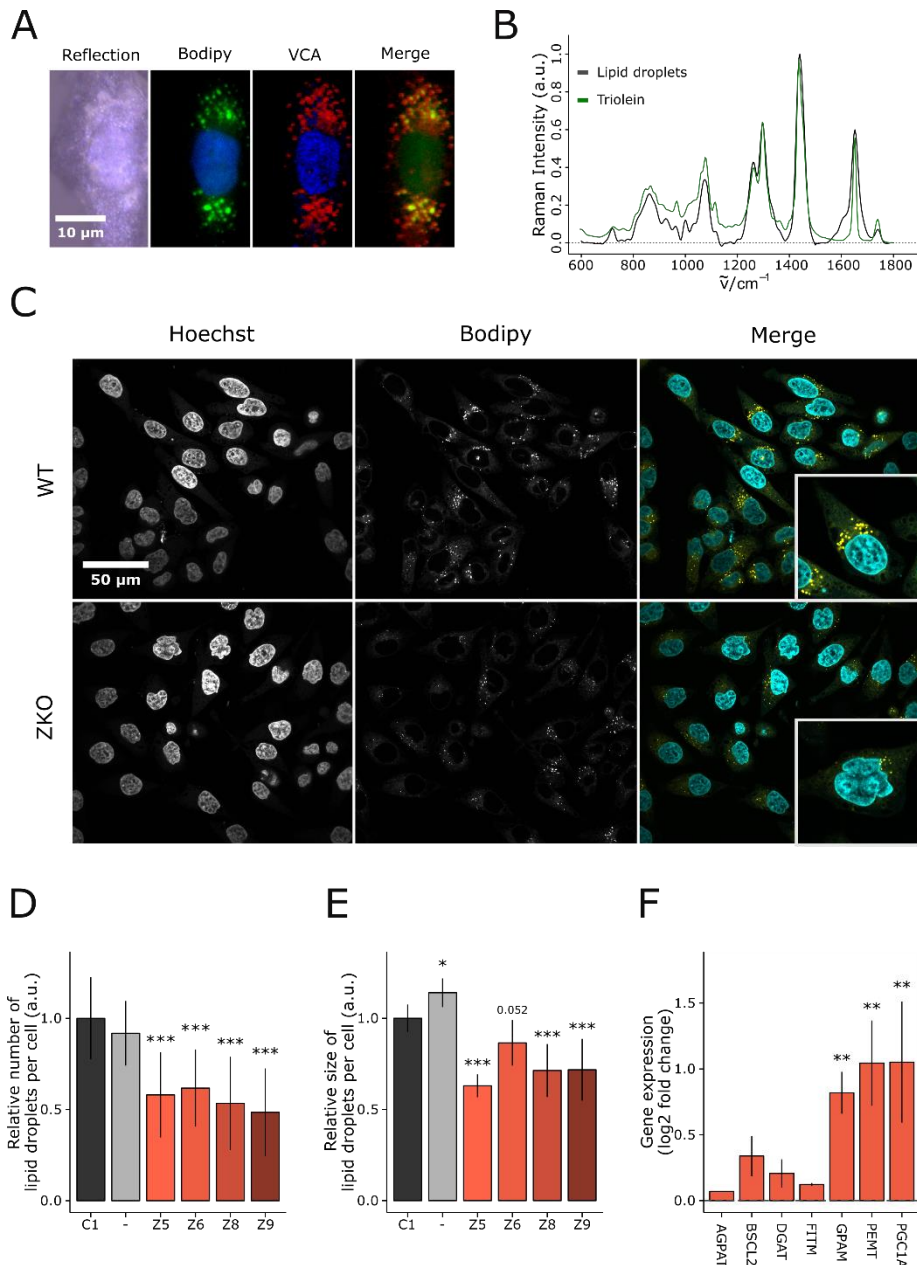


Figure 4-4. HeLa-ZKO cells have less LDs, decreased LD size and altered expression of genes involved in LD biogenesis. A: Correlation between bodipy 493/503 image (green) and VCA image (red) of a cycloheximide treated HeLa cell. On the left side, the reflection image of the cell is depicted. B: Average Raman spectrum of LDs (gray) and the reference spectrum of triolein (green). C: Representative images of HeLa-WT and HeLa-ZKO cells after bodipy 493/503 staining (yellow) and counterstaining with Hoechst 33342 (cyan). D: Number of LDs in different HeLa-ZKO clones relative to HeLa-WT cells (C1). E: Size of LDs in different HeLa-ZKO clones relative to HeLa-WT cells (C1). HeLa cells were included as an extra control (-). Error bars in D and E indicate the standard deviation on the mean value of four biological replicates. Significance was calculated with ANOVA; * = p-value < 0.05; ** = p-value < 0.01; *** = p-value < 0.001. F: Gene expression levels of *AGPAT*, *BSCL2*, *DGAT*, *FITM*, *GPAM*, *PEMT*, and *PGC1 α* measured by real-time qPCR in HeLa-ZKO cells (Z6) relative to HeLa-WT cells (C1). Error bars indicate the standard deviation on the mean value of three technical replicates. Significance was calculated with a Student's *t*-test; ** = p-value < 0.01.

4.3. Discussion

Previous studies have shown that RMS can be used to study a wide variety of diseases, but most studies focused on cancer.^{188–191} Here we used this technique to study the molecular changes in HeLa-ZKO cells, which were acquired through targeted CRISPR/Cas9 genome editing. CRISPR/Cas9 promotes genome editing by stimulating a double stranded break (DSB) at the target genomic locus which is re-ligated by error-prone nonhomologous end joining (NHEJ), leading to insertion/deletion (indel) mutations, which in turn result in frameshift mutations and premature stop codons.^{296,297} All HeLa-ZKO clones showed prelamin A accumulation, but *ZMPSTE24* expression was highly variable among the clones. Interestingly, one HeLa-ZKO clone produced a shorter lamin C isoform, as demonstrated by western blotting, this clone was excluded from the results. This might be caused by off-target effects during CRISPR/Cas9 genome editing.²⁹⁸ Several approaches have been proposed to reduce off-target effects, such as the use of a D10 mutant nickase version of Cas9 paired with two guide RNAs that each cleave only one strand, or fusion of catalytically inactive Cas9 with a Fok I nuclease domain (fCas9).²⁹⁸ Next to CRISPR/Cas9-associated off-target effects, the unstable genome of HeLa cells, which shows a remarkably high level of aneuploidy, can also contribute to high interclonal variability.²⁹⁹ The latter can be resolved by using primary cells, since these have a more stable genome. However, genome editing in primary cells is less straightforward, due to the necessity of cellular expansion after clonal selection. Therefore, iPSCs or hTERT-immortalized primary cells are the best option.

We were able to discriminate most of the HeLa-ZKO cells from HeLa-WT cells with HCA, however the FDR was higher than 5%. By increasing the sample size in future experiments, discrimination performance can be enhanced and, in parallel, supervised clustering can be used to classify the data. In the difference spectrum, we noticed four Raman bands which were significantly reduced in HeLa-ZKO cells, three bands were typical for lipids and one band was related to hydroxyproline. The lipid specific Raman bands were enriched in LDs, which was confirmed by bodipy 493/503 staining. The average Raman spectrum of LDs showed good resemblance with the reference spectrum of triolein. This triglyceride likely constitutes the neutral lipid ester core of the LDs, which is encapsulated by a surface phospholipid monolayer.^{300–302} The main function of LDs is storing lipid esters, originating from lipid synthesis or membrane lipids, in doing so they form an important defense mechanism against lipotoxicity.^{301,303–305} HeLa-ZKO cells had fewer LDs and their size was reduced compared with HeLa-WT cells. To explain this phenomenon, we analyzed the expression of a number of genes involved in LD biogenesis. *GPAM*, *PEMT* and *PGC1 α* showed increased expression. The first gene encodes a mitochondrial isoform of glycerol-3-phosphate acyltransferase (GPAT), which is involved in the synthesis of glycerolipids. GPAM specifically directs the incorporation of exogenous fatty acids into triacylglycerol.³⁰⁶ Overexpression of *GPAM* in rat hepatocytes resulted in decreased fatty acid oxidation and increased glycerolipid biosynthesis.³⁰⁷ Interestingly, in

Drosophila cells this was accompanied by the formation of many small LDs.³⁰⁸ The second gene *PEMT* is involved in the conversion of phosphatidylethanolamine (PE) to phosphatidylcholine (PC). Increased expression of *PEMT* can induce accumulation of PC, which in turn stabilizes the LD surface, resulting in smaller LDs.³⁰⁹ The third gene, *PGC1 α* , is a key regulator of mitochondrial biogenesis.³¹⁰ Similar to *GPAT* and *PEMT*, overexpression of *PGC1 α* is accompanied by the formation of smaller LDs in oleate-induced human skeletal muscle cells.³¹¹ Interestingly, both increased *PEMT* activity and increased *PGC1 α* expression has been linked to prelamin A accumulation.^{312,313} More specific, increased *PEMT* activity has been observed in prelamin A accumulating hMSC-derived adipocytes and increased expression of *PGC1 α* has been documented in the liver from *Zmpste24*-deficient mice.^{312,313} Furthermore, increased *Pgc1 α* expression has also been observed in HGPS mice.³¹⁴ Taken together the altered expression of these genes can partly explain the reduced size of LDs we observed, however in contrast to our observations increased expression of these genes normally increases lipid content. A possible explanation for this is that the overexpression of the aforementioned genes is a compensatory mechanism for accelerated lipolysis induced by prelamin A accumulation, which has been linked to loss of adipose tissue and reduced lipid storage.^{128,312,315–318} Moreover experiments in *Zmpste24*^{-/-} mice showed increased partitioning of fatty acid towards β -oxidation.¹²⁸ A possible mechanism by which prelamin A accumulation impairs lipid storage might be through interaction with the Sp1 transcription factor, perturbing adipogenesis, or sequestration of sterol regulatory element-binding protein 1 (SREBP1) which lowers PPAR γ expression, causing impairment of pre-adipocyte differentiation.^{100,242,317,319}

In conclusion, our work indicates that *ZMPSTE24*-deficiency in HeLa cells impairs lipid storage by reducing the number and size of LDs. Altered gene expression can contribute to the reduced LD size. RMS enabled us to identify molecular changes in HeLa-ZKO cells, which indicates that RMS can be a reliable technique for cell biologists. In future experiments, a larger number of cells should be included and other cell types, including patient cells, should be analyzed. In addition, nonlinear Raman technologies, such as coherent anti-Stokes-shifted Raman scattering (CARS) microscopy and stimulated Raman (SRS) microscopy, can be used instead of spontaneous RMS to reduce acquisition times and increase spatial resolution. However, a major drawback of the latter techniques is that they are often only limited to a discrete number of wavelengths. In a recent study this issue was solved by the introduction of an electronically-tunable acousto-optical filter as a wavelength selector, allowing broadband nonlinear RMS.³²⁰

4.4. Materials and Methods

Cell culture

HeLa cells were cultured in T10 or T25 culture flasks in DMEM High Glucose with L-Glutamine medium (Lonza, BE12-604F) supplemented with 10% fetal bovine serum (Gibco, Life Technologies, 10500-064) and 1% penicillin/streptomycin (Westburg,

DE17-602E/12), at 37°C and 5% CO₂, according to standard procedures. To stimulate the number of LDs we treated the cells with 10 µg/ml cycloheximide (CHX) for 24 h.

CRISPR/Cas9 mediated genome editing

To generate stable knockout HeLa cell lines for *ZMPSTE24* and controls, we used CRISPR/Cas9 genome editing. The gRNA and Cas9 protein were delivered to cells by plasmid transfection. The plasmids were constructed starting from pSpCas9(BB)-2A-Puro (PX459) (from Feng Zhang, Addgene # 48138 and 48139). The gRNA sequence which targets the first exon of *ZMPSTE24* was 5'-GGCCGAGAAGCGTATCTTCGGGG-3'. They were designed with the CRISPR oligo design tool (Feng Zhang). The constructs were made based on the protocol of Ran et al.²⁹⁶. 48 h after transfection (Lipofectamin 2000, Life Technologies, 11668027, according to manufacturer's instructions), cells were selected by culturing cells in the presence of puromycin (1 µg/ml). Control cells underwent the same treatment mentioned above but with a construct containing no gRNA. Individually selected cells were grown to colonies and screened by quantitative immunofluorescence for accumulation of prelamin A. Targeting efficiency was validated by high-resolution melt (HRM) analysis around the cut position of the Cas9 protein using the following primers for *ZMPSTE24*: forward: 5'-CTGGACGCTTTGTGGGAGAT -3', reverse: 5'-CGCTGTGCTAGGAAGGTCTC -3'.

Raman acquisition and analysis

HeLa cells were seeded onto CaF₂ slides and cultured for 24 h. The cells were fixed in 4% paraformaldehyde for 15 min at room temperature and washed (3 x 5 min) with PBS. The Raman measurements were performed in Hanks balanced salt solution (HBSS) to avoid cell detachment. Raman spectra were collected by raster-scanning the fixed cells under a confocal Raman microscope (alpha300 R, WITec, GmbH, Ulm, Germany) at 785 nm excitation with 2 µm step size and 1 s integration time per spectrum with a grating of 600 g mm⁻¹ grating and a 63X water immersion (NA = 0.95) objective. At least 50 cells per condition were measured. After data acquisition the hyperspectral datasets were preprocessed in the WITec Project Four software and in R using the hyperSpec package.²⁹² In a first step pixels containing cosmic rays were removed and replaced by the mean spectrum of four adjacent pixels, this was performed with a standard tool in the Project Four software. The corrected spectra were exported and subsequent preprocessing was carried out in R. The wavelength axis was calibrated towards the Raman signal of CaF₂ at 322 cm⁻¹, to cope with small shifts in the excitation wavelength. Next, signal-to-noise ratio (SNR) was increased by smoothing and interpolation. The spectra were smoothed by local polynomial regression fitting and in parallel interpolated on a new wavelength axis with equidistant spacing, since the unequal data point spacing can influence data analysis. The background was initially removed by fitting a polynome of the 4th order to the spectral region between 500 and 1400 cm⁻¹ and a polynome of the 3rd order to the region between 500 and 2000 cm⁻¹, since both regions could not be fitted by the same

polynome at once. The two polynomes were combined and subtracted from the spectra. After baseline correction, the data distribution was studied with principal component analysis (PCA) and outliers were removed and replaced by the average spectrum of eight adjacent pixels with an in-house written algorithm. Next, cellular pixels were detected by hierarchical cluster analysis (HCA) and the average Raman spectrum of these pixels was calculated from the original Raman spectra obtained after smoothing and interpolation. The average spectra of the cells were pooled and the background was more precisely permanently removed using the time-consuming baselineWavelet package (Zhang et al., <http://code.google.com/p/baselinelwavelet>, 2009). To estimate the baseline, peak position was accurately detected by continuous wavelet transformation (CWT), peak-width was estimated by SNR enhancing derivative calculation based on CWT, and finally the baseline was fitted using penalized least squares with binary masks. Finally, the average spectra were min-max normalized to minimize the influence of the focal volume on the signal. The minimum of each spectrum was scaled to 0 and the maximum to 1. The normalization also minimized variance between measurements. The complete preprocessing protocol is depicted in Figure 4-2.

The average cellular spectra were analyzed with HCA and PCA. A difference spectrum was generated to highlight changes by subtracting the mean Raman spectrum of control cells from the Raman spectra of *ZMPSTE24^{-/-}* cells.

LDs were isolated in Raman images by using VCA. The Raman images were preprocessed as mentioned before, but instead of polynomial baseline correction, baseline wavelet correction was applied on the whole image. Next the Raman spectra were min-max normalized and analyzed with VCA.

Immunofluorescence staining

HeLa cells were grown on glass coverslips or polystyrene 96 well plates (Greiner Bio-One, 655090) and fixed in 4% paraformaldehyde for 15 min at room temperature and washed (3 x 5 min) with PBS. Subsequently, cells were permeabilized with 0.5% Triton X-100 (5 min), and incubated with primary antibody diluted in 50% fetal bovine serum (FBS) for 60 min. After minimally 3 PBS washing steps, slides were incubated with secondary antibody diluted in 50% FBS for 30 min. After the incubation, the slides were washed again, and mounted with VECTASHIELD™ Mounting Medium (Vector Labs, VWR, 101098-042) containing 1 µg/ml 4',6-diamino-2-phenylindole (DAPI, ThermoFisher Scientific, D1306). Primary antibodies used were directed against lamin A (Rabbit, Abcam, ab26300, 1/200), lamin B1 (Abcam, ab16048, 1/1000) and prelamin A (Goat, Santa Cruz Biotechnology Inc., sc-6214, 1/150). Secondary antibodies were Alexa Fluor 488 conjugated donkey anti-rabbit (Jackson ImmunoResearch Laboratories Inc., JAC-711546152) and DyLight 649 conjugated donkey anti-goat (Jackson ImmunoResearch Laboratories Inc., JAC-705606147). Immunofluorescent stained cells were visualized using a Nikon Ti Eclipse inverted widefield fluorescence microscope (Nikon Instruments) with 40x Plan Apo oil (NA = 1.3) or 60x Plan Apo VC

(NA = 1.4) objectives. Immunofluorescent staining was performed in triplicate, and per microscope slide a minimum of 9 regions was imaged.

Bodipy 493/503 staining

HeLa cells were grown on glass, CaF₂ coverslips, or polystyrene 96 well plates and fixed in 4% paraformaldehyde for 15 min at room temperature and washed (3x, 5 min) with PBS. The cells were stained with bodipy 493/503 (1 µg/ml in PBS, ThermoFisher Scientific, D3922) and Hoechst 33342 (5 µg/ml in PBS, ThermoFisher Scientific, H3570) for 20 min at room temperature. After staining the cells were washed (3X, 5 min) and stored in PBS. Cells were visualized using a Nikon A1R confocal microscope (Nikon Instruments) or Nikon Ti Eclipse inverted widefield fluorescence microscope (Nikon Instruments) with a 60x Plan Apo VC oil (NA = 1.4) objective or a 40x Plan Fluor dry (NA = 0.75) objective.

Western blot

Cells were grown in T75 culture flasks and lysed using the Nucleospin Triprep Kit (Macherey-Nagel, 740966.50). Protein concentration was measured with the Pierce™ BCA Protein Assay Kit (Thermo Scientific, 23227). Cell lysates were subjected to SDS-PAGE (NuPAGE™ Novex™ 4–12% Bis-Tris Protein Gels with MOPS running buffer, Thermo Scientific, J00047) and transferred to BioTrace PVDF membranes (Pall Corporation, 66542). Primary antibodies were directed against lamin A/C (Mouse, Santa Cruz Biotechnology Inc., sc-56139) and nucleolin (Rabbit, Novus Biologicals, NB600-241). HRP conjugated goat anti-mouse (Sigma-Aldrich, A4416) and HRP conjugated goat anti-rabbit (Sigma-Aldrich, A6154) were used as secondary antibodies. Proteins were detected by chemiluminescence with Immobilon Western chemiluminescent HRP substrate (Millipore, WBKLS0100).

Quantitative PCR

RNA was extracted using the Nucleospin Triprep kit (Macherey-Nagel). After quality control with the Bioanalyser (Agilent), cDNA synthesis was executed (Tetro cDNA synthesis kit, Bioline) followed by qPCR (Sensimix, Bioline, CFX connect Biorad). Primers were used for *AGPAT*: forward: 5'-CAGAGCTGGGACGTCATCTG-3', reverse: 5'-TACTGCAAGAAGGAGCGTCG-3'; *BSCL2*: forward: 5'-CCTATGAAGGCGCAGGTCAT-3', reverse: 5'-CGACCACTGGAGCGATCATT-3'; *DGAT1*: forward: 5'-TGCTGAAGCCACTGTCAGAG-3', reverse: 5'-CCCCAACAAAGGACGGAGAC-3'; *FITM2*: forward: 5'-GGCAGAAGGAGACAGAACGT-3', reverse: 5'-TCAAGGAGTTGTCCCCGTTG-3'; *GPAM*: forward: 5'-ACAAAGATGGCAGCAGAGCT-3', reverse: 5'-TGACTTTGGGGAGGAACAGC-3'; *PEMT*: forward: 5'-GCCACTATGTAGGTGAGGGC-3', reverse: 5'-ATGTACTGGGGAAGCACAGC-3'; *PGC1-α*: forward: 5'-GGTGAAGCAGGGTCAAAGT-3', reverse: 5'-CTTTGCGCAGGTCAAACGAA-3'; *ZMPSTE24*: forward: 5'-CGAGAAGCGTATCTTCGGGG-3', reverse: 5'-TGTGCTAGGAAGGTCTCCCA-3'; *ACTB*: forward: 5'-CCTTGACATGCCGGAG-3', reverse: 5'-

GCACAGAGCCTCGCCTT-3'; *GAPDH*: forward: 5'-TGCACCACCAACTGCTTAGC-3', reverse: 5'-GGCATGGACTGTGGTCATGAG-3'.

Image analysis

Image Processing. Image processing was performed in Fiji (<http://fiji.sc>), a packaged version of ImageJ freeware (W.S. Rasband, U.S.A. National Institutes of Health, Bethesda, Maryland, USA, <http://rsb.info.nih.gov/ij/>, 1997–2014).

The LDs were quantified by means of a custom-designed image processing pipeline²⁸⁸, which is essentially based on a high-content analysis workflow described before⁵⁶ and is available upon request. In brief, the analysis consists of a few image preprocessing steps, followed by hierarchical segmentation of nuclei, cells, and LDs to allow region-specific analysis of objects. Nuclear regions of interest (ROIs) are segmented in the DAPI channel after filtering with a Gaussian kernel of small radius ($\Sigma = 3$), automatic thresholding according to Otsu's algorithm and watershed-based separation. Cellular boundaries are then delineated by conditional region growing from the nuclear seeds restricted by a Voronoi tessellation. Finally, LDs are specifically enhanced in the LD channel by means of a Laplacian operator and binarized using the Triangle autothresholding algorithm. The resulting ROIs were used for analyzing shape (area and circularity) and intensity metrics of objects larger than a predefined size (>5 pixels) on the original image.

Statistical analyses

Data analysis and visualization was performed in R statistical freeware (<http://www.r-project.org>). Standard statistical methods were employed, including the Shapiro-Wilk Normality Test to assess normality of the data; Levene's test to assess homoscedasticity; Student's *t*-test, ANOVA, and the Kruskal-Wallis rank sum test to assess differences between the group means; and Tukey (after ANOVA) and Dunnett type (After Kruskal-Wallis) post-hoc tests to assess significance for each group. We also used non-parametric contrast-based multiple comparison tests and Wilcoxon tests.²⁸⁹ Significance levels were indicated as follows: $p < 0.05$ (*), $p < 0.01$ (**), and $p < 0.001$ (***). For graphics and annotation, the R program was expanded with the ggplot2 package.²³⁹

5

GENERAL DISCUSSION AND PERSPECTIVES

Mimicking lamin dysfunction in cells

During the course of this PhD, we have identified different cellular pathways that are regulated by A-type lamins. To do so, we have optimized experimental perturbations that enable studying lamin A/C maturation defects in an isogenic context: namely through sustained siRNA-mediated knockdown (Ch. 2 and Ch.3) or CRISPR-Cas9-mediated knockout (Ch. 4) of *LMNA* or *ZMPSTE24*. The rationale for developing human model cells was given shape by the fact that animal model cells are more difficult to translate.^{196,197} For example, the average rate of successful translation from animal models to clinical cancer trials is less than 8%.¹⁹⁷ However, it should be noted that animal models are essential as a bridge between *in vitro* and clinical studies. Furthermore, patient cells are scarce, and have a heterogeneous genetic background.¹⁹⁵ In contrast, isogenic cell lines only differ (by definition) in the expression of the target gene (i.e. *LMNA* or *ZMPSTE24*). This facilitates interpretation of experimental data. However, patient cells remain indispensable as reference, and were therefore used during our experiments to validate our models. Ideally three different isogenic cell lines should be developed. This would strengthen our findings even further and improve their credibility.

In contrast with CRISPR/Cas9-mediated knockout, siRNA-mediated knockdown is transient. We prolonged the effect through repetitive transfection rounds, resulting in a sustained knockdown. Indeed, knockdown efficiency was strongly time-dependent, especially at the protein level. This is most likely caused by the slow turnover of lamin A.²¹⁰ Despite this lag time, siRNA transfections bear the advantage that they are easily applicable, effective and can be used on a wide range of cell types, including primary cells. CRISPR/Cas9-mediated genome editing enables the generation of stable knockout cells, but also allows the introduction of point mutations.³²¹ Unlike siRNA transfections, genome editing is more laborious and time-consuming. Especially clonal selection is a bottleneck and clonal expansion requires numerous cell divisions. Therefore CRISPR/Cas9 is difficult to apply to primary (mortal) cells. A way to circumvent this problem is by using (conditionally) immortalized primary cells, e.g. through ectopic hTERT expression, or by using iPSCs. In addition, iPSCs can be differentiated into multiple cell types, favouring their use. These cells have been generated from HGPS fibroblasts and were nearly indistinguishable from control cells, while differentiation into the affected cell lineages recapitulated the disease phenotype.^{322,323}

Sustained knockdowns induced overt changes in nuclear morphology of fibroblasts, which resembled the changes of laminopathy patient fibroblast nuclei. Nuclei from genome-edited HeLa cells showed less pronounced morphological alterations, although *ZMPSTE24* knockout cells did more frequently present nuclear herniations and blebs. This may be explained by the sheer fact that HeLa cells display a high basal nuclear morphology by default, making these cells less reliable for morphological analysis.

Both siRNA-mediated knockdown and CRISPR/Cas9-mediated genome engineering hold the risk to induced off-target effects. Off-target effects linked to siRNA transfections include non-specific induction of inflammatory cytokines and type I interferon by cellular sensors of foreign RNA (e.g. MDA5, RIG-I, PKR, OAS1-3, TLR3, TLR7 and TLR8) which can obscure on-target effects.^{324,325} Altered *IL6* expression for example can be a sequence-independent off-target effect through activation of TLR3, TLR7, and TLR8.³²⁶ Hence, the altered *IL6* expression in LMNAkd and ZMPSTE24kd cells, might be caused by off-target effects. CRISPR-Cas9-associated off-target effects are caused by mismatches between the guide RNA and the DNA, resulting in off-target cleavage activity.²⁹⁸ In line with this, one HeLa-ZKO clone showed a dramatic deviation in phenotype, as compared to the other colonies, although this can also be caused by genome instability in HeLa cells. Several modifications of this technique have been proposed to decrease the probability of these off-target effects, as discussed in chapter 4. Such as the paired nicking strategy, or fusion of catalytically inactive Cas9 with a Fok I nuclease domain (fCas9), which has a much higher specificity than wild-type Cas9.²⁹⁸ Next to these suggestions, the use of inducible CRISPR/Cas9 could dramatically decrease off-target effects with a pulse exposure of the genome to the Cas9/sgRNA complex.³²⁷

Lamins are important regulators of cellular redox biology

As described in chapter 2, *LMNA* deficiency caused elevated basal ROS levels and hypersensitivity to exogenous TBHP (induced ROS). *ZMPSTE24* deficiency on the other hand was associated with moderately increased basal ROS levels. Both knockdowns were accompanied by an upregulation of several ROS detoxifying enzymes. The hypersensitivity towards exogenous ROS in LMNAkd cells, supports the hypothesis that the nuclear lamina acts as an intracellular ROS-sink by virtue of their conserved cysteine residues within the lamin tail.²¹³ This ROS buffering capacity has also been documented in R439C skin fibroblasts, which express lamin A with an additional cysteine residue.³²⁸ Hence, loss of A-type lamins (and their cysteine residues), abrogates the ability of the lamina to act as a ROS buffering system, rendering the cell more sensitive against increases of the intracellular ROS levels. Next to loss of this ROS buffering system, *LMNA* deficient cells present repetitive nuclear ruptures, which can temporarily relocate various transcription factors, several of which controlling oxidative stress response⁶², and result in cytoplasmic translocation of nuclear PML bodies⁶⁰, known sensors of oxidative stress and regulators of redox homeostasis.^{224,225} In contrast to LMNAkd cells, ZMPSTE24kd cells are not hypersensitive to exogenous TBHP, in part due to the ROS buffering capacities of prelamin A.

Mitochondria are the instigators of oxidative stress

Loss of ROS buffering can aggravate the release of intracellular ROS and thereby boost basal ROS levels. However, this is only the case in presence of ROS build up in the cell. As dysfunctional mitochondria can trigger intracellular ROS release, we analyzed $\Delta\Psi_m$, mitochondrial $\bullet\text{O}_2^-$ levels, and basal mitochondrial respiration rate. In

LMNAkd cells we noticed that elevated ROS levels were preceded by $\Delta\psi_m$ depolarization, eventually followed by $\Delta\psi_m$ hyperpolarization, which was accompanied by increased mitochondrial $\bullet\text{O}_2^-$ levels. Furthermore, we measured a lowered basal mitochondrial respiration rate. In contrast, ZMPSTE24kd cells showed a transient $\Delta\psi_m$ depolarization and no increased mitochondrial $\bullet\text{O}_2^-$ levels were measured, which was likely due to upregulation of *SOD2*. Although, basal mitochondrial respiration was also lowered. Of note, we have also performed a SILAC-based differential proteome analysis on ZMPSTE24kd cells (unpublished data). GO analysis of these data indicated altered levels of proteins involved in ion transmembrane transport and mitochondrial membrane components. More specifically, TOMM70A, a translocase of the outer mitochondrial membrane, showed reduced protein levels and STOML2, a protein involved in mitochondrial biogenesis and function³²⁹, showed decreased gene expression (unpublished results). In line with this, proteomic profiling of adipose tissue of *Zmpste24*^{-/-} mice highlighted major changes in mitochondrial function.¹²⁸ This further supports the notion that ZMPSTE24kd impairs mitochondrial function.

Proteasome overload can trigger mitochondrial dysfunction

In LMNAkd cells mitochondrial dysfunction preceded elevated ROS levels, indicating that mitochondria are likely the initial sites of oxidative damage and the instigators of oxidative stress in the cytosol. Maharjan et al. (2014) showed that mitochondrial dysfunction can be triggered by proteasome overload, as demonstrated by accumulation of polyubiquitinated proteins in mitochondria upon proteasome inhibition, resulting in loss of $\Delta\psi_m$ and the generation of ROS from the electron transport chain (ETC).²¹⁷ Loss of A-type lamins can cause proteasome overload by the accumulation of nuclear envelope proteins (SUN2, Emerin and Nesprin-1) in the ER.^{114,218,219} In addition, loss of A-type lamins can trigger an upregulation of various ubiquitin ligases.²²⁰ The proteasome hypothesis is supported by the fact that MG132 treatment, a potent proteasome inhibitor, also resulted in a significant increase of basal and induced ROS levels, as well as increased $\Delta\psi_m$. In line with this, our research group recently measured reduced activity of the 20S proteasome in LMNAkd cells, as well as a significant decrease in the number of autophagosomes in these cells (Sieprath, T. (2017). *Exploring the role of lamins as mediators of oxidative stress* (Unpublished doctoral dissertation)). Supporting this, *Lmna*^{H222P/H222P} mice (a mouse model for LMNA cardiomyopathy) responded well to Temsirolimus, a rapamycin analogue, that activates autophagy.³³⁰ ZMPSTE24kd also impaired 20S proteasome activity, likely triggered by prelamin A accumulation, but did not significantly affect autophagy (Sieprath, T. (2017). *Exploring the role of lamins as mediators of oxidative stress* (Unpublished doctoral dissertation)). So, in ZMPSTE24kd cells, accumulation of polyubiquitinated proteins in mitochondria can be avoided by autophagy, or dysfunctional mitochondria can be cleared through mitophagy, explaining the moderately increased basal ROS levels. Moreover, our research group tested sulforaphane, a plant-derived isothiocyanate (1-isothiocyanato-4-methylsulfinylbutane), which has been shown to enhance progerin clearance in HGPS

fibroblast, via proteasome and autophagy activation.¹⁵⁹ Indeed, 20S proteasomal activity and the number of autophagosomes increased in LMNAkd and ZMPSTE24kd cells, and this was accompanied by decreased basal ROS levels (Sieprath, T. (2017). *Exploring the role of lamins as mediators of oxidative stress* (Unpublished doctoral dissertation)).

ROS dosage induces different cell fates

In contrast to LMNAkd, which induced apoptosis, reduced expression of *ZMPSTE24* triggered a senescence pathway. We hypothesize that a ROS dosage effect dictates the dichotomy in cellular outcomes. Modestly increased levels of intracellular ROS induce and maintain cellular senescence, as observed in ZMPSTE24kd cells, while higher doses provoke apoptosis, as seen in LMNAkd cells.^{231–234} However, LMNAkd cells also present decreased protein levels of paxillin and a decrease in nuclear FAK, which can also contribute to the onset of apoptosis^{264,277,331,332}. Next to their direct contribution to the onset of apoptosis, they can also impair adhesion-dependent cell cycle progression.³³³ Nevertheless, decreasing the basal ROS level might postpone senescence and apoptosis in LMNAkd and ZMPSTE24kd cells or trigger senescence instead of apoptosis in LMNAkd cells.

ROS levels can be reduced by the ROS scavenger N-acetyl cysteine as shown by Pekovic et al. (2011) in HGPS fibroblasts and *LMNA* deficient fibroblasts²¹³, or by sulforaphane treatment, as mentioned earlier. Alternatively, ROS levels can be reduced through restoring or boosting mitochondrial function. One way to do this, might be by targeting the phosphorylation of Rac1b by rho-associated protein kinase (ROCK): ROCK inhibitors have been found to block the interaction of Rac1b and cytochrome c in mitochondria, and thereby reduce ROS levels and recover mitochondrial function in HGPS fibroblasts.³³⁴ Next to ROCK inhibitors the mitochondrial-targeting antioxidant methylene blue (MB) is also very promising. MB alleviated the mitochondrial defects and rescued nuclear abnormalities in HGPS fibroblasts.³³⁵ Figure 5-1 depicts the mechanisms contributing to the cell fate of LMNAkd and ZMPSTE24kd cells.

Loss of lamins uncouples intracellular mechanical wiring

A differential proteomics analysis, revealed that sustained depletion of A-type lamins also affected the production of proteins involved in FA formation. Since nuclear translocation of MKL1 was significantly reduced, we hypothesized that impaired MKL1-SRF signaling, which regulates the expression of a large number of genes involved in actin cytoskeleton organization and FA²⁵⁷, was responsible for smaller FA size in LMNAkd cells. Emerin stimulates MKL1-SRF-dependent gene activity in a substrate-stiffness-dependent manner³³⁶, and ectopic expression of emerin can restore nuclear translocation of MKL1 in *Lmna*^{-/-} MEFs.¹⁰⁵ Hence, since correct localization of emerin depends on lamin A, impaired MKL1-SRF signaling in LMNAkd cells could likely be a result of mislocalized emerin.³³⁷ In future experiments the impact of impaired MKL1-

SRF signalling on production of FA proteins should be studied through knockdown experiments. Furthermore, activation of SRF should recover FA size in LMNAkd cells.

Interestingly, LMNAkd cells presented more pronounced stress fibers and significantly higher traction forces during cell detachment. Counterintuitively, the actin stress fibers still attached to and exerted even stronger traction forces on smaller FAs. Thus, LMNA knockdown appeared to uncouple cell adhesive mechanisms and cytoskeletal tension. A similar observation was made previously for DAP kinase, which stabilizes and enhances the formation of stress fibers through phosphorylation of TPM1, independent of FA formation, before the onset of apoptosis.²⁶⁹ Intriguingly, DAP kinase becomes activated in response to oxidative stress.²⁷⁰ This may imply that there is a direct connection between redox biology and cytoskeletal function, which is regulated by A-type lamins. To establish the involvement of DAP kinase, future experiments should focus on studying the abundance and activity of DAP kinase in LMNAkd cells vs WT controls. If DAP kinase were a downstream target of elevated ROS levels, treatment with antioxidants or knockdown of DAP kinase in LMNAkd cells should counteract the uncoupling and might prevent the onset of apoptosis.²⁶⁹ Cytoskeletal tension can also be decreased in LMNAkd cells by the aforementioned ROCK inhibition, since ROCK is involved in actomyosin contraction. Indeed treatment of immortalized human trabecular meshwork cells with ROCK inhibitors showed a loss of stress fibers.³³⁸ Thus ROCK inhibitors might not only alleviate mitochondrial dysfunction in LMNAkd cells, but also decrease cytoskeletal tension.

Taken together, we hypothesize that pathogenesis in LMNAkd cells is caused by proteasome overload (as shown by decreased 20S proteasome activity), which causes mitochondrial dysfunction, resulting in elevated ROS levels. In parallel, FA size is reduced by impaired MKL1-SRF signaling. Elevated ROS levels might activate DAP kinase, resulting in increased cytoskeletal tension independent of FA size, as shown in previous studies.^{269,270} The aforementioned events eventually result in the onset of apoptosis. So, we can distinguish two key pathways in LMNAkd cells, namely impaired MKL1-SRF signalling and elevated ROS levels, probably as a result of proteasome overload. The proposed mechanism is displayed in Figure 5-1.

Loss of ZMPSTE24 alters lipid metabolism

Loss of *ZMPSTE24* expression in HeLa cells was associated with reduced lipid storage in HeLa cells, as demonstrated by reduced LD number and size. Furthermore, increased expression of three LD-associated genes was observed, namely *GPAM*, *PEMT* and *PGC1 α* . In line with our observations, increased expression of these genes induce reduced LD size.^{308,309,311} On the other hand, these genes are involved in processes which can increase lipid storage. In addition, SILAC results of ZMPSTEkd fibroblasts showed an upregulation of ATP citrate lyase (*ACLY*), which is a lipogenic gene. We proposed that the overexpression of the aforementioned genes is a compensatory mechanism against the accelerated lipolysis induced by prelamin A accumulation, as was hypothesized by Sánchez et al. (2015) for increased *PEMT* activity in prelamin A accumulating hMSC-derived adipocytes.³¹² Indeed, experiments

in *Zmpste24*^{-/-} mice showed increased partitioning of fatty acids towards β -oxidation and away from storage¹²⁸, and LDs supply fatty acids for mitochondrial β -oxidation.³³⁹ This hypothesis can be tested by coupling stimulated Raman scattering (SRS) microscopy with isotope labeled glucose.³⁴⁰ Using this approach *de novo* lipogenesis can be visualized in real time, and the turnover of newly synthesized lipids can be assessed. Furthermore, SRS microscopy has much faster acquisition times than RMS, enabling the generation of Raman images with a high resolution.

Next to increased β -oxidation, interaction of prelamin A with Sp1 has been shown to perturb adipogenesis and sequestration of SREBP1 by prelamin A impairs pre-adipocyte differentiation.^{100,242,317,319} Since these processes implicate activation of LD biogenesis, interaction/sequestration of these transcription factors can impair lipid storage.

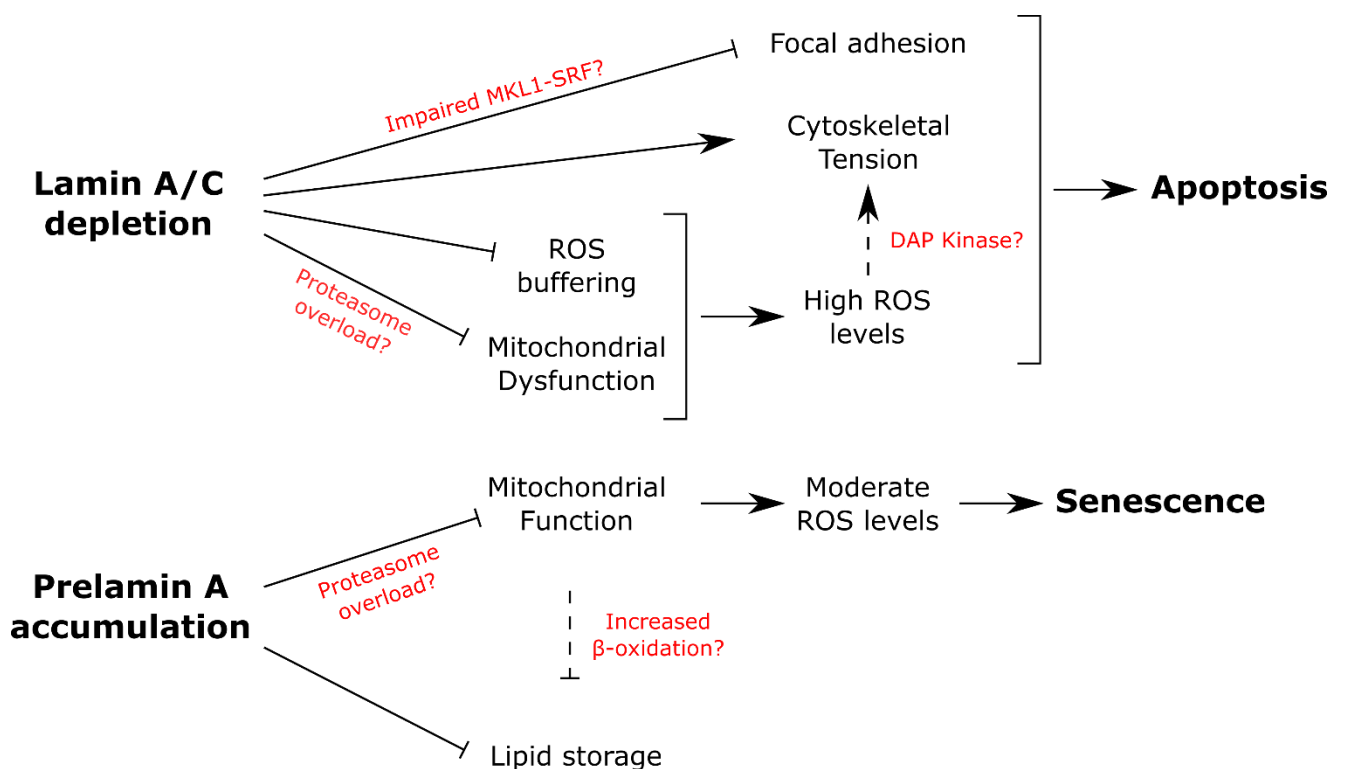


Figure 5-1. Scheme showing how loss of lamin A/C and accumulation of prelamin A eventually result in apoptosis and senescence, respectively.

Towards physiologically relevant model systems

The primary function of nuclear lamins is to regulate nuclear mechanics. However, by organizing chromatin and sequestering transcription factors, lamins also regulate a plethora of signaling pathways. Yet, knowledge about the pathogenic mechanisms that underlie laminopathies is incomplete. Using a variety of cytomics approaches, we have identified a set of additional pathways that are regulated by A-type lamins. In short, we have discovered that A-type lamins are essential for cellular redox balance, focal adhesion formation and cytoskeletal tension, and lipid droplet formation. This underlines the pleiotropic nature of lamin function and may also provide a novel basis for better understanding disease development.

For all our experiments, we either used human dermal fibroblasts or HeLa cells. However, in the context of laminopathies more relevant cell lineages should be selected. Results obtained from LMNAkd fibroblasts should be validated in cardiomyocytes or myoblasts.^{107,262,341} Results obtained from ZMPSTE24kd fibroblasts and HeLa-ZKO cells should be validated in preadipocytes and adipocytes.¹²⁸ However, these cell lineages have different genetic background. This can be bypassed through the use of hMSCs or generation of iPSCs. These stem cells can be differentiated into multiple cell lineages with the same genetic background.

A significant drawback of working with cells is the fact that they do not completely mimic the functions of living tissues. Cells within a tissue establish a 3D communication network through cell-cell and cell-extracellular matrix (ECM) interactions.³⁴² This 3D communication network can be approximated with 3D cell culture models such as organotypic explant culture, which can be retrieved from surgeries³⁴³, cellular spheroids, polarized epithelial cell cultures, artificial skin, and microcarrier culture.³⁴² When studying cell migration and cell adhesion, as discussed in chapter 3, 3D cell culture is a better reflection of the *in vivo* situation and eventually can give different outcomes compared to 2D cell culture. This has been demonstrated for *Imna*-deficient MEFs, which showed a significantly reduced migration rate in a 3D matrix, while no significant changes were observed on a 2D substrate.²⁷⁹ Similarly, cell adhesion is remarkably different in a 3D matrix than on a 2D substrate. FA proteins do not form aggregates in a 3D matrix. However they do modulate cell motility, but rather by affecting protrusion activity and matrix deformation.³⁴⁴ To even better approximate tissue biology, 3D culture models should comprise different cell types. Besides organotypic explant culture, iPSCs can be used to engineer organoids with mixed cell types.

Novel therapeutic and diagnostic strategies

Our findings can pave the way to novel therapeutic strategies for laminopathies. Especially the proteasome hypothesis is very promising, exemplified by the positive effect of sulforaphane treatment on our model cells and HGPS fibroblasts. Future studies should validate these results, prior to animal and clinical studies. Besides sulforaphane, treatments restoring mitochondrial dysfunction might also be successful. To this end, ROCK inhibitors and methylene blue can be used. Finally, antioxidants, such as N-acetyl cysteine, can also show some effect by reducing ROS levels. However, these will probably lack effectivity as monotherapy, and are therefore preferred in combination with one of the former drugs. Despite the potential of these therapeutic strategies, a lifelong administration is required, in contrast to gene therapies.

Restoring the cytoskeletal tension and FA formation is less straightforward than the preceding therapeutic strategies, and our findings should first be validated in animal studies. Instead of a novel therapeutic strategy, these observations might be relevant for early diagnosis of *LMNA* DCM, which manifests at a later age. Cytoskeletal alterations or impaired FA formation might already be present before the first

symptoms appear. However, DNA sequencing has become the most obvious and preferred diagnostic platform for genetic diseases, making it very hard to compete with. In line with this, implementation of RMS as a novel diagnostic strategy for laminopathies is also not very likely in the near future.

Main results and perspectives

1. Sustained knockdown and CRISPR/CAS9-mediated genome editing are complementary tools to modulate lamin levels
2. Lamins are important regulators of cellular redox biology.
3. Sustained lamin A/C depletion and to a lower extent prelamin A accumulation trigger oxidative stress and mitochondrial dysfunction.
4. ROS dosage contributes to the different cell fates of lamin A/C and ZMPSTE24 depleted cells.
5. SILAC-based proteomics offers a holistic insight in differentially modulated proteins between cells.
6. Loss of lamin A/C uncouples FA formation and cytoskeletal tension.
7. Loss of ZMPSTE24 decreases lipid storage.
8. Raman microscopy allows molecular fingerprinting of model cells, but with limited resolution and sensitivity

REFERENCES

1. Hetzer MW. The nuclear envelope. *Cold Spring Harb Perspect Biol* 2010; 2:1–16.
2. Wolfner MF, Wilson KL. The nuclear envelope: emerging roles in development and disease. *Cell Mol Life Sci C* 2001; 58:1737–40.
3. Pavelka M, Roth J. Nuclear Envelope and Rough Endoplasmic Reticulum [Internet]. In: *Functional Ultrastructure: Atlas of Tissue Biology and Pathology*. Vienna: Springer Vienna; 2010. page 30–1.
4. Sosa BA, Rothballer A, Kutay U, Schwartz TU. LINC complexes form by binding of three KASH peptides to domain interfaces of trimeric SUN proteins. *Cell* 2012; 149:1035–47.
5. Lim RYH, Fahrenkrog B. The nuclear pore complex up close. *Curr Opin Cell Biol* 2006; 18:342–7.
6. Alber F, Dokudovskaya S, Veenhoff LM, Zhang W, Kipper J, Devos D, Suprpto A, Karni-Schmidt O, Williams R, Chait BT, et al. The molecular architecture of the nuclear pore complex. *Nature* 2007; 450:695–701.
7. Gerace L, Huber MD. Nuclear lamina at the crossroads of the cytoplasm and nucleus. *J Struct Biol* 2012; 177:24–31.
8. Zwerger M, Medalia O. From lamins to lamina: a structural perspective. *Histochem Cell Biol* 2013; 140:3–12.
9. Shumaker DK, Kuczmarski ER, Goldman RD. The nucleoskeleton: Lamins and actin are major players in essential nuclear functions. *Curr Opin Cell Biol* 2003; 15:358–66.
10. Turgay Y, Eibauer M, Goldman AE, Shimi T, Khayat M, Ben-Harush K, Dubrovsky-Gaupp A, Sapra KT, Goldman RD, Medalia O. The molecular architecture of lamins in somatic cells. *Nature* 2017; 543:261–4.
11. Höger TH, Grund C, Franke WW, Krohne G. Immunolocalization of lamins in the thick nuclear lamina of human synovial cells. *Eur J Cell Biol* 1991; 54:150–156.
12. Goldman AE, Maul G, Steinert PM, Yang HY, Goldman RD. Keratin-like proteins that coisolate with intermediate filaments of BHK-21 cells are nuclear lamins. *Proc Natl Acad Sci* 1986; 83:3839–43.
13. Gruenbaum Y, Medalia O. Lamins: the structure and protein complexes. *Curr Opin Cell Biol* 2015; 32:7–12.
14. Broers JL, Ramaekers FC, Bonne G, Yaou RB, Hutchison CJ. Nuclear lamins: laminopathies and their role in premature ageing. *Physiol Rev* 2006; 86:967–1008.
15. Malhas A, Goulbourne C, Vaux DJ. The nucleoplasmic reticulum: Form and function. *Trends Cell Biol* 2011; 21:362–73.
16. Naetar N, Ferraioli S, Foisner R. Lamins in the nuclear interior – life outside the lamina. *J Cell Sci* 2017; :2087–96.

17. Wilson KL, Foisner R. Lamin-binding Proteins. *Cold Spring Harb Perspect Biol* 2009; :1–17.
18. Stewart CL, Roux KJ, Burke B. Blurring the boundary: the nuclear envelope extends its reach. [Internet]. *Science* 2007; 318:1408–12.
19. Dechat T, Adam SA, Taimen P, Shimi T, Goldman RD. Nuclear lamins. *Cold Spring Harb. Perspect. Biol.* 2010; 2.
20. Stuurman N, Heins S, Aebi U. Nuclear lamins: their structure, assembly, and interactions. [Internet]. *J. Struct. Biol.* 1998; 122:42–66.
21. Nakajima N, Abe K. Genomic structure of the mouse A-type lamin gene locus encoding somatic and germ cell-specific lamins. *FEBS Lett* 1995; 365:108–14.
22. Furukawa K, Hotta Y. cDNA cloning of a germ cell specific lamin B3 from mouse spermatocytes and analysis of its function by ectopic expression in somatic cells. *EMBO J* 1993; 12:97–106.
23. Gerace L, Blobel G. The nuclear envelope lamina is reversibly depolymerized during mitosis. *Cell* 1980; 19:277–87.
24. Benavente R, Krohne G, Franke WW. Cell type-specific expression of nuclear lamina proteins during development of *Xenopus laevis*. *Cell* 1985; 41:177–90.
25. Lehner CF, Stick R, Eppenberger HM, Migg EA. Differential expression of nuclear lamin proteins during chicken development. *J Cell Biol* 1987; 105:577–87.
26. Schatten G, Maul GG, Schatten H, Chaly N, Simerly C, Balczon R, Brown DL. Nuclear lamins and peripheral nuclear antigens during fertilization and embryogenesis in mice and sea urchins. *Proc Natl Acad Sci U S A* 1985; 82:4727–31.
27. Constantinescu D, Gray HL, Sammak PJ, Schatten GP, Csoka AB. Lamin A/C expression is a marker of mouse and human embryonic stem cell differentiation. *Stem Cells* 2006; 24:177–85.
28. Rober R-A, Weber K, Osborn M. Differential timing of nuclear lamin A/C expression in the various organs of the mouse embryo and the young animal: a developmental study. *Development* 1989; 105:365–78.
29. Prokocimer M, Margalit A, Gruenbaum Y. The nuclear lamina and its proposed roles in tumorigenesis: Projection on the hematologic malignancies and future targeted therapy. *J Struct Biol* 2006; 155:351–60.
30. Machiels BM, Zorenc AHG, Endert JM, Kuijpers HJH, Van Eys GJJM, Ramaekers FCS, Broers JL V. An alternative splicing product of the lamin A/C gene lacks exon 10. *J Biol Chem* 1996; 271:9249–53.
31. Verstraeten VLRM, Broers JL V, Ramaekers FCS, van Steensel M a M. The nuclear envelope, a key structure in cellular integrity and gene expression. [Internet]. *Curr. Med. Chem.* 2007; 14:1231–48.
32. Swift J, Ivanovska IL, Buxboim A, Harada T, Dave PC, Dingal P, Pinter J, Pajerowski JD, Spinler KR, Shin J-W, et al. Nuclear Lamin-A Scales with Tissue Stiffness and Enhances Matrix-Directed Differentiation. 2013; 341.

33. Parry DAD, Conway JF, Steinertt PM. Structural studies on lamin Similarities and differences between lamin and intermediate-filament proteins. *Biochem J* 1986; 238:305–8.
34. Dhe-Paganon S, Werner ED, Chi YI, Shoelson SE. Structure of the globular tail of nuclear lamin. *J Biol Chem* 2002; 277:17381–4.
35. Loewinger L, McKeon F. Mutations in the nuclear lamin proteins resulting in their aberrant assembly in the cytoplasm. *EMBO J* 1988; 7:2301–9.
36. Shimi T, Kittisopikul M, Tran J, Goldman AE, Adam SA, Zheng Y, Jaqaman K, Goldman RD. Structural organization of nuclear lamins A, C, B1, and B2 revealed by superresolution microscopy. *Mol Biol Cell* 2015; 26:4075–86.
37. Davies BSJ, Fong LG, Yang SH, Coffinier C, Young SG. The posttranslational processing of prelamin A and disease. *Annu Rev Genomics Hum Genet* 2009; 10:153–74.
38. Rusiñol AE, Sinensky MS. Farnesylated lamins, progeroid syndromes and farnesyl transferase inhibitors. [Internet]. *J. Cell Sci.*2006; 119:3265–72.
39. Corrigan DP, Kuszczak D, Rusinol AE, Thewke DP, Hrycyna CA, Michaelis S, Sinensky MS. Prelamin A endoproteolytic processing in vitro by recombinant Zmpste24. *Biochem J* 2005; 387:129–38.
40. Winter-Vann AM, Casey PJ. Post-prenylation-processing enzymes as new targets in oncogenesis. *Nat Rev Cancer* 2005; 5:405–12.
41. Davies BS, Coffinier C, Yang SH, Barnes RH, Jung H-J, Young SG, Fong LG. Investigating the purpose of prelamin A processing. *Nucleus* 2010; 2:4–9.
42. Barrowman J, Hamblet C, Kane MS, Michaelis S. Requirements for efficient proteolytic cleavage of prelamin A by ZMPSTE24. *PLoS One* 2012; 7:e32120.
43. Sinensky M, Fantle K, Trujillo M, McLain T, Kupfer A, Dalton M. The processing pathway of prelamin A. *J Cell Sci* 1994; 107 (Pt 1):61–7.
44. Jung H-J, Nobumori C, Goulbourne CN, Tu Y, Lee JM, Tatar A, Wu D, Yoshinaga Y, de Jong PJ, Coffinier C, et al. Farnesylation of lamin B1 is important for retention of nuclear chromatin during neuronal migration. *Proc Natl Acad Sci U S A* 2013; 110:E1923-32.
45. Davies BSJ, Barnes RH, Tu Y, Ren S, Andres DA, Peter Spielmann H, Lammerding J, Wang Y, Young SG, Fong LG. An accumulation of non-farnesylated prelamin A causes cardiomyopathy but not progeria. *Hum Mol Genet* 2010; 19:2682–94.
46. Fong LG, Ng JK, Lammerding J, Vickers TA, Meta M, Coté N, Gavino B, Qiao X, Chang SY, Young SR, et al. Prelamin A and lamin A appear to be dispensable in the nuclear lamina. *J Clin Invest* 2006; 116:743–52.
47. Coffinier C, Jung HJ, Li Z, Nobumori C, Yun UJ, Farber EA, Davies BS, Weinstein MM, Yang SH, Lammerding J, et al. Direct synthesis of lamin A, bypassing prelamin a processing, causes misshapen nuclei in fibroblasts but no detectable pathology in mice. *J Biol Chem* 2010; 285:20818–26.
48. González-Granado JM, Navarro-Puche A, Molina-Sanchez P, Blanco-Berrocal

- M, Viana R, Font de Mora J, Andrés V. Sorting nexin 6 enhances lamin a synthesis and incorporation into the nuclear envelope. *PLoS One* 2014; 9:e115571.
49. Dessev G, Iovcheva C, Tasheva B, Goldman R. Protein kinase activity associated with the nuclear lamina. [Internet]. *Proc. Natl. Acad. Sci. U. S. A.* 1988; 85:2994–8.
 50. Goss VL, Hocevar BA, Thompson LJ, Stratton CA, Burns DJ, Fields AP. Identification of nuclear beta II protein kinase C as a mitotic lamin kinase. *J Biol Chem* 1994; 269:19074–80.
 51. Gruenbaum Y, Margalit A, Goldman RD, Shumaker DK, Wilson KL. The nuclear lamina comes of age. *Nat Rev Mol Cell Biol* 2005; 6:21–31.
 52. Sieprath T, Darwiche R, De Vos WH. Lamins as mediators of oxidative stress. *Biochem Biophys Res Commun* 2012; 421:635–9.
 53. Lammerding J, Fong LG, Ji JY, Reue K, Stewart CL, Young SG, Lee RT. Lamins a and C but not lamin B1 regulate nuclear mechanics. *J Biol Chem* 2006; 281:25768–80.
 54. De Vos WH, Houben F, Hoebe RA, Hennekam R, van Engelen B, Manders EMM, Ramaekers FCS, Broers JL V, Van Oostveldt P. Increased plasticity of the nuclear envelope and hypermobility of telomeres due to the loss of A-type lamins. *Biochim Biophys Acta - Gen Subj* 2010; 1800:448–58.
 55. Lammerding J, Schulze PC, Takahashi T, Kozlov S, Sullivan T, Kamm RD, Stewart CL, Lee RT. Lamin A/C deficiency causes defective nuclear mechanics and mechanotransduction. *J. Clin. Invest.* 2004; 113:370–8.
 56. De Vos WH, Van Neste L, Dieriks B, Joss GH, Van Oostveldt P. High content image cytometry in the context of subnuclear organization. *Cytometry A* 2010; 77:64–75.
 57. Broers JL V, Peeters E a G, Kuijpers HJH, Endert J, Bouten CVC, Oomens CWJ, Baaijens FPT, Ramaekers FCS. Decreased mechanical stiffness in LMNA-/- cells is caused by defective nucleo-cytoskeletal integrity: implications for the development of laminopathies. *Hum Mol Genet* 2004; 13:2567–80.
 58. Pajerowski JD, Dahl KN, Zhong FL, Sammak PJ, Discher DE. Physical plasticity of the nucleus in stem cell differentiation. *Proc Natl Acad Sci U S A* 2007; 104:15619–24.
 59. Verstraeten VLRM, Peckham L a, Olive M, Capell BC, Collins FS, Nabel EG, Young SG, Fong LG, Lammerding J. Protein farnesylation inhibitors cause donut-shaped cell nuclei attributable to a centrosome separation defect. *Proc Natl Acad Sci U S A* 2011; 108:4997–5002.
 60. Houben F, De Vos WH, Krapels IPC, Coorens M, Kierkels GJJ, Kamps M a F, Verstraeten VLRM, Marcelis CLM, Van Den Wijngaard a., Ramaekers FCS, et al. Cytoplasmic localization of PML particles in laminopathies. *Histochem Cell Biol* 2013; 139:119–34.
 61. Robijns J, Molenberghs F, Sieprath T, Corne TDJ, Verschuuren M, De Vos WH. In silico synchronization reveals regulators of nuclear ruptures in lamin A/C

- deficient model cells. *Sci Rep* 2016; 6:30325.
62. De vos WH, Houben F, Kamps M, Malhas A, Verheyen F, Cox J, Manders EMM, Verstraeten VLRM, van Steensel MAM, Marcelis CLM, et al. Repetitive disruptions of the nuclear envelope invoke temporary loss of cellular compartmentalization in laminopathies. *Hum Mol Genet* 2011; 20:4175–86.
 63. Lu W, Gotzmann J, Sironi L, Jaeger VM, Schneider M, Lüke Y, Uhlén M, Szigyarto CAK, Brachner A, Ellenberg J, et al. Sun1 forms immobile macromolecular assemblies at the nuclear envelope. *Biochim Biophys Acta - Mol Cell Res* 2008; 1783:2415–26.
 64. Simon DN, Zastrow MS, Wilson KL. Direct actin binding to A- and B-type lamin tails and actin filament bundling by the lamin A tail. *Nucleus* 2010; 1:264–72.
 65. Starr DA, Fridolfsson HN. Interactions Between Nuclei and the Cytoskeleton Are Mediated by SUN-KASH Nuclear-Envelope Bridges. *Annu Rev Cell Dev Biol* 2010; 26:421–44.
 66. Andrés V, González JM. Role of A-type lamins in signaling, transcription, and chromatin organization. [Internet]. *J. Cell Biol.*2009; 187:945–57.
 67. Cremer T, Cremer M, Dietzel S, Müller S, Solovei I, Fakan S. Chromosome territories--a functional nuclear landscape. [Internet]. *Curr. Opin. Cell Biol.*2006; 18:307–16.
 68. Solovei I, Wang AS, Thanisch K, Schmidt CS, Krebs S, Zwerger M, Cohen T V., Devys D, Foisner R, Peichl L, et al. LBR and lamin A/C sequentially tether peripheral heterochromatin and inversely regulate differentiation. *Cell* 2013; 152:584–98.
 69. Ludérus ME, den Blaauwen JL, de Smit OJ, Compton D a, van Driel R. Binding of matrix attachment regions to lamin polymers involves single-stranded regions and the minor groove. *Mol Cell Biol* 1994; 14:6297–305.
 70. Zhao K, Harel A, Stuurman N, Guedalia D, Gruenbaum Y. Binding of matrix attachment regions to nuclear lamin is mediated by the rod domain and depends on the lamin polymerization state. *FEBS Lett* 1996; 380:161–4.
 71. Lee KK, Haraguchi T, Lee RS, Koujin T, Hiraoka Y, Wilson KL. Distinct functional domains in emerin bind lamin A and DNA-bridging protein BAF. [Internet]. *J. Cell Sci.*2001; 114:4567–73.
 72. Mattout A, Goldberg M, Tzur Y, Margalit A, Gruenbaum Y. Specific and conserved sequences in *D. melanogaster* and *C. elegans* lamins and histone H2A mediate the attachment of lamins to chromosomes. *J Cell Sci* 2007; 120:77–85.
 73. Goldberg M, Harel a, Brandeis M, Rechsteiner T, Richmond TJ, Weiss a M, Gruenbaum Y. The tail domain of lamin Dm0 binds histones H2A and H2B. *Proc Natl Acad Sci U S A* 1999; 96:2852–7.
 74. Guelen L, Pagie L, Brasset E, Meuleman W, Faza MB, Talhout W, Eussen BH, de Klein A, Wessels L, de Laat W, et al. Domain organization of human chromosomes revealed by mapping of nuclear lamina interactions. *Nature* 2008; 453:948–51.

75. Peric-Hupkes D, Meuleman W, Pagie L, Bruggeman SWM, Solovei I, Brugman W, Gr??f S, Flicek P, Kerkhoven RM, van Lohuizen M, et al. Molecular Maps of the Reorganization of Genome-Nuclear Lamina Interactions during Differentiation. *Mol Cell* 2010; 38:603–13.
76. Shah PP, Donahue G, Otte GL, Capell BC, Nelson DM, Cao K, Aggarwala V, Cruickshanks H a., Rai TS, McBryan T, et al. Lamin B1 depletion in senescent cells triggers large-scale changes in gene expression and the chromatin landscape. *Genes Dev* 2013; 27:1787–99.
77. Shimi T, Pflgebraar K, Kojima SI, Pack CG, Solovei I, Goldman AE, Adam SA, Shumaker DK, Kinjo M, Cremer T, et al. The A- and B-type nuclear lamin networks: Microdomains involved in chromatin organization and transcription. *Genes Dev* 2008; 22:3409–21.
78. Galiová G, Bártová E, Raška I, Krejčí J, Kozubek S, Raska I, Krejčí J, Kozubek S. Chromatin changes induced by lamin A/C deficiency and the histone deacetylase inhibitor trichostatin A. *Eur J Cell Biol* 2008; 87:291–303.
79. Bronshtein I, Kepten E, Kanter I, Berezin S, Lindner M, Redwood AB, Mai S, Gonzalo S, Foisner R, Shav-Tal Y, et al. Loss of lamin A function increases chromatin dynamics in the nuclear interior. *Nat Commun* 2015; 6:8044.
80. Shumaker DK, Dechat T, Kohlmaier A, Adam SA, Bozovsky MR, Erdos MR, Eriksson M, Goldman AE, Khuon S, Collins FS, et al. Mutant nuclear lamin A leads to progressive alterations of epigenetic control in premature aging. *Proc Natl Acad Sci U S A* 2006; 103:8703–8.
81. Mattioli E, Columbaro M, Capanni C, Santi S, Maraldi NM, D'Apice MR, Novelli G, Riccio M, Squarzoni S, Foisner R, et al. Drugs affecting prelamin A processing: effects on heterochromatin organization. *Exp Cell Res* 2008; 314:453–62.
82. Kennedy BK, Barbie DA, Classon M, Dyson N, Harlow E. Nuclear organization of DNA replication in primary mammalian cells. *Genes Dev* 2000; 14:2855–68.
83. Moir RD, Montag-Lowy M, Goldman RD. Dynamic properties of nuclear lamins: Lamin B is associated with sites of DNA replication. *J Cell Biol* 1994; 125:1201–12.
84. Shumaker DK, Solimando L, Sengupta K, Shimi T, Adam SA, Grunwald A, Strelkov S V., Aebi U, Cardoso MC, Goldman RD. The highly conserved nuclear lamin Ig-fold binds to PCNA: Its role in DNA replication. *J Cell Biol* 2008; 181:269–80.
85. Singh M, Hunt CR, Pandita RK, Kumar R, Yang C-R, Horikoshi N, Bachoo R, Serag S, Story MD, Shay JW, et al. Lamin A/C depletion enhances DNA damage-induced stalled replication fork arrest. *Mol Cell Biol* 2013; 33:1210–22.
86. Meier J, Georgatos SD. Type B lamins remain associated with the integral nuclear envelope protein p58 during mitosis: implications for nuclear reassembly. *EMBO J* 1994; 13:1888–98.
87. Gonzalez-Suarez I, Redwood AB, Perkins SM, Vermolen B, Lichtensztejin D, Grotsky D a, Morgado-Palacin L, Gapud EJ, Sleckman BP, Sullivan T, et al.

- Novel roles for A-type lamins in telomere biology and the DNA damage response pathway. *EMBO J* 2009; 28:2414–27.
88. Raab M, Gentili M, Belly H De, Thiam H, Vargas P, Jimenez AJ, Lautenschlaeger F, Voituriez R, Manel N, Piel M. ESCRT III repairs nuclear envelope ruptures during cell migration to limit DNA damage and cell death. 2016; 352:359–63.
 89. Denais CM, Gilbert RM, Isermann P, Mcgregor AL, Lindert M, Weigelin B, Davidson PM, Friedl P, Wolf K, Lammerding J. Nuclear envelope rupture and repair during cancer cell migration. 2016; 352.
 90. Redwood AB, Perkins SM, Vanderwaal RP, Feng Z, Biehl KJ, Gonzalez-Suarez I, Morgado-Palacin L, Shi W, Sage J, Roti-Roti JL, et al. A dual role for A-type lamins in DNA double-strand break repair. *Cell Cycle* 2011; 10:2549–60.
 91. Redwood AB, Gonzalez-Suarez I, Gonzalo S. Regulating the levels of key factors in cell cycle and DNA repair: New pathways revealed by lamins. *Cell Cycle* 2011; 10:3652–7.
 92. Liu B, Wang J, Chan KM, Tjia WM, Deng W, Guan X, Huang J, Li KM, Chau PY, Chen DJ, et al. Genomic instability in laminopathy-based premature aging. *Nat Med* 2005; 11:780–5.
 93. Manju K, Muralikrishna B, Parnaik VK. Expression of disease-causing lamin A mutants impairs the formation of DNA repair foci. *J Cell Sci* 2006; 119:2704–14.
 94. Varela I, Cadinanos J, Pendas AM, Gutierrez-Fernandez A, Folgueras AR, Sanchez LM, Zhou Z, Rodriguez FJ, Stewart CL, Vega JA, et al. Accelerated ageing in mice deficient in Zmpste24 protease is linked to p53 signalling activation. *Nature* 2005; 437:564–8.
 95. Heessen S, Fornerod M. The inner nuclear envelope as a transcription factor resting place. *EMBO Rep* 2007; 8:914–9.
 96. Ivorra C, Kubicek M, González JM, Sanz-González SM, Álvarez-Barrientos A, O'Connor J-EE, Burke B, Andrés V, Alvarez-Barrientos A, O'Connor J-EE, et al. A mechanism of AP-1 suppression through interaction of c-Fos with lamin A/C. *Genes Dev* 2006; 20:307–20.
 97. González JM, Navarro-Puche A, Casar B, Crespo P, Andrés V. Fast regulation of AP-1 activity through interaction of lamin A/C, ERK1/2, and c-Fos at the nuclear envelope. *J Cell Biol* 2008; 183:653–66.
 98. Dreuillet C. In vivo and in vitro interaction between human transcription factor MOK2 and nuclear lamin A/C. *Nucleic Acids Res* 2002; 30:4634–42.
 99. Lloyd DJ, Trembath RC, Shackleton S. A novel interaction between lamin A and SREBP1: implications for partial lipodystrophy and other laminopathies. *Hum Mol Genet* 2002; 11:769–77.
 100. Capanni C, Mattioli E, Columbaro M, Lucarelli E, Parnaik VK, Novelli G, Wehnert M, Cenni V, Maraldi NM, Squarzoni S, et al. Altered pre-lamin A processing is a common mechanism leading to lipodystrophy. *Hum Mol Genet* 2005; 14:1489–502.
 101. Malhas AN, Lee CF, Vaux DJ. Lamin B1 controls oxidative stress responses via

- Oct-1. *J Cell Biol* 2009; 184:45–55.
102. Markiewicz E, Tilgner K, Barker N, van de Wetering M, Clevers H, Dorobek M, Hausmanowa-Petrusewicz I, Ramaekers FCS, Broers JL V, Blankesteyn WM, et al. The inner nuclear membrane protein emerin regulates beta-catenin activity by restricting its accumulation in the nucleus. *EMBO J* 2006; 25:3275–85.
 103. Hellemans J, Preobrazhenska O, Willaert A, Debeer P, Verdonk PCM, Costa T, Janssens K, Menten B, Van Roy N, Vermeulen SJT, et al. Loss-of-function mutations in LEMD3 result in osteopoikilosis, Buschke-Ollendorff syndrome and melorheostosis. *Nat Genet* 2004; 36:1213–8.
 104. Martineau LC, Gardiner PF. Insight into skeletal muscle mechanotransduction: MAPK activation is quantitatively related to tension. *J Appl Physiol* 2001; 91:693–702.
 105. Ho CY, Jaalouk DE, Vartiainen MK, Lammerding J. Lamin A/C and emerin regulate MKL1-SRF activity by modulating actin dynamics. *Nature* 2013; 497:507–11.
 106. Emerson LJ, Holt MR, Wheeler MA, Wehnert M, Parsons M, Ellis JA. Defects in cell spreading and ERK1/2 activation in fibroblasts with lamin A/C mutations. *Biochim Biophys Acta - Mol Basis Dis* 2009; 1792:810–21.
 107. Muchir A, Pavlidis P, Decostre V, Herron AJ, Arimura T, Bonne G, Worman HJ. Activation of MAPK pathways links LMNA mutations to cardiomyopathy in Emery-Dreifuss muscular dystrophy. *J Clin Invest* 2007; 117:1282–93.
 108. Muchir A, Wu W, Sera F, Homma S, Worman HJ. Mitogen-activated protein kinase kinase 1/2 inhibition and angiotensin II converting inhibition in mice with cardiomyopathy caused by lamin A/C gene mutation. *Biochem Biophys Res Commun* 2014; 452:958–61.
 109. Roskoski R. ERK1/2 MAP kinases: Structure, function, and regulation. *Pharmacol Res* 2012; 66:105–43.
 110. Yang SH, Jung H-J, Coffinier C, Fong LG, Young SG. Are B-type lamins essential in all mammalian cells? *Nucleus* 2011; 2:562–9.
 111. Coffinier C, Chang SY, Nobumori C, Tu Y, Farber EA, Toth JI, Fong LG, Young SG. Abnormal development of the cerebral cortex and cerebellum in the setting of lamin B2 deficiency. *Proc Natl Acad Sci U S A* 2010; 107:5076–81.
 112. Szeverenyi I, Cassidy AJ, Cheuk WC, Lee BTK, Common JEA, Ogg SC, Chen H, Shu YS, Goh WLP, Kee WN, et al. The human intermediate filament database: Comprehensive information on a gene family involved in many human diseases. *Hum Mutat* 2008; 29:351–60.
 113. Dittmer TA, Misteli T, Aaronson R, Blobel G, Gerace L, Blum A, Blobel G, McKeon F, Kirschner M, Caput D, et al. The lamin protein family. *Genome Biol* 2011; 12:222.
 114. Parnaik VK, Chaturvedi P, Muralikrishna B. Lamins, laminopathies and disease mechanisms: Possible role for proteasomal degradation of key regulatory proteins. *J Biosci* 2011; 36:471–9.

115. Raffaele Di Barletta M, Ricci E, Galluzzi G, Tonali P, Mora M, Morandi L, Romorini A, Voit T, Orstavik KH, Merlini L, et al. Different mutations in the LMNA gene cause autosomal dominant and autosomal recessive Emery-Dreifuss muscular dystrophy. *Am J Hum Genet* 2000; 66:1407–12.
116. Muchir a, Bonne G, van der Kooi a J, van Meegen M, Baas F, Bolhuis P a, de Visser M, Schwartz K. Identification of mutations in the gene encoding lamins A/C in autosomal dominant limb girdle muscular dystrophy with atrioventricular conduction disturbances (LGMD1B). *Hum Mol Genet* 2000; 9:1453–9.
117. Novelli G, Muchir A, Sangiuolo F, Helbling-Leclerc A, D'Apice MR, Massart C, Capon F, Sbraccia P, Federici M, Lauro R, et al. Mandibuloacral Dysplasia Is Caused by a Mutation in LMNA-Encoding Lamin A/C. *Am J Hum Genet* 2002; 71:426–31.
118. Shackleton S, Lloyd DJ, Jackson SN, Evans R, Niermeijer MF, Singh BM, Schmidt H, Brabant G, Kumar S, Durrington PN, et al. LMNA, encoding lamin A/C, is mutated in partial lipodystrophy. *Nat Genet* 2000; 24:153–6.
119. Navarro CL, De Sandre-Giovannoli A, Bernard R, Boccaccio I, Boyer A, Geneviève D, Hadj-Rabia S, Gaudy-Marqueste C, Smitt HS, Vabres P, et al. Lamin A and ZMPSTE24 (FACE-1) defects cause nuclear disorganization and identify restrictive dermopathy as a lethal neonatal laminopathy. *Hum Mol Genet* 2004; 13:2493–503.
120. Renard D, Fourcade G, Milhaud D, Bessis D, Esteves-Vieira V, Boyer A, Roll P, Bourgeois P, Levy N, De Sandre-Giovannoli A. Novel LMNA mutation in atypical Werner syndrome presenting with ischemic disease. *Stroke* 2009; 40:e11-4.
121. Lopez-Mejia IC, Vautrot V, De Toledo M, Behm-Ansmant I, Bourgeois CF, Navarro CL, Osorio FG, Freije JMP, Stévenin J, De Sandre-Giovannoli A, et al. A conserved splicing mechanism of the LMNA gene controls premature aging. *Hum Mol Genet* 2011; 20:4540–55.
122. Garg A, Subramanyam L, Agarwal AK, Simha V, Levine B, D'Apice MR, Novelli G, Crow Y. Atypical Progeroid Syndrome due to Heterozygous Missense LMNA Mutations. *J Clin Endocrinol Metab* 2009; 94:4971–83.
123. Luo D-Q, Wang X-Z, Meng Y, He D-Y, Chen Y-M, Ke Z-Y, Yan M, Huang Y, Chen D-F. Mandibuloacral dysplasia type A-associated progeria caused by homozygous LMNA mutation in a family from Southern China. *BMC Pediatr* 2014; 14:256.
124. Chen L, Lee L, Kudlow BA, Dos Santos HG, Sletvold O, Shafeghati Y, Botha EG, Garg A, Hanson NB, Martin GM, et al. LMNA mutations in atypical Werner's syndrome. *Lancet* 2003; 362:440–5.
125. Eriksson M, Brown WT, Gordon LB, Glynn MW, Singer J, Scott L, Erdos MR, Robbins CM, Moses TY, Berglund P, et al. Recurrent de novo point mutations in lamin A cause Hutchinson-Gilford progeria syndrome. *Nature* 2003; 423:293–8.
126. Ben Yaou R, Navarro C, Quijano-Roy S, Bertrand AT, Massart C, De Sandre-Giovannoli A, Cadiñanos J, Mamchaoui K, Butler-Browne G, Estournet B, et al. Type B mandibuloacral dysplasia with congenital myopathy due to homozygous ZMPSTE24 missense mutation. *Eur J Hum Genet* 2011; 19:647–54.

127. Moulson CL, Go G, Gardner JM, van der Wal AC, Smitt JHS, van Hagen JM, Miner JH. Homozygous and compound heterozygous mutations in ZMPSTE24 cause the laminopathy restrictive dermopathy. *J Invest Dermatol* 2005; 125:913–9.
128. Peinado JR, Quirós PM, Pulido MR, Mariño G, Martínez-Chantar ML, Vázquez-Martínez R, Freije JMP, López-Otín C, Malagón MM. Proteomic profiling of adipose tissue from *Zmpste24*^{-/-} mice, a model of lipodystrophy and premature aging, reveals major changes in mitochondrial function and vimentin processing. *Mol Cell Proteomics* 2011; 10:M111.008094.
129. Barrowman J, Wiley PA, Hudon-Miller SE, Hrycyna CA, Michaelis S. Human ZMPSTE24 disease mutations: Residual proteolytic activity correlates with disease severity. *Hum Mol Genet* 2012; 21:4084–93.
130. Denecke J, Brune T, Feldhaus T, Robenek H, Kranz C, Auchus RJ, Agarwal AK, Marquardt T. A homozygous ZMPSTE24 null mutation in combination with a heterozygous mutation in the LMNA gene causes Hutchinson-Gilford progeria syndrome (HGPS): insights into the pathophysiology of HGPS. *Hum Mutat* 2006; 27:524–31.
131. Simha V, Garg A. Body fat distribution and metabolic derangements in patients with familial partial lipodystrophy associated with mandibuloacral dysplasia. *J Clin Endocrinol Metab* 2002; 87:776–85.
132. Azibani F, Muchir A, Vignier N, Bonne G, Bertrand AT. Striated muscle laminopathies. *Semin Cell Dev Biol* 2014; 29:107–15.
133. Aliper AM, Csoka AB, Buzdin A, Jetka T, Roumiantsev S, Moskalev A, Zhavoronkov A. Signaling pathway activation drift during aging: Hutchinson-Gilford Progeria Syndrome fibroblasts are comparable to normal middle-age and old-age cells. *Aging (Albany NY)* 2015; 7:26–37.
134. Carrero D, Soria-valles C, Lo C. Hallmarks of progeroid syndromes : lessons from mice and reprogrammed cells. 2016; :719–35.
135. Favreau C, Higuete D, Courvalin J-C, Buendia B. Expression of a Mutant Lamin A That Causes Emery-Dreifuss Muscular Dystrophy Inhibits In Vitro Differentiation of C2C12 Myoblasts. *Mol Cell Biol* 2004; 24:1481–92.
136. Plasilova M, Chattopadhyay C, Ghosh A, Wenzel F, Demougin P, Noppen C, Schaub N, Szinnai G, Terracciano L, Heinemann K. Discordant gene expression signatures and related phenotypic differences in lamin A- and A/C-related Hutchinson-Gilford progeria syndrome (HGPS). *PLoS One* 2011; 6:e21433.
137. Yu K-R, Lee S, Jung J-W, Hong I-S, Kim H-S, Seo Y, Shin T-H, Kang K-S. MicroRNA-141-3p plays a role in human mesenchymal stem cell aging by directly targeting ZMPSTE24. *J Cell Sci* 2013;
138. Cao K, Graziotto JJ, Blair CD, Mazzulli JR, Erdos MR, Krainc D, Collins FS. Rapamycin reverses cellular phenotypes and enhances mutant protein clearance in Hutchinson-Gilford progeria syndrome cells. *Sci Transl Med* 2011; 3:89ra58.
139. Taylor MRG, Fain PR, Sinagra G, Robinson ML, Robertson AD, Carniel E, Di

- Lenarda A, Bohlmeyer TJ, Ferguson DA, Brodsky GL, et al. Natural history of dilated cardiomyopathy due to lamin A/C gene mutations. *J Am Coll Cardiol* 2003; 41:771–80.
140. Codd MB, Sugrue DD, Gersh BJ, Melton LJ. Epidemiology of idiopathic dilated and hypertrophic cardiomyopathy. A population-based study in Olmsted County, Minnesota, 1975-1984. *Circulation* 1989; 80:564–72.
 141. Diane F, Calum M, Takeshi S, R. WM, Maurizio P, Michael F, John A, Jr. VHJ, Serena S, Umberto DG, et al. Missense Mutations in the Rod Domain of the Lamin A/C Gene as Causes of Dilated Cardiomyopathy and Conduction-System Disease. *N Engl J Med* 1999; 341:1715–24.
 142. Lu JT, Muchir A, Nagy PL, Worman HJ. LMNA cardiomyopathy: cell biology and genetics meet clinical medicine. *Dis Model Mech* 2011; 4:562–8.
 143. van Engelen BGM, Muchir a, Hutchison CJ, van der Kooi a J, Bonne G, Lammens M. The lethal phenotype of a homozygous nonsense mutation in the lamin A/C gene. *Neurology* 2005; 64:374–6.
 144. Sullivan T, Escalante-Alcalde D, Bhatt H, Anver M, Bhat N, Nagashima K, Stewart CL, Burke B. Loss of A-type lamin expression compromises nuclear envelope integrity leading to muscular dystrophy. *J Cell Biol* 1999; 147:913–9.
 145. Wolf CM, Wang L, Alcalai R, Pizard A, Burgon PG, Ahmad F, Sherwood M, Branco DM, Wakimoto H, Fishman GI, et al. Lamin A/C haploinsufficiency causes dilated cardiomyopathy and apoptosis-triggered cardiac conduction system disease. *J Mol Cell Cardiol* 2008; 44:293–303.
 146. Krimm I, Östlund C, Gilquin B, Couprie J, Hossenlopp P, Mornon JP, Bonne G, Courvalin JC, Worman HJ, Zinn-Justin S. The Ig-like structure of the C-terminal domain of lamin A/C, mutated in muscular dystrophies, cardiomyopathy, and partial lipodystrophy. *Structure* 2002; 10:811–23.
 147. Camozzi D, D'Apice MR, Schena E, Cenni V, Columbaro M, Capanni C, Maraldi NM, Squarzoni S, Ortolani M, Novelli G, et al. Altered chromatin organization and SUN2 localization in mandibuloacral dysplasia are rescued by drug treatment. *Histochem Cell Biol* 2012; 138:643–51.
 148. Tu Y, Sánchez-iglesias S, Araújo-vilar D, Fong LG, Young SG, Tu Y, Sánchez-iglesias S, Araújo-vilar D, Loren G. LMNA missense mutations causing familial partial lipodystrophy do not lead to an accumulation of prelamin A. *Nucleus* 2016; 7:512–21.
 149. Cao K, Capell BC, Erdos MR, Djabali K, Collins FS. A lamin A protein isoform overexpressed in Hutchinson-Gilford progeria syndrome interferes with mitosis in progeria and normal cells. *Proc Natl Acad Sci* 2007; 104:4949–54.
 150. Pierard-Franchimont C, Pierard GE, Hermanns-Le T, Arrese Estrada J, Verloes A, Mulliez N. Dermatopathological aspects of restrictive dermopathy. *J Pathol* 1992; 167:223–8.
 151. Yang SH, Bergo MO, Toth JI, Qiao X, Hu Y, Sandoval S, Meta M, Bendale P, Gelb MH, Young SG, et al. Blocking protein farnesyltransferase improves nuclear blebbing in mouse fibroblasts with a targeted Hutchinson-Gilford

- progeria syndrome mutation. *Proc Natl Acad Sci U S A* 2005; 102:10291–6.
152. Scaffidi P, Misteli T. Lamin A-dependent nuclear defects in human aging. [Internet]. *Science* 2006; 312:1059–63.
 153. Cao K, Blair CD, Faddah DA, Kieckhaefer JE, Olive M, Erdos MR, Nabel EG, Collins FS. Progerin and telomere dysfunction collaborate to trigger cellular senescence in normal human fibroblasts. *J Clin Invest* 2011; 121:2833–44.
 154. Yu K-R, Lee S, Jung J-W, Hong I-S, Kim H-S, Seo Y, Shin T -h., Kang K-S. MicroRNA-141-3p plays a role in human mesenchymal stem cell aging by directly targeting ZMPSTE24. *J Cell Sci* 2014; 127:475–475.
 155. Gordon LB, Kleinman ME, Miller DT, Neuberg DS, Giobbie-Hurder A, Gerhard-Herman M, Smoot LB, Gordon CM, Cleveland R, Snyder BD, et al. Clinical trial of a farnesyltransferase inhibitor in children with Hutchinson-Gilford progeria syndrome. *Proc Natl Acad Sci U S A* 2012; 109:16666–71.
 156. Varela I, Pereira S, Ugalde AP, Navarro CL, Suárez MF, Cau P, Cadiñanos J, Osorio FG, Foray N, Cobo J, et al. Combined treatment with statins and aminobisphosphonates extends longevity in a mouse model of human premature aging. *Nat Med* 2008; 14:767–72.
 157. Konstantinopoulos PA, Papavassiliou AG. Multilevel modulation of the mevalonate and protein-prenylation circuitries as a novel strategy for anticancer therapy. *Trends Pharmacol Sci* 2007; 28:6–13.
 158. Cenni V, Capanni C, Mattioli E, Columbaro M, Wehnert M, Ortolani M, Fini M, Novelli G, Bertacchini J, Maraldi NM, et al. Rapamycin treatment of Mandibuloacral Dysplasia cells rescues localization of chromatin-associated proteins and cell cycle dynamics. *Aging (Albany NY)* 2014; 6:755–70.
 159. Gabriel D, Roedl D, Gordon LB, Djabali K. Sulforaphane enhances progerin clearance in Hutchinson-Gilford progeria fibroblasts. *Aging Cell* 2015; 14:78–91.
 160. Egesipe A-L, Blondel S, Cicero A Lo, Jaskowiak A-L, Navarro C, Sandre-Giovannoli A De, Levy N, Peschanski M, Nissan X. Metformin decreases progerin expression and alleviates pathological defects of Hutchinson–Gilford progeria syndrome cells. *npj Aging Mech Dis* 2016; 2:16026.
 161. Liu B, Ghosh S, Yang X, Zheng H, Liu X, Wang Z, Jin G, Zheng B, Kennedy BK, Suh Y, et al. Resveratrol rescues SIRT1-dependent adult stem cell decline and alleviates progeroid features in laminopathy-based progeria. *Cell Metab* 2012; 16:738–50.
 162. Ghosh S, Liu B, Zhou Z. Resveratrol activates SIRT1 in a Lamin A-dependent manner. *Cell Cycle* 2013; 12:872–6.
 163. Hutchison CA. DNA sequencing: Bench to bedside and beyond. *Nucleic Acids Res* 2007; 35:6227–37.
 164. Shendure J, Ji H. Next-generation DNA sequencing. *Nat Biotechnol* 2008; 26:1135–45.
 165. Metzker ML. Sequencing technologies - the next generation. *Nat Rev Genet* 2010; 11:31–46.

166. Lee H, Gurtowski J, Yoo S, Nattestad M, Marcus S, Goodwin S, McCombie WR, Schatz M. Third-generation sequencing and the future of genomics. *bioRxiv* 2016; :48603.
167. Abdallah C, Dumas-Gaudot E, Renaut J, Sergeant K. Gel-based and gel-free quantitative proteomics approaches at a glance. *Int J Plant Genomics* 2012; 2012:494572.
168. Chandramouli K, Qian P-Y. Proteomics: challenges, techniques and possibilities to overcome biological sample complexity. *Hum Genomics Proteomics* 2009; 2009:22.
169. Li Z, Adams RM, Chourey K, Hurst GB, Hettich RL, Pan C. Systematic comparison of label-free, metabolic labeling, and isobaric chemical labeling for quantitative proteomics on LTQ orbitrap velos. *J Proteome Res* 2012; 11:1582–90.
170. Jensen ON. Modification-specific proteomics: characterization of post-translational modifications by mass spectrometry. *Curr Opin Chem Biol* 2004; 8:33–41.
171. Boisvert F-M, Lam YW, Lamont D, Lamond AI. A quantitative proteomics analysis of subcellular proteome localization and changes induced by DNA damage. *Mol Cell Proteomics* 2010; 9:457–70.
172. Boisvert F-M, Ahmad Y, Gierliński M, Charrière F, Lamont D, Scott M, Barton G, Lamond AI. A quantitative spatial proteomics analysis of proteome turnover in human cells. *Mol Cell Proteomics* 2012; 11:M111.011429.
173. Lodish H, Berk A, Kaiser CA, Krieger M, Bretscher A, Ploegh H, Amon A, Scott MP, Martin K. *Molecular cell biology* [Internet]. 2016.
174. Thorn K. A quick guide to light microscopy in cell biology. *Mol Biol Cell* 2016; 27:219–22.
175. Fernández-Suárez M, Ting AY. Fluorescent probes for super-resolution imaging in living cells. *Nat Rev Mol Cell Biol* 2008; 9:929–43.
176. Renz M. Fluorescence microscopy-A historical and technical perspective. *Cytom Part A* 2013; 83:767–79.
177. Wang E, Babbey CM, Dunn KW. Performance comparison between the high-speed Yokogawa spinning disc confocal system and single-point scanning confocal systems. *J Microsc* 2005; 218:148–59.
178. Wollman R, Stuurman N. High throughput microscopy: from raw images to discoveries. *J Cell Sci* 2007; 120:3715–22.
179. Pepperkok R, Ellenberg J. High-throughput fluorescence microscopy for systems biology. *Nat Rev Mol Cell Biol* 2006; 7:690–6.
180. Rimon N, Schuldiner M. Getting the whole picture: combining throughput with content in microscopy. *J Cell Sci* 2011; 124:3743–51.
181. Roukos V, Misteli T. Deep Imaging: The next frontier in microscopy. *Histochem Cell Biol* 2014; 142:125–31.

182. Klein K, Gigler AM, Aschenbrenner T, Monetti R, Bunk W, Jamitzky F, Morfill G, Stark RW, Schlegel J. Label-free live-cell imaging with confocal Raman microscopy. *Biophys J* 2012; 102:360–8.
183. Wegner KD, Hildebrandt N. Quantum dots: bright and versatile in vitro and in vivo fluorescence imaging biosensors. *Chem Soc Rev* 2015; 44:4792–834.
184. Schie IWW, Huser T. Methods and Applications of Raman Microspectroscopy to Single-Cell Analysis. *Appl Spectrosc* 2013; 67:813–28.
185. Raman C V., Krishnan KS. A new class of spectra due to secondary radiation. *Indian J Phys* 1928; 2:399–419.
186. Kano H, Segawa H, Leproux P, Couderc V. Linear and nonlinear Raman microspectroscopy: History, instrumentation, and applications. *Opt Rev* 2014; 21:752–61.
187. Hedegaard M, Matthäus C, Hassing S, Krafft C, Popp J. Spectral unmixing and clustering algorithms for assessment of single cells by Raman microscopic imaging. 2011; 130:1249–60.
188. Kong K, Kendall C, Stone N, Notingher I. Raman spectroscopy for medical diagnostics - From in-vitro biofluid assays to in-vivo cancer detection. *Adv Drug Deliv Rev* 2015; 89:121–34.
189. Marro M, Nieva C, Sanz-Pamplona R, Sierra a. Molecular monitoring of epithelial-to-mesenchymal transition in breast cancer cells by means of Raman spectroscopy. *Biochim Biophys Acta - Mol Cell Res* 2014; 1843:1785–95.
190. Neugebauer U, Bocklitz T, Clement JH, Krafft C, Popp J. Towards detection and identification of circulating tumour cells using Raman spectroscopy. *Analyst* 2010; 135:3178–82.
191. Tolstik T, Marquardt C, Matthäus C, Bergner N, Bielecki C, Krafft C, Stallmach a., Popp J. Discrimination and classification of liver cancer cells and proliferation states by Raman spectroscopic imaging. *Analyst* 2014; 139:6036–43.
192. Beleites C, Neugebauer U, Bocklitz T, Krafft C, Popp J. Sample size planning for classification models. *Anal Chim Acta* 2013; 760:25–33.
193. Konorov SO, Jardon M a, Piret JM, Blades MW, Turner RFB. Raman microspectroscopy of live cells under autophagy-inducing conditions. *Analyst* 2012; 137:4662–8.
194. Czamara K, Majzner K, Selmi A, Baranska M, Ozaki Y, Kaczor A. Unsaturated lipid bodies as a hallmark of inflammation studied by Raman 2D and 3D microscopy. *Sci Rep* 2017; 7:40889.
195. Liu P-Q, Tan S, Mendel MC, Murrills RJ, Bhat BM, Schlag B, Samuel R, Matteo JJ, de la Rosa R, Howes K, et al. Isogenic Human Cell Lines for Drug Discovery: Regulation of Target Gene Expression by Engineered Zinc-Finger Protein Transcription Factors. *J Biomol Screen* 2005; 10:304–13.
196. Burkhardt AM, Zlotnik A. Translating translational research: mouse models of human disease. *Cell Mol Immunol* 2013; 10:373–4.
197. Mak IW, Evaniew N, Ghert M. Lost in translation: animal models and clinical trials

- in cancer treatment. *Am J Transl Res* 2014; 6:114–8.
198. Candelario J, Borrego S, Reddy S, Comai L. Accumulation of distinct prelamin A variants in human diploid fibroblasts differentially affects cell homeostasis. *Exp Cell Res* 2011; 317:319–29.
 199. Goldman RD, Shumaker DK, Erdos MR, Eriksson M, Goldman AE, Gordon LB, Gruenbaum Y, Khuon S, Mendez M, Varga R, et al. Accumulation of mutant lamin A causes progressive changes in nuclear architecture in Hutchinson–Gilford progeria syndrome. *Proc Natl Acad Sci U S A* 2004; 101:8963–8.
 200. Navarro CL, Cadiñanos J, Sandre-Giovannoli A De, Bernard R, Courrier S, Boccaccio I, Boyer A, Kleijer WJ, Wagner A, Giuliano F, et al. Loss of ZMPSTE24 (FACE-1) causes autosomal recessive restrictive dermopathy and accumulation of Lamin A precursors. *Hum Mol Genet* 2005; 14:1503–13.
 201. Malhas AN, Vaux DJ. The nuclear envelope and its involvement in cellular stress responses. *Biochem Soc Trans* 2011; 39:1795–8.
 202. Barascu A, Le Chalony C, Pennarun G, Genet D, Zaarour N, Bertrand P. Oxydative stress alters nuclear shape through lamins dysregulation: a route to senescence. *Nucleus* 2012; 3:411–7.
 203. Lattanzi G, Marmiroli S, Facchini A, Maraldi NM. Nuclear damages and oxidative stress: new perspectives for laminopathies. *Eur J Histochem* 2012; 56:e45.
 204. Caron M, Auclair M, Donadille B, Béréziat V, Guerci B, Laville M, Narbonne H, Bodemer C, Lascols O, Capeau J, et al. Human lipodystrophies linked to mutations in A-type lamins and to HIV protease inhibitor therapy are both associated with prelamin A accumulation, oxidative stress and premature cellular senescence. *Cell Death Differ* 2007; 14:1759–67.
 205. Rivera-Torres J, Acín-Perez R, Cabezas-Sánchez P, Osorio FG, Gonzalez-Gómez C, Megias D, Cámara C, López-Otín C, Enríquez JA, Luque-García JL, et al. Identification of Mitochondrial Dysfunction in Hutchinson-Gilford Progeria Syndrome Through Use of Stable Isotope Labelling with Amino Acids in Cell Culture. *J Proteomics* 2013;
 206. Lawless C, Wang C, Jurk D, Merz A, Zglinicki T Von, Passos JF. Quantitative assessment of markers for cell senescence. *Exp Gerontol* 2010; 45:772–8.
 207. Muchir A, Van Engelen BG, Lammens M, Mislou JM, McNally E, Schwartz K, Bonne G. Nuclear envelope alterations in fibroblasts from LGMD1B patients carrying nonsense Y259X heterozygous or homozygous mutation in lamin A/C gene. *Exp Cell Res* 2003; 291:352–62.
 208. Verstraeten VLRM, Broers JL V, van Steensel MAM, Zinn-Justin S, Ramaekers FCS, Steijlen PM, Kamps M, Kuijpers HJH, Merckx D, Smeets HJM, et al. Compound heterozygosity for mutations in LMNA causes a progeria syndrome without prelamin A accumulation. *Hum Mol Genet* 2006; 15:2509–22.
 209. Zhang D, Cui Y, Niu L, Xu X, Tian K, Young CYF, Lou H, Yuan H. Regulation of SOD2 and β -arrestin1 by interleukin-6 contributes to the increase of IGF-1R expression in docetaxel resistant prostate cancer cells. *Eur J Cell Biol* 2014; 93:289–98.

210. Broers JL, Machiels BM, van Eys GJ, Kuijpers HJ, Manders EM, van Driel R, Ramaekers FC. Dynamics of the nuclear lamina as monitored by GFP-tagged A-type lamins. [Internet]. *J. Cell Sci.* 1999; 112 (Pt 2:3463–75.
211. Goulbourne CN, Malhas AN, Vaux DJ. The induction of a nucleoplasmic reticulum by prelamin A accumulation requires CTP:phosphocholine cytidyltransferase- α . *J Cell Sci* 2011; 124:4253–66.
212. Richards S a, Muter J, Ritchie P, Lattanzi G, Hutchison CJ. The accumulation of un-repairable DNA damage in laminopathy progeria fibroblasts is caused by ROS generation and is prevented by treatment with N-acetyl cysteine. *Hum Mol Genet* 2011; 20:3997–4004.
213. Pekovic V, Gibbs-Seymour I, Markiewicz E, Alzoghaibi F, Benham AM, Edwards R, Wenher M, von Zglinicki T, Hutchison CJ. Conserved cysteine residues in the mammalian lamin A tail are essential for cellular responses to ROS generation. *Aging Cell* 2011; 10:1067–79.
214. Lattanzi G, Ortolani M, Columbaro M, Prencipe S, Mattioli E, Lanzarini C, Maraldi NM, Cenni V, Garagnani P, Salvioli S, et al. Lamins are rapamycin targets that impact human longevity: a study in centenarians. *J Cell Sci* 2014; 127:147–57.
215. Korshunov SS, Skulachev VP, Starkov A a. High protonic potential actuates a mechanism of production of reactive oxygen species in mitochondria. *FEBS Lett* 1997; 416:15–8.
216. Turrens JF. Mitochondrial formation of reactive oxygen species. *J Physiol* 2003; 552:335–44.
217. Maharjan S, Oku M, Tsuda M, Hoseki J, Sakai Y. Mitochondrial impairment triggers cytosolic oxidative stress and cell death following proteasome inhibition. *Sci Rep* 2014; 4:5896.
218. Muchir A, Massart C, van Engelen BG, Lammens M, Bonne G, Worman HJ. Proteasome-mediated degradation of integral inner nuclear membrane protein emerin in fibroblasts lacking A-type lamins. *Biochem Biophys Res Commun* 2006; 351:1011–7.
219. Chen C-Y, Chi Y-H, Mutalif RA, Starost MF, Myers TG, Anderson SA, Stewart CL, Jeang K-T. Accumulation of the inner nuclear envelope protein Sun1 is pathogenic in progeric and dystrophic laminopathies. *Cell* 2012; 149:565–77.
220. Muralikrishna B, Chaturvedi P, Sinha K, Parnaik VK. Lamin misexpression upregulates three distinct ubiquitin ligase systems that degrade ATR kinase in HeLa cells. *Mol Cell Biochem* 2012; :1–10.
221. Osorio FG, Bárcena C, Soria-Valles C, Ramsay AJ, de Carlos F, Cobo J, Fueyo A, Freije JMP, López-Otín C. Nuclear lamina defects cause ATM-dependent NF- κ B activation and link accelerated aging to a systemic inflammatory response. *Genes Dev* 2012; 26:2311–24.
222. Chien Y, Scuoppo C, Wang X, Fang X, Balgley B, Bolden JE, Premssirut P, Luo W, Chicas A, Lee CS, et al. Control of the senescence-associated secretory phenotype by NF- κ B promotes senescence and enhances chemosensitivity. *Genes Dev* 2011; 25:2125–36.

223. Kojima H, Kunimoto H, Inoue T, Nakajima K. The STAT3-IGFBP5 axis is critical for IL-6/gp130-induced premature senescence in human fibroblasts. *Cell Cycle* 2012; 11:730–9.
224. Sahin Umut U, Ferhi O, Jeanne M, Benhenda S, Berthier C, Jollivet F, Niwa-Kawakita M, Faklaris O, Setterblad N, de Thé H, et al. Oxidative stress-induced assembly of PML nuclear bodies controls sumoylation of partner proteins. *J Cell Biol* 2014; 204:931–45.
225. Guo S, Cheng X, Lim J-H, Liu Y, Kao H-Y. Control of antioxidative response by the tumor suppressor protein PML through regulating Nrf2 activity. *Mol Biol Cell* 2014; 25:2485–98.
226. Giovannini C, Matarrese P, Scazzocchio B, Sanchez M, Masella R, Malorni W. Mitochondria hyperpolarization is an early event in oxidized low-density lipoprotein-induced apoptosis in Caco-2 intestinal cells. *FEBS Lett* 2002; 523:200–6.
227. Nagy G, Koncz A, Perl A. T Cell Activation-Induced Mitochondrial Hyperpolarization Is Mediated by Ca²⁺- and Redox-Dependent Production of Nitric Oxide(). *J Immunol* 2003; 171:5188–97.
228. Liu J, Yin X, Liu B, Zheng H, Zhou G, Gong L, Li M, Li X, Wang Y, Hu J, et al. HP1 α mediates defective heterochromatin repair and accelerates senescence in Zmpste24-deficient cells. *Cell Cycle* 2014; 13:1237–47.
229. Liu Y, Drozdov I, Shroff R, Beltran LE, Shanahan CM. Prelamin A accelerates vascular calcification via activation of the DNA damage response and senescence-associated secretory phenotype in vascular smooth muscle cells. *Circ Res* 2013; 112:e99-109.
230. Lu D, Lian H, Zhang X, Shao H, Huang L, Qin C, Zhang L. LMNA E82K Mutation Activates FAS and Mitochondrial Pathways of Apoptosis in Heart Tissue Specific Transgenic Mice. *PLoS One* 2010; 5:e15167.
231. Childs BG, Baker DJ, Kirkland JL, Campisi J, van Deursen JM. Senescence and apoptosis: dueling or complementary cell fates? *EMBO Rep* 2014; 15:1139–53.
232. Chen QM, Liu J, Merrett JB. Apoptosis or senescence-like growth arrest: influence of cell-cycle position, p53, p21 and bax in H₂O₂ response of normal human fibroblasts. *Biochem J* 2000; 347:543–51.
233. Bladier C, Wolvetang EJ. Response of a Primary Human Fibroblast Cell Line to H₂O₂ : Growth Arrest or Apoptosis ? *Cell Growth Differ* 1997; 8:589–98.
234. Macip S, Igarashi M, Berggren P, Yu J, Lee SW, Aaronson S a. Influence of Induced Reactive Oxygen Species in p53-Mediated Cell Fate Decisions Influence of Induced Reactive Oxygen Species in p53-Mediated Cell Fate Decisions. *Society* 2003; 23:8576–85.
235. Livak KJ, Schmittgen TD. Analysis of relative gene expression data using real-time quantitative PCR and the 2-ddCT method. *Methods* 2001; 25:402–8.
236. Dixit R, Cyr R. Cell damage and reactive oxygen species production induced by fluorescence microscopy: effect on mitosis and guidelines for non-invasive fluorescence microscopy. *Plant J* 2003; 36:280–90.

237. Mukhopadhyay P, Rajesh M, Haskó G, Hawkins BJ, Madesh M, Pacher P. Simultaneous detection of apoptosis and mitochondrial superoxide production in live cells by flow cytometry and confocal microscopy. *Nat Protoc* 2007; 2:2295–301.
238. Konietzschke F, Hothorn LA, Brunner E. Rank-based multiple test procedures and simultaneous confidence intervals. *Electron J Stat* 2012; 6:738–59.
239. Wickham H. *ggplot2: Elegant Graphics for Data Analysis*. 1st ed. New York, NY: Springer New York; 2009.
240. Nitta RT, Jameson S a, Kudlow B a, Conlan L a, Kennedy BK. Stabilization of the retinoblastoma protein by A-type nuclear lamins is required for INK4A-mediated cell cycle arrest. *Mol Cell Biol* 2006; 26:5360–72.
241. McCord RP, Nazario-Toole A, Zhang H, Chines PS, Zhan Y, Erdos MR, Collins FS, Dekker J, Cao K. Correlated alterations in genome organization, histone methylation, and DNA-lamin A/C interactions in Hutchinson-Gilford progeria syndrome. *Genome Res* 2013; 23:260–9.
242. Maraldi NM, Capanni C, Lattanzi G, Camozzi D, Facchini A, Manzoli FA. SREBP1 interaction with prelamin A forms: a pathogenic mechanism for lipodystrophic laminopathies. *Adv Enzyme Regul* 2008; 48:209–23.
243. Wang J, Robinson JF, O’Neil CH, Edwards JY, Williams CM, Huff MW, Pickering JG, Hegele RA. Ankyrin G overexpression in Hutchinson-Gilford progeria syndrome fibroblasts identified through biological filtering of expression profiles. *J Hum Genet* 2006; 51:934–42.
244. Mateos J, Landeira-Abia A, Fafián-Labora JA, Fernández-Pernas P, Lesende-Rodríguez I, Fernández-Puente P, Fernández-Moreno M, Delmiro A, Martín MA, Blanco FJ, et al. iTRAQ-based analysis of progerin expression reveals mitochondrial dysfunction, reactive oxygen species accumulation and altered proteostasis. *Stem Cell Res Ther* 2015; 6:119.
245. Magagnotti C, Bachi A, Zerbini G, Fattore E, Fermo I, Riba M, Previtali SC, Ferrari M, Andolfo A, Benedetti S. Protein profiling reveals energy metabolism and cytoskeletal protein alterations in LMNA mutation carriers. *Biochim Biophys Acta* 2012; 1822:970–9.
246. Sieprath T, Corne TD, Nooteboom M, Grootaert C, Rajkovic A, Buyschaert B, Robijns J, Broers JL, Ramaekers FC, Koopman WJ, et al. Sustained accumulation of prelamin a and depletion of lamin A/C both cause oxidative stress and mitochondrial dysfunction but induce different cell fates. *Nucleus* 2015; :1–11.
247. Argenzio E, Margadant C, Leyton-Puig D, Janssen H, Jalink K, Sonnenberg A, Moolenaar WH. CLIC4 regulates cell adhesion and beta1 integrin trafficking. *J Cell Sci* 2014; 127:5189–203.
248. Berryman MA, Goldenring JR. CLIC4 Is Enriched at Cell-Cell Junctions and Colocalizes With AKAP350 at the Centrosome and Midbody of Cultured Mammalian Cells. *Cell Motil Cytoskeleton* 2003; 56:159–72.
249. Dang I, Gorelik R, Sousa-Blin C, Derivery E, Guérin C, Linkner J, Nemethova M,

- Dumortier JG, Giger FA, Chipysheva TA, et al. Inhibitory signalling to the Arp2/3 complex steers cell migration. *Nature* 2013;
250. Hwang JH, Smith C a, Salhia B, Rutka JT. The role of fascin in the migration and invasiveness of malignant glioma cells. *Neoplasia* 2008; 10:149–59.
 251. Kim DH, Wirtz D. Focal adhesion size uniquely predicts cell migration. *FASEB J* 2013; 27:1351–61.
 252. Snyder M, Huang XY, Zhang JJ. Signal Transducers and Activators of Transcription 3 (STAT3) directly regulates cytokine-induced fascin expression and is required for breast cancer cell migration. *J Biol Chem* 2011; 286:38886–93.
 253. Snyder M, Huang J, Huang X, Zhang JJ. A STAT3/NFκB Complex is Necessary for the Expression of Fascin in Metastatic Breast Cancer Cells in Response to IL-6 and TNF-α. 2014;
 254. Debidda M, Wang L, Zang H, Poli V, Zheng Y. A role of STAT3 in Rho GTPase-regulated cell migration and proliferation. *J Biol Chem* 2005; 280:17275–85.
 255. Lin Z-Q, Kondo T, Ishida Y, Takayasu T, Mukaida N. Essential involvement of IL-6 in the skin wound-healing process as evidenced by delayed wound healing in IL-6-deficient mice. *J Leukoc Biol* 2003; 73:713–21.
 256. Schrott G, Philippar U, Berger J, Schwarz H, Heidenreich O, Nordheim A. Serum response factor is crucial for actin cytoskeletal organization and focal adhesion assembly in embryonic stem cells. *J Cell Biol* 2002; 156:737–50.
 257. Selvaraj A, Prywes R. Expression profiling of serum inducible genes identifies a subset of SRF target genes that are MKL dependent. *BMC Mol Biol* 2004; 5:13.
 258. Schwartz B, Marks M, Wittler L, Werber M, Währisch S, Nordheim A, Herrmann BG, Grote P. SRF is essential for mesodermal cell migration during elongation of the embryonic body axis. *Mech Dev* 2014; 133:23–35.
 259. Mullins RD, Heuser JA, Pollard TD. The interaction of Arp2/3 complex with actin: nucleation, high affinity pointed end capping, and formation of branching networks of filaments. *Proc Natl Acad Sci U S A* 1998; 95:6181–6.
 260. Chorev DS, Moscovitz O, Geiger B, Sharon M. Regulation of focal adhesion formation by a vinculin-Arp2/3 hybrid complex. *Nat Commun* 2014; 5:3758.
 261. Elkhatib N, Neu MB, Zensen C, Schmoller KM, Louvard D, Bausch AR, Betz T, Vignjevic DM. Fascin plays a role in stress fiber organization and focal adhesion disassembly. *Curr Biol* 2014; 24:1492–9.
 262. Bertrand AT, Ziaei S, Ehret C, Duchemin H, Mamchaoui K, Bigot A, Mayer M, Quijano-Roy S, Desguerre I, Lainé J, et al. Cellular microenvironments reveal defective mechanosensing responses and elevated YAP signaling in LMNA-mutated muscle precursors. *J Cell Sci* 2014; 127:2873–84.
 263. Hale CM, Shrestha AL, Khatau SB, Stewart-Hutchinson PJ, Hernandez L, Stewart CL, Hodzic D, Wirtz D. Dysfunctional connections between the nucleus and the actin and microtubule networks in laminopathic models. *Biophys J* 2008; 95:5462–75.

264. Lim STS. Nuclear FAK: A new mode of gene regulation from cellular adhesions. *Mol Cells* 2013; 36:1–6.
265. Soiné JRD, Brand CA, Stricker J, Oakes PW, Gardel ML, Schwarz US. Model-based Traction Force Microscopy Reveals Differential Tension in Cellular Actin Bundles. *PLoS Comput Biol* 2015; 11:1–16.
266. Beningo KA, Dembo M, Kaverina I, Small JV, Wang YL. Nascent focal adhesions are responsible for the generation of strong propulsive forces in migrating fibroblasts. *J Cell Biol* 2001; 153:881–7.
267. Stricker J, Aratyn-Schaus Y, Oakes PW, Gardel ML. Spatiotemporal constraints on the force-dependent growth of focal adhesions. *Biophys J* 2011; 100:2883–93.
268. Chancellor TJ, Lee J, Thodeti CK, Lele T. Actomyosin tension exerted on the nucleus through nesprin-1 connections influences endothelial cell adhesion, migration, and cyclic strain-induced reorientation. *Biophys J* 2010; 99:115–23.
269. Kuo J, Lin J, Staddon JM, Hosoya H, Chen R. Uncoordinated regulation of stress fibers and focal adhesions by DAP kinase. *J Cell Sci* 2003; 116:4777–90.
270. Houle F, Poirier A, Dumaresq J, Huot J. DAP kinase mediates the phosphorylation of tropomyosin-1 downstream of the ERK pathway, which regulates the formation of stress fibers in response to oxidative stress. *J Cell Sci* 2007; 120:3666–77.
271. Lee JSH, Hale CM, Panorchan P, Khatau SB, George JP, Tseng Y, Stewart CL, Hodzic D, Wirtz D. Nuclear lamin A/C deficiency induces defects in cell mechanics, polarization, and migration. *Biophys J* 2007; 93:2542–52.
272. Foster CR, Robson JL, Simon WJ, Twigg J, Cruikshank D, Wilson RG, Hutchison CJ. The role of Lamin A in cytoskeleton organization in colorectal cancer cells: a proteomic investigation. *Nucleus* 2011; 2:434–43.
273. Schaller MD. FAK and paxillin: Regulators of N-cadherin adhesion and inhibitors of cell migration? *J Cell Biol* 2004; 166:157–9.
274. Salgia R, Li J, Ewaniuk DS, Wang Y, Sattler M, Chen W, Richards W, Pisick E, Shapiro GI, Rollins BJ, et al. Expression of the focal adhesion protein paxillin in lung cancer and its relation to cell motility. 1999;
275. Mierke CT. The Role of Vinculin in the Regulation of the Mechanical Properties of Cells. *Cell Biochem Biophys* 2009; 53:115–26.
276. Houben F, Willems CHMP, Declercq ILJ, Hochstenbach K, Kamps MA, Snoeckx LHEH, Ramaekers FCS, Broers JL V. Disturbed nuclear orientation and cellular migration in A-type lamin deficient cells. *Biochim Biophys Acta - Mol Cell Res* 2009; 1793:312–24.
277. Veith C, Marsh LM, Wygrecka M, Rutschmann K, Seeger W, Weissmann N, Kwapiszewska G. Paxillin Regulates Pulmonary Arterial Smooth Muscle Cell Function in Pulmonary Hypertension. *Am J Pathol* 2012; 181:1621–33.
278. Wade R, Bohl J, Vande Pol S. Paxillin null embryonic stem cells are impaired in cell spreading and tyrosine phosphorylation of focal adhesion kinase. *Oncogene*

2002; 21:96–107.

279. Khatau SB, Bloom RJ, Bajpai S, Razafsky D, Zang S, Giri A, Wu P-H, Marchand J, Celedon A, Hale CM, et al. The distinct roles of the nucleus and nucleus-cytoskeleton connections in three-dimensional cell migration. *Sci Rep* 2012; 2:488.
280. Krause M, Wolf K. Cancer cell migration in 3d tissue: Negotiating space by proteolysis and nuclear deformability. *Cell Adhes Migr* 2015; 9:357–66.
281. Cox J, Mann M. MaxQuant enables high peptide identification rates, individualized p.p.b.-range mass accuracies and proteome-wide protein quantification. *Nat Biotechnol* 2008; 26:1367–72.
282. Perkins DN, Pappin DJC, Creasy DM, Cottrell JS. Probability-based protein identification by searching sequence databases using mass spectrometry data. *Electrophoresis* 1999; 20:3351–567.
283. Mi H, Poudel S, Muruganujan A, Casagrande JT, Thomas PD. PANTHER version 10: expanded protein families and functions, and analysis tools. *Nucleic Acids Res* 2016; 44:D336-42.
284. Eden E, Navon R, Steinfeld I, Lipson D, Yakhini Z. GOrilla: a tool for discovery and visualization of enriched GO terms in ranked gene lists. *BMC Bioinformatics* 2009; 10:48.
285. Jonkman JEN, Cathcart J a., Xu F, Bartolini ME, Amon JE, Stevens KM, Colarusso P. An introduction to the wound healing assay using live-cell microscopy. *Cell Adh Migr* 2015; 8:440–51.
286. Grevesse T, Versaevel M, Circelli G, Desprez S, Gabriele S. A simple route to functionalize polyacrylamide hydrogels for the independent tuning of mechanotransduction cues. *Lab Chip* 2013; 13:777–80.
287. Versaevel M, Grevesse T, Gabriele S. Spatial coordination between cell and nuclear shape within micropatterned endothelial cells. *Nat Commun* 2012; 3:671.
288. Walle E Van De, Nieuwenhove I Van, Vanderleyden E, Declercq H, Gellynck K, Schaubroeck D, Ottevaere H, Thienpont H, Vos WH De, Cornelissen M, et al. Polydopamine–Gelatin as Universal Cell-Interactive Coating for Methacrylate-Based Medical Device Packaging Materials: When Surface Chemistry Overrides Substrate Bulk Properties. *Biomacromolecules* 2016; 17:56–68.
289. Hollander M, Wolfe DA. Nonparametric statistical methods [Internet]. Wiley; 1973.
290. Schie IW, Huser T. Methods and Applications of Raman Microspectroscopy to Single-Cell Analysis. *focal point Rev* 2013; 67:993–6.
291. Krafft C, Knetschke T, Siegner A, Funk RHW, Salzer R. Mapping of single cells by near infrared Raman microspectroscopy. *Vib Spectrosc* 2003; 32:75–83.
292. Beleites C, Sergo V. hyperSpec: a package to handle hyperspectral data sets in R [Internet]. 2014;
293. Lim NSJ, Hamed Z, Yeow CH, Chan C, Huang Z. Early detection of biomolecular changes in disrupted porcine cartilage using polarized Raman spectroscopy. *J*

Biomed Opt 2011; 16:17003.

294. Gelder J De, Gussem K De, Vandenabeele P, Moens L. Reference database of Raman spectra of biological molecules. 2007; :1133–47.
295. Apice MRD, Licata N, Novelli G. Skeletal phenotype of mandibuloacral dysplasia associated with mutations in. *Bone* 2010; 47:591–7.
296. Ran FA, Hsu PPD, Wright J, Agarwala V, Scott D a, Zhang F. Genome engineering using the CRISPR-Cas9 system. *Nat Protoc* 2013; 8:2281–308.
297. Yang L, Esvelt KM, Aach J, Guell M, Dicarlo JE, Norville JE, Church GM. RNA-Guided Human Genome. 2013; :823–7.
298. Zhang X-H, Tee LY, Wang X-G, Huang Q-S, Yang S-H. Off-target Effects in CRISPR/Cas9-mediated Genome Engineering. *Mol Ther Nucleic Acids* 2015; 4:e264.
299. Landry JJM, Pyl PT, Rausch T, Zichner T, Tekkedil MM, Stütz AM, Jauch A, Aiyar RS, Pau G, Delhomme N, et al. The genomic and transcriptomic landscape of a HeLa cell line. *G3 (Bethesda)* 2013; 3:1213–24.
300. Tauchi-Sato K, Ozeki S, Houjou T, Taguchi R, Fujimoto T. The surface of lipid droplets is a phospholipid monolayer with a unique fatty acid composition. *J Biol Chem* 2002; 277:44507–12.
301. Fujimoto T, Parton RG. Not just fat: The structure and function of the lipid droplet. *Cold Spring Harb Perspect Biol* 2011; 3:1–17.
302. Cheng J, Fujita A, Ohsaki Y, Suzuki M, Shinohara Y, Fujimoto T. Quantitative electron microscopy shows uniform incorporation of triglycerides into existing lipid droplets. *Histochem Cell Biol* 2009; 132:281–91.
303. Listenberger LL, Han X, Lewis SE, Cases S, Farese R V, Ory DS, Schaffer JE. Triglyceride accumulation protects against fatty acid-induced lipotoxicity. *Proc Natl Acad Sci U S A* 2003; 100:3077–82.
304. Kraemer N, Farese R V, Walther TC. Balancing the fat: lipid droplets and human disease. *EMBO Mol Med* 2013; 5:905–15.
305. Thiam AR, Farese R V, Walther TC. The biophysics and cell biology of lipid droplets. *Nat Rev Mol Cell Biol* 2013; 14:775–86.
306. Igal RA, Wang S, Gonzalez-Baró M, Coleman RA. Mitochondrial Glycerol Phosphate Acyltransferase Directs the Incorporation of Exogenous Fatty Acids into Triacylglycerol. *J Biol Chem* 2001; 276:42205–12.
307. Lindén D, William-Olsson L, Rhedin M, Asztély A-K, Clapham JC, Schreyer S. Overexpression of mitochondrial GPAT in rat hepatocytes leads to decreased fatty acid oxidation and increased glycerolipid biosynthesis. *J Lipid Res* 2004; 45:1279–88.
308. Wilfling F, Wang H, Haas JT, Kraemer N, Gould TJ, Cheng J, Graham M, Christiano R, Fröhlich F, Buhman KK, et al. Growth by Relocalizing from the ER to Lipid Droplets. 2013; 24:384–99.
309. Cohen B-C, Shamay A, Argov-Argaman N. Regulation of lipid droplet size in

- mammary epithelial cells by remodeling of membrane lipid composition—a potential mechanism. *PLoS One* 2015; 10:e0121645.
310. Handschin C, Spiegelman BM. Peroxisome proliferator-activated receptor γ coactivator 1 coactivators, energy homeostasis, and metabolism. *Endocr Rev* 2006; 27:728–35.
 311. Mormeneo E, Jimenez-Mallebrera C, Palomer X, de Nigris V, Vázquez-Carrera M, Orozco A, Nascimento A, Colomer J, Lerín C, Gómez-Foix AM. PGC-1 α induces mitochondrial and myokine transcriptional programs and lipid droplet and glycogen accumulation in cultured human skeletal muscle cells. *PLoS One* 2012; 7.
 312. Sánchez P, Infante A, Ruiz de Eguino G, Fuentes-Maestre J a., Manuel García-Verdugo J, Rodríguez CI. Age-related lipid metabolic signature in human *LMNA*-lipodystrophic stem cell derived adipocytes. *J Clin Endocrinol Metab* 2015; :jc.2014-4528.
 313. Mariño G, Ugalde AP, Salvador-Montoliu N, Varela I, Quirós PM, Cadiñanos J, van der Pluijm I, Freije JMP, López-Otín C. Premature aging in mice activates a systemic metabolic response involving autophagy induction. *Hum Mol Genet* 2008; 17:2196–211.
 314. Lopez-mejia IC, Toledo M De, Chavey C, Lapasset L, Cavelier P, Lopez-herrera C, Chebli K, Fort P, Beranger G, Fajas L, et al. Antagonistic functions of *LMNA* isoforms in energy expenditure and lifespan. 2014; :1–11.
 315. Shackleton S, Smallwood DT, Clayton P, Wilson LC, Agarwal a K, Garg a, Trembath RC. Compound heterozygous *ZMPSTE24* mutations reduce prelamin A processing and result in a severe progeroid phenotype. *J Med Genet* 2005; 42:e36.
 316. Agarwal a. K, Fryns J-P, Auchus RJ, Garg A. Zinc metalloproteinase, *ZMPSTE24*, is mutated in mandibuloacral dysplasia. *Hum Mol Genet* 2003; 12:1995–2001.
 317. Ruiz de Eguino G, Infante A, Schlangen K, Aransay AM, Fullaondo A, Soriano M, Garcia-Verdugo JM, Martin AG, Rodriguez CI. Sp1 transcription factor interaction with accumulated prelamin a impairs adipose lineage differentiation in human mesenchymal stem cells: essential role of sp1 in the integrity of lipid vesicles. *Stem Cells Transl Med* 2012; 1:309–21.
 318. Hernandez-Vallejo SJ, Beaupere C, Larghero J, Capeau J, Lagathu C. HIV protease inhibitors induce senescence and alter osteoblastic potential of human bone marrow mesenchymal stem cells: beneficial effect of pravastatin. *Aging Cell* 2013; :1–11.
 319. Caron M, Auclair M, Sterlingot H, Kornprobst M, Capeau J. Some HIV protease inhibitors alter lamin A/C maturation and stability, SREBP-1 nuclear localization and adipocyte differentiation. *AIDS* 2003; 17:2437–44.
 320. Meng Z, Petrov GI, Yakovlev V V. Pure electrical, highly-efficient and sidelobe free coherent Raman spectroscopy using acousto-optics tunable filter (AOTF). *Sci Rep* 2016; 6:20017.

321. Inui M, Miyado M, Igarashi M, Tamano M, Kubo A, Yamashita S, Asahara H, Fukami M, Takada S. Rapid generation of mouse models with defined point mutations by the CRISPR /. 2014; :1–8.
322. Petrini S, Borghi R, Oria VD, Restaldi F, Moreno S, Novelli A, Bertini E, Compagnucci C. Aged induced pluripotent stem cell (iPSCs) as a new cellular model for studying premature aging. 2017; 9:1453–66.
323. Chen Z, Chang WY, Etheridge A, Strickfaden H, Jin Z, Palidwor G, Cho J, Wang K, Kwon SY, Dor C, et al. Reprogramming progeria fibroblasts re-establishes a normal epigenetic landscape. 2017; :1–18.
324. Sui H, Zhou M, Chen Q, Lane HC, Imamichi T. siRNA enhances DNA-mediated interferon lambda-1 response through crosstalk between RIG-I and IFI16 signalling pathway. *Nucleic Acids Res* 2014; 42:583–98.
325. Olejniczak M, Galka P, Krzyzosiak WJ. Sequence-non-specific effects of RNA interference triggers and microRNA regulators. *Nucleic Acids Res* 2010; 38:1–16.
326. Jackson AL, Linsley PS. Recognizing and avoiding siRNA off-target effects for target identification and therapeutic application. *Nat Rev Drug Discov* 2010; 9:57–67.
327. Cao J, Wu L, Zhang S, Lu M, Cheung WKC, Cai W, Gale M, Xu Q, Yan Q. An easy and efficient inducible CRISPR / Cas9 platform with improved specificity for multiple gene targeting. 2016; 44:1–10.
328. Verstraeten VLRM, Caputo S, Steensel MAM Van, Duband-goulet I, Zinn-justin S, Kamps M, Kuijpers HJH, Ostlund C, Worman HJ, Briedé JJ, et al. The R439C mutation in LMNA causes lamin oligomerization and susceptibility to oxidative stress. 2009; 13:959–71.
329. Christie D a, Lemke CD, Elias IM, Chau L a, Kirchhof MG, Li B, Ball EH, Dunn SD, Hatch GM, Madrenas J. Stomatin-like protein 2 binds cardiolipin and regulates mitochondrial biogenesis and function. *Mol Cell Biol* 2011; 31:3845–56.
330. Choi JC, Muchir A, Wu W, Iwata S, Homma S, Morrow JP, Worman HJ. Temsirolimus Activates Autophagy and Ameliorates Cardiomyopathy Caused by Lamin A/C Gene Mutation. *Sci Transl Med* 2012; 4:144ra102-144ra102.
331. Marushige Y, Marushige K. Alterations in focal adhesion and cytoskeletal proteins during apoptosis. *Anticancer Res* 1998; 18:301—307.
332. Shim SR, Kook S, Kim JI, Song WK. Degradation of focal adhesion proteins paxillin and p130cas by caspases or calpains in apoptotic rat-1 and L929 cells. *Biochem Biophys Res Commun* 2001; 286:601–8.
333. Zhu X, Ohtsubo M, Bhmer RM, Roberts JM, Assoian RK. Adhesion-dependent Cell Cycle Progression Linked to the Expression of Cyclin D1, Activation of Cyclin E-cdk2, and Phosphorylation of the Retinoblastoma Protein. 1996; 133:391–403.
334. Kang HT, Park JT, Choi K, Choi HJC, Jung CW, Kim GR, Lee YS, Park SC. Chemical screening identifies ROCK as a target for recovering mitochondrial

- function in Hutchinson-Gilford progeria syndrome. *Aging Cell* 2017; :541–50.
335. Xiong Z-M, Choi JY, Wang K, Zhang H, Tariq Z, Wu D, Ko E, LaDana C, Sesaki H, Cao K. Methylene blue alleviates nuclear and mitochondrial abnormalities in progeria. *Aging Cell* 2015; :n/a-n/a.
 336. Willer MK, Carroll CW. Substrate stiffness-dependent regulation of SRF/Mkl1 requires the inner nuclear membrane protein Emerin. *J Cell Sci* 2017;
 337. Vaughan O a, Alvarez-Reyes M, Bridger JM, Broers JL, Ramaekers FC, Wehnert M, Morris GE, WGF W, Hutchison CJ. Both emerin and lamin C depend on lamin A for localization at the nuclear envelope. [Internet]. *J. Cell Sci.*2001; 114:2577–90.
 338. Ramachandran C, Patil R V, Combrink K, Sharif NA, Srinivas SP. Rho-Rho kinase pathway in the actomyosin contraction and cell-matrix adhesion in immortalized human trabecular meshwork cells. *Mol Vis* 2011; 17:1877–90.
 339. Herms A, Bosch M, Reddy BJN, Schieber NL, Fajardo A, Rupérez C, Fernández-Vidal A, Ferguson C, Rentero C, Tebar F, et al. AMPK activation promotes lipid droplet dispersion on detyrosinated microtubules to increase mitochondrial fatty acid oxidation. *Nat Commun* 2015; 6:7176.
 340. Li J, Cheng J-X. Direct Visualization of De novo Lipogenesis in Single Living Cells. *Sci Rep* 2014; 4:6807.
 341. Frock RL, Chen SC, Da DF, Frett E, Lau C, Brown C, Pak DN, Wang Y, Muchir A, Worman HJ, et al. Cardiomyocyte-specific expression of lamin A improves cardiac function in *Lmna*^{-/-} mice. *PLoS One* 2012; 7.
 342. Pampaloni F, Reynaud EG, Stelzer EHK. The third dimension bridges the gap between cell culture and live tissue. *Nat Rev Mol Cell Biol* 2007; 8:839–45.
 343. Frade MAC, de Andrade TAM, Aguiar AFCL, Guedes FA, Leite MN, Passos WR, Coelho EB, Das PK. Prolonged viability of human organotypic skin explant in culture method (hOSEC). *An Bras Dermatol* 2015; 90:347–50.
 344. Fraley SI, Feng Y, Krishnamurthy R, Kim D, Celedon A, Longmore GD, Wirtz D, Louis S. A distinctive role for focal adhesion proteins in three-dimensional cell motility. *Nat Cell Biol* 2010; 12:598–604.

Ir. Ing. Tobias Corne

Wijnbergstraat 52
8560 Wevelgem, Belgium
Phone: +32484159829
Email: tobi.corne@gmail.com

Last updated April, 2017

WORKING EXPERIENCE

PROFESSIONAL EXPERIENCE

- 2016-Present Innovation engineer at **CREAX**, Kortrijk.
- 2012-Present **PhD Student in Applied Biological Sciences**, Cell and Gene Biotechnology at Cell Systems & Imaging, Department Molecular Biotechnology, **Ghent University** and the **University of Antwerp** (Joint PhD).

INTERNSHIP EXPERIENCE

- March 2014 Working visit to learn data analysis of confocal Raman datasets in the laboratory of Prof. Christophe Krafft at the **Institute of Photonic Technology** (IPHT), Jena, Germany.
- September 2013 Working visit to enhance expertise in confocal Raman microspectroscopy with Prof. Andre Skirtach at the **Max Planck institute of Colloids and Interfaces**, Potsdam, Germany.
- 2011-2012 Masterthesis "Structurele en functionele analyse van telomeer-lamine interacties." At Ghent University, faculty of Bioscience Engineering, Department of Molecular Biotechnology, Gent, Belgium.
- 2010 Performance of cytotoxicity assays in the context of the master thesis "Implementatie van *in vitro* methoden voor het bepalen van de carcinogene eigenschappen van vleeswaren." At University College West-Vlaanderen, Department Simon Stevin, Brugge, Belgium.
- 2009-2010 Performance of Ames tests in the context of the master thesis "Implementatie van *in vitro* methoden voor het bepalen van de carcinogene eigenschappen van vleeswaren." At University College West-Vlaanderen, Campus Graaf Karel de Goedelaan, Kortrijk, Belgium.
- 2009 Implementation of *in vitro* meat digestion in the context of the master thesis "Implementatie van *in vitro* methoden voor het bepalen van de carcinogene eigenschappen van vleeswaren." At

Ghent University, Department of Animal Production, Laboratory for Animal Nutrition and Animal Product Quality, Melle, Belgium.

TEACHING EXPERIENCE

- 2015-Present Tutor of Frederick Tison. Master thesis entitled “Moleculaire karakterisatie van *ZMPSTE24* deficiënte cellen met Raman microspectroscopie”.
- October 2015 Demo practicum Cell Biology Course 3rd Bachelor Bioscience engineering, “Introduction to confocal microscopy”.
- February 2015 BVL **Molecular Biology and Cytometry Course**, “Basic microscopy and image processing.” at University College of Karel De Grote, Campus of Industrial Science and Technology, Hoboken, Belgium.
- 2014-2015 Tutor of Niels De Brandt. Master thesis entitled “Moleculaire karakterisatie van laminopathie modelcellen”.
- May 2013 BVAC **Molecular Biology and Cytometry Course**, “Introduction to advanced proteomics.” At SCK-CEN, Mol, Belgium.
- October 2013 Demo practicum Cell Biology Course 3rd Bachelor Bioscience engineering, “Introduction to confocal microscopy”.

EDUCATION

- 2012-Present Ghent University and University of Antwerp (Joint PhD), **Doctor of Applied Biological Sciences**.
- 2010-2012 Ghent University, **Master of Science in Bioscience Engineering, Cell and Gene Biotechnology**. Thesis: “Structurele en functionele analyse van telomeer-lamine interacties.”

*Optional course “Biopharmacy of Biotechnological Drugs”, lectured by Prof. Dr. Stefaan De Smedt.
- 2006-2010 University College West-Vlaanderen, **Master of Science in Biochemical Engineering Technology**. Thesis: “Implementatie van in vitro methoden voor het bepalen van de carcinogene eigenschappen van vleeswaren.”

SPECIALIST COURSES

- November 2012 “Mass spectrometry data processing”, VIB Bioinformatics Training & Service Facility (BITS), Gent, Belgium.
- October 2012 “Introduction to Linux for bioinformatics”, VIB Bioinformatics Training & Service Facility (BITS), Gent, Belgium.

CONGRESS PARTICIPATION

1. **T. Corne**, T. Sieprath and W. De Vos (2013). MIMICKING LAMINOPATHIES WITH MODEL CELL LINES. In *The BSCDB Autumn Meeting, Abstracts*. Liège, Belgium. [Poster]
2. **T. Corne**, P. Wuytens, C. Beleites, A. Skirtach and W. De Vos (2014). IDENTIFICATION OF SUBCELLULAR STRUCTURES WITH RAMAN MICROSCOPY. In *Biolmage Informatics, Abstracts*. The Biolmage Informatics communication network. Leuven, Belgium. [Poster]
3. **T. Corne**, T. Sieprath, J. Vandenbussche, K. Gevaert and W. De Vos (2014). QUANTITATIVE PROTEOMICS REVEALS DIFFERENTIAL EFFECTS OF ZMPSTE24 AND LMNA KNOCKDOWN ON HUMAN FIBROBLASTS. In *Systems-Level View of Cytoskeletal Function, EMBO workshop, Abstracts*. Stockholm, Sweden. [Poster]
4. **T. Sieprath**, **T. Corne**, W.J. Koopman, P.H. Willems and W. De Vos (2014). CHEMICALLY AND GENETICALLY INDUCED ACCUMULATION OF FARNESYLATED PRELAMIN A DIFFERENTIALLY AFFECT OXIDATIVE STRESS AND MITOCHONDRIAL POTENTIAL. In *Systems-Level View of Cytoskeletal Function, EMBO workshop, Abstracts*. Stockholm, Sweden. [Poster]
5. **T. Sieprath**, **T. Corne**, W.J. Koopman, P.H. Willems and W. De Vos (2014). HIGH-CONTENT ANALYSIS OF CELLULAR OXIDATIVE STRESS. In *Biolmage Informatics, Abstracts*. In *Biolmage Informatics, Abstracts*. The Biolmage Informatics communication network. Leuven, Belgium. [Poster]
6. **T. Corne**, T. Sieprath, J. Vandenbussche, K. Gevaert and W. De Vos (2015). QUANTITATIVE PROTEOMICS REVEALS ALTERED EXPRESSION OF ACTIN BINDING PROTEINS AFTER LMNA KNOCKDOWN IN HUMAN DERMAL FIBROBLASTS. In *Nuclear structure and dynamics, EMBO conference, Abstracts*. Isle sur Sorgue, France. [Poster]
7. **T. Corne**, T. Sieprath, J. Vandenbussche, K. Gevaert, M. Kea-te Lindert, K. Wolf and W. De Vos (2016). LAMIN A/C REGULATES SUBSTRATE ADHESION VIA THE ARP2/3 COMPLEX. In *European Cytoskeletal Forum - Cell Adhesion and Migration, Abstracts*. Cambridge, United Kingdom. [Flash poster presentation]

PEER-REVIEWED PUBLICATIONS

1. T. Sieprath*, **T. Corne***, M. Noteboom , C. Grootaert , A. Rajkovic , B. Buyschaert, J. Robijns, J. Broers, F. Ramaekers, W. Koopman, P. Willems and W. De Vos (2015). SUSTAINED ACCUMULATION OF PRELAMIN A AND DEPLETION OF LAMIN A/C BOTH CAUSE OXIDATIVE STRESS AND MITOCHONDRIAL DYSFUNCTION BUT INDUCE DIFFERENT CELL FATES. *Nucleus*, p1-11. DOI:10.1080/19491034.2015.1050568. (* **equal contribution**)
2. T. Sieprath, **T. Corne**, P. Willems, W. Koopman and W. De Vos (2016). INTEGRATED HIGH-CONTENT QUANTIFICATION OF INTRACELLULAR ROS LEVELS AND MITOCHONDRIAL MORPHOFUNCTION. *Advances in Anatomy, Embryology and Cell Biology*, 219, p149-177. DOI:10.1007/978-3-319-28549-8.
3. M. Versaevel, M. Riaz, **T. Corne**, T. Grevesse, J. Lantoine, D. Mohammed, C. Bruyère, L. Alaimo, W. De Vos and S. Gabriele (2016). PROBING CYTOSKELETAL PRE-STRESS AND NUCLEAR MECHANICS IN ENDOTHELIAL CELLS WITH SPATIOTEMPORALLY CONTROLLED ATTACHMENT AND DETACHMENT KINETICS ON MICROPATTERNED SUBSTRATES. *Cell Adhesion & Migration*, p98-109. DOI:10.1080/19336918.2016.1182290.
4. J. Robijns, F. Molenberghs, T. Sieprath, **T. D. J. Corne**, M. Verschuuren and W. H. De Vos (2016). IN SILICO SYNCHRONISATION REVEALS REGULATORS OF NUCLEAR RUPTURES IN LAMIN A/C DEFICIENT MODEL CELLS. *Scientific Reports*, 6:30325. DOI:10.1038/srep30325.
5. **T. D. J. Corne**, T. Sieprath, J. Vandenbussche, D. Mohammed, M. te Lindert, K. Gevaert, S. Gabriele, K. Wolf and W. H. De Vos (2016). DEREGULATION OF FOCAL ADHESION FORMATION AND CYTOSKELETAL TENSION DUE TO LOSS OF A-TYPE LAMINS. *Cell Adhesion & Migration*, p1-17. DOI:10.1080/19336918.2016.1247144.
6. T. Sieprath, **T. Corne**, J. Robijns, W. J. Koopman and W. H. De Vos (2017). CELLULAR REDOX PROFILING USING HIGH-CONTENT MICROSCOPY. *Journal of Visual Experiments*. DOI:10.3791/55449.
7. **T. D. J. Corne**, F. Tison, P. Wuytens, T. Sieprath, J. Robijns, C. Beleites, A. G. Skirtach and W. H. De Vos (2017). ZMPSTE24 DEFICIENCY IMPAIRS INTRACELLULAR LIPID STORAGE AS REVEALED BY RAMAN MICROSPECTROSCOPY. *PLoS ONE*. In preparation.

